Role of Sorting on the Composition of Siliciclastic Sediment: Implications for Interpreting Provenance after Limited Transport in an Arid Climate

A Thesis Presented for the
Master of Science
Degree
The University of Tennessee, Knoxville

Forrest Christopher Driscoll
August 2016

ACKNOWLEDGEMENTS

Completion of this work was made possible through the assistance of many people. Dr. Chris Fedo provided constant guidance, feedback, and fruitful discussion as an advisor. Committee members Dr. Bob Hatcher and Dr. Annette Engel helped to review my work and progress. Drs. Scott Samson and Mariana Bonich helped during a field season in the Mojave Desert by providing on-site discussion. Dr. Jeff Moersch operated the drone used to obtain high resolution aerial photographs of the field site. Graduate students at the University of Tennessee, friends, and family offered tremendous guidance and support during the completion of my degree. A grant awarded from the Geological Society of America was used to fund the petrography, geochemistry, and travel expenses for this study.

ABSTRACT

This study tested whether transport distances (< 500 m) have the capacity to shape the geochemistry of sediments across multiple grain-size populations due to sorting derived from a single source. In the Stepladder Mountains, Mojave Desert, CA, a < 1 km^2 [square kilometers] watershed allows for a controlled study to understand how modern sediments acquire their composition from a single granodioritic source in an arid climate where there is no chemical weathering. Sediments are naturally sorted into distinct grain-size populations, with modes ranging from very fine sand to gravel within a single, alluvial channel. Sediment samples representative of each population were petrographically and geochemically analyzed in order to test the effectiveness of commonly used discrimination diagrams. Sediments became proportionally enriched in plagioclase and biotite and depleted in K-feldspar and quartz with decreasing grain size. Major elements were plotted in Al_2O_3 [aluminum oxide]–CaO^*+Na_2O [sodium oxide]–K_2O [potassium oxide] and Al_2O_3–CaO^*+Na_2O+K_2O–FeO+MgO compositional space and indicate that a negligible degree of chemical weathering was involved in sediment production. Trace-element plots normalized to average granodiorite bedrock show strong enrichments in elements thought to be immobile during sedimentary processing (Cr, Co, and Sc) across nearly all sediment samples. Using any of these elements as ratios (Th/Co, La/Sc, Th/Sc, Cr/Th, Zr/Sc) in provenance discriminating plots reveal that sediment was formed source mixing, as sediments in these plots considerably deviate from bedrock composition due to the control grain size has on geochemistry. Sediment rare-earth element (REE) contents also deviate from source composition and show an increase in total REE content, decrease in fractionation of light REEs and heavy REEs, and an

increase in the magnitude of the negative Eu anomaly with decreasing grain size. Variations in sediment composition and thus geochemical ratios result from mineral sorting during transport, no matter how short. Thus, strong caution must be used when using discrimination diagrams to interpret sediment and sedimentary rock provenance.

TABLE OF CONTENTS

LIST OF TABLES

LIST OF FIGURES

1. INTRODUCTION

Unravelling the petrologic origin of sediment requires an approach that addresses the processes that control detrital composition from source to sink. Beyond original provenance compositions, sedimentary processes, such as chemical weathering, source mixing, mineral sorting during transport, and diagenesis, are all capable of affecting the composition of sediment after being released from source (Johnsson, 1993). Thus, the ability to reconstruct provenance (i.e., deciphering source rock characteristics from sediment) is limited to how well each step is understood.

For decades, numerous studies have used petrography and geochemistry as a way to reconstruct sediment provenance under the premise that source is the dominant control on sediment composition. Petrographic applications used the mineralogical modes to interpret tectonic settings of source terrains (Dickinson, 1970; Dickinson and Suczek, 1979; Dickinson and Valloni, 1980; Bhatia, 1983; Dickinson et al., 1983; Ingersoll et al., 1984) and to decipher paleoclimates (Basu, 1976; Suttner et al., 1981; Basu, 1985). With the advent of methods capable of extracting whole-rock geochemical information, major oxides have been used to observe the relationships between feldspar destruction and clay production (Nesbitt and Young, 1982) as a way to understand the role chemical weathering has on sediment composition (Nesbitt and Markovics, 1980; Roser and Korsch, 1988; Nesbitt and Young, 1996; Young and Nesbitt, 1998). As the understanding of the types of compositional changes that occur during soil formation improved, major-element compositions of sediments were used to interpret source rock compositions (Roser and Korsch, 1988; Fedo et al., 1995).

Groundbreaking geochemical work by Taylor and McLennan (1985) used trace-element patterns from sedimentary rocks to determine the average composition of the upper continental crust and its evolution, which subsequently broadened the application of using trace elements and rare-earth elements (REE) for provenance interpretation. Key findings presented in Taylor and McLennan (1985) suggested that certain trace elements with low solubility values (e.g. Zr, Hf, Sc, Cr, Th, Co and the REEs), and thus low residence times in water, are quantitatively transferred to the sedimentary record from source, regardless of denundational processes. Under this principle, many studies have expressed trace element compositions of sediment and sedimentary rocks as derived ratios (e.g. Th/Sc, La/Sc, Cr/Th, Th/Co) to interpret sources with similar geochemical characteristics (e.g. Bhatia and Crook, 1986; Wronkiewicz and Condie, 1987; McLennan, 1989; Feng and Kerrich, 1990; McLennan and Taylor, 1991; Condie et al., 1992; McLennan et al., 1993; Cullers, 1994; Fedo et al., 1996; Fralick and Kronberg, 1997; Holail and Moghazi, 1998; Armstrong-Altrin et al., 2004; Cullers, 2002; Oni et al., 2014; Eizenhöfer et al., 2015; Xiang et al., 2015).

Caution must be taken when using provenance discriminating techniques whose basis is the transfer of major or trace elements to the sedimentary record via chemical weathering, because such approaches disregard the notion that sediment may partly acquire its composition by mechanical processes during transport. In particular, mineral fractionation (i.e., sorting) causes concern in evaluating provenance (Cullers et al., 1987; Cullers, 1988; Nesbitt and Young, 1996; Fedo et al., 2015) because sorting is governed by how different minerals behave in water flow based upon their textural properties (e.g. density, shape, and crystal structure) that commonly result in the preferential

concentration of certain minerals into different grain-size fractions. This means that sorting introduces the possibility that some sediment fractions will become enriched in accessory minerals abundant in specific trace elements. Because trace elements and the minerals that they are incorporated in are linked to each other, elemental ratios commonly used to infer source composition may reveal geochemical values that are disproportionate to those of the actual provenance if minerals holding trace elements have become either concentrated or depleted in a fraction of sediment. As a result, it should be expected that some elemental ratios used for revealing source compositions may be impacted by sorting.

Despite the effects that sorting could impose on the composition of sediment, source-discriminating ratios are still extensively used to interpret provenance under the assumption that the chosen elements behave as a closed system during weathering and are quantitatively transferred to the sedimentary record. Recent studies (e.g. Singh, 2009; Schoenborn et al., 2012; Tang et al., 2012) use either trace-element signatures, elemental ratios, or REE patterns to infer the possible sources of sediment without accounting for the possible effects of sorting. In light of this situation, and following on the approach in Nesbitt and Young (1996) and Nesbitt et al. (1997), a controlled study is needed that aims to understand how siliciclastic sediment directly receives its composition from a single, simple geologic system with a known sediment source. Such a study can be conducted by going to a location that eliminates, minimizes, or controls the intensity of all other processes capable of modifying sediment composition.

Modi (2011) conducted such a study in the Stepladder Mountains in the Mojave Desert, CA (Fig. 1). The work was designed to test whether a mineralogical and

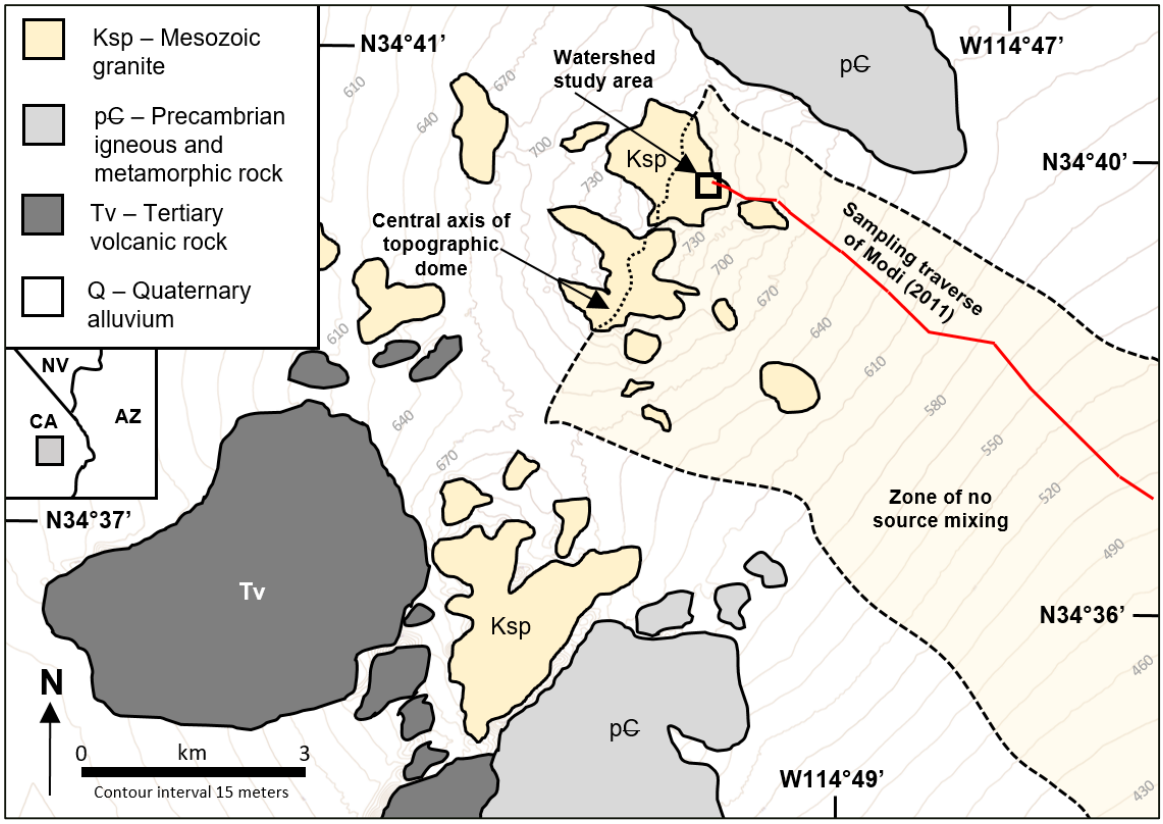

Figure 1. Map of the field area in the Mojave Desert, southeastern CA. The watershed site lies in the northern tip of the granitic Stepladder pluton (Ksp). Other exposed lithological units are marked. The red line marks the path in which sediment samples were collected across the pediment dome by Modi (2011).

geochemical provenance reconstruction of first-cycle sediment produced in an arid climate would correctly predict the source composition. That study area is located in a geological setting where sediment should ideally reflect source composition because: (1) the sediment in the vicinity is solely derived from the granodiorite Stepladder pluton (Modi, 2011), (2) the effects of chemical alteration on the bedrock or sediment are minimal because the region has been arid to semiarid since the early Holocene (McDonald et al., 2003), and (3) the sediment is currently in active transport and, therefore, has not yet been compositionally modified by diagenesis. Results from Modi (2011) recognized considerable deviations in the provenance-indicating, trace-element signatures from those of the bedrock. Modi (2011) interpreted the findings as a result of mineral sorting across 8 km of transport. However, collected sediments were scattered from the source to the lower plain of the piedmont (Fig. 1), prompting the concern that extrabasinal components were delivered by wind. Rare-earth element (REE) signatures in sediment derived from the pluton indicated that granitic bedrock from the Stepladder pluton is more compositionally similar to coarser-grained sediment than finer-grained sediment, although neither size group is the same as bedrock compositionally. Despite that all sediment in the region was most likely derived from the granitic Stepladder pluton, data scattered across a trace element plot commonly used for the assessment of source mixing permitted up to 10% of an endmember basalt in the fine sediment population (Modi, 2011).

Given the concern that wind-blown material might be a problem, and that the sampling traverse ranged from a mountainous source to an alluvial plain, the findings of Modi (2011) inspired an effort to further control the variables associated with source

mixing by refining the study area in Modi (2011) to a single, small watershed (Fig. 2A) contained entirely within the mountainous source area of the Stepladder pluton. This setting experiences high rates of downcutting (Dohrenwend, 1988) and therefore contains recently formed and transported sediment. Shallow, narrow fluvial channels within the watershed dissect the local bedrock and saprolite, and similar to the Modi (2011) study, contain sediments that have been naturally sorted into different grain-size populations that span from very fine sand to gravel (Fig. 3A-B). Given the results of Modi (2011), this observation prompts the question: even after very minimal transport, can sorting cause mineralogical components, and thus geochemical signatures in sediment, to deviate significantly from those of the source rock before sediment leaves the source area? If the preferentially sorted sediment is not geochemically equivalent to the source, then transport of almost any length holds the capacity to impose changes in sediment composition from source through the process of sorting. The purpose of this study is to apply field work coupled with the utilization of petrographic and geochemical techniques to examine whether the composition of sediments can be modified substantially enough during very short transport distances (0-500 m from source), where geochemical signatures fail to reconstruct provenance composition accurately.

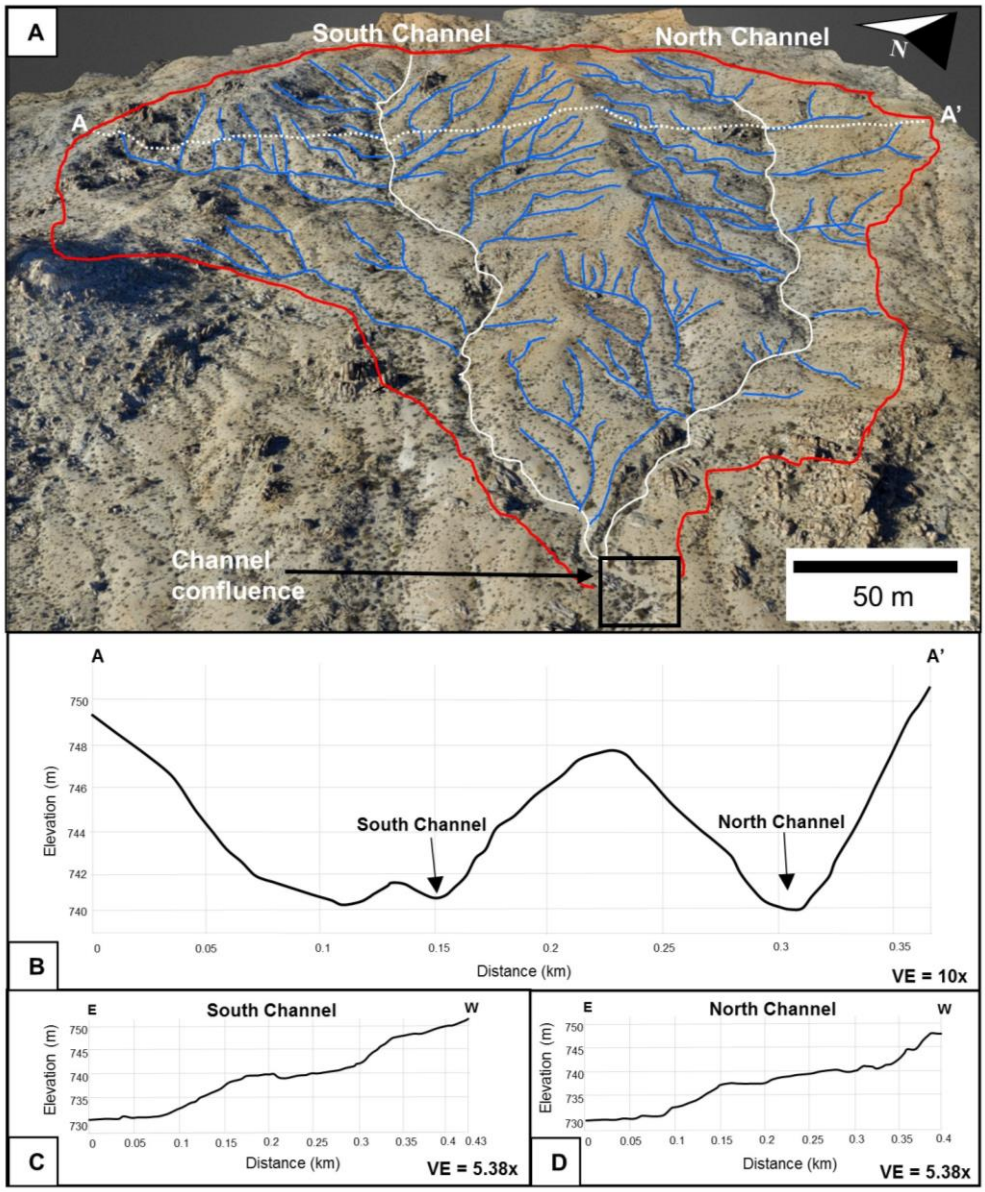

Figure 2A-D. Oblique low altitude aerial image looking west into studied watershed in the Stepladder Mountains, CA. (A) Boundary of watershed used in this study. Watershed margin is delineated in red. Two main channels are marked in white, with smaller feeding channels in blue. Black box indicates location of channel confluence where sediment samples were collected. (B) Topographic profile of the dotted white cross section line from A to A'. (C) Topographic profile of the south channel. (D) Topographic profile of north channel.

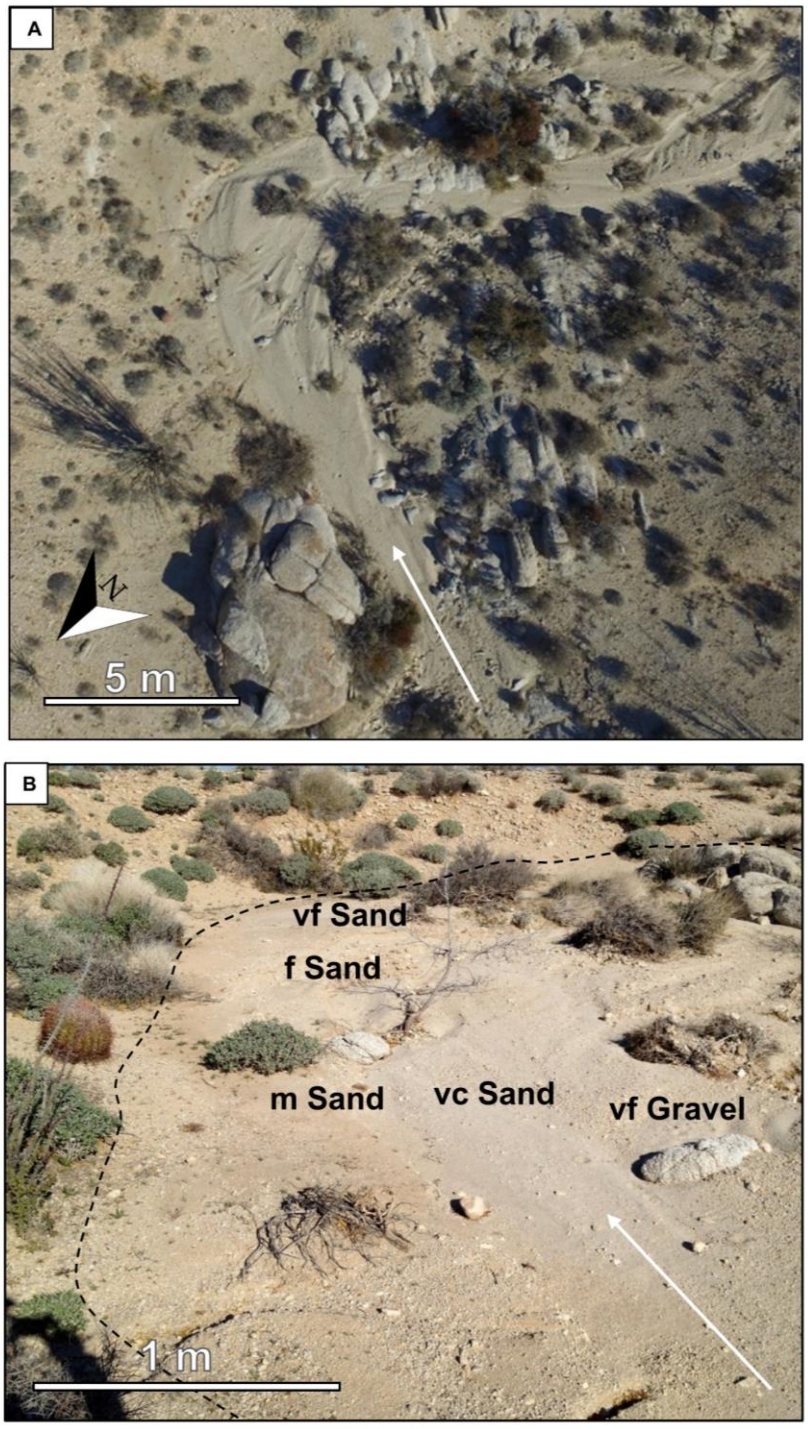

Figure 3A-B. Channel area holding sorted Stepladder sediments. (A) Direct overhead image of bending channel. White arrow denotes the direction of sediment transport. (B) Outline of the channel field site with general locations of grain-size populations. White arrow denotes the direction of sediment transport. Coordinates for channel area: 34°40’18.5’’N, 114°50’22.3’’W.

2. GEOLOGIC SETTING

The oldest basement rocks documented in the local area of the Stepladder Mountains consist of Paleoproterozoic gneisses and schists that underwent regional metamorphism at 1.7 Ga during the Ivanpah orogeny (Dewitt et al., 1984; Thomas et al., 1988; Wooden and Miller, 1990). These metamorphic rocks were later intruded by granitoids (1.76 to 1.64 Ga; Wooden and Miller, 1990), potassium-rich granites (1.4 Ga; Anderson and Bender, 1989), and diabase dikes (1.1 Ga; Miller and Wooden, 1994). By the Neoproterozoic, a stable craton developed upon which kilometers of sedimentary strata consisting of clastic and carbonate rocks were unconformably deposited (Fedo and Cooper, 2001). Tectonic activity during the Late Cretaceous was associated with the Laramide Orogeny and spurred regional magmatism and high-grade metamorphism (Anderson and Cullers, 1990), which resulted in the emplacement of widespread granitic plutons, including the Stepladder pluton, in the middle to upper crust (Miller and Wooden, 1994). Crustal thinning during the late Miocene within the Colorado River extensional corridor exposed rocks at the Earth's surface from depths down to 15 km (Howard and John, 1987), including the Stepladder pluton.

The Stepladder pluton is now exposed as a topographic dome (Fig. 1) with a low sloping pediment that extends away from the highlands where all channels drain away from the center of the range. Such landforms in the Mojave Desert, commonly referred to as pediment domes, are desirable locations to study rates of sediment erosion, transportation, and deposition. Cosmogenic nuclide models used to date the ages of exposed grains on Mojave pediment domes have shown that nuclide activities increase downslope (Nichols et al., 2002), which implies downwearing rates are the greatest in

mountainous areas with the steepest topography. Depositional rates of piedmont sediments in the Mojave Desert increase between 18 to 39 mm/ky throughout the Pleistocene (Nichols et al., 2005), until the early Holocene when the climate shifted to arid conditions. Due to the low annual rainfall in the Mojave Desert (12 cm/year; Stoffer, 2004), sediments are transported only decimeters per year across piedmonts (Nichols et al., 2002; Nichols et al., 2005). Greatest lengths of sediment transport occur within channel systems, where sediments can be transported several meters per year (Nichols et al., 2005) during strong rain events.

3. CHARACTERIZATION OF WATERSHED

The study area for this work is a small watershed (0.1 km^2; Fig. 2A) located on the east side of the central axis of a topographic dome at the northern tip of the Stepladder Mountains, southeastern CA (Fig. 1). Maximum topographic relief in the watershed is ~ 50 m, although this is based on the anomalously high peak at the southern boundary of the watershed (Fig. 2A). Excluding the peak, the common relief from the outer margin of the watershed to the lowest point at the southeastern margin is ~ 30 m.

Exposed bedrock in the watershed is fresh to slightly weathered, where the latter forms a saprolite at the surface. Fresh bedrock and saprolite are best exposed in the study area in the form of inselbergs and rocky outcrops. However, bedrock lies only centimeters beneath the erosional surface throughout the entire watershed (Fig. 2A).

Two large stream channels dissect the exposed bedrock and saprolite in the watershed and hold loose, unconsolidated sediment (Fig. 2A). Many lower-order streams bring sediment from higher elevations to the two main channels that are separated by a divide, that is topographically lower than the watershed boundary (Fig. 2B). The southern channel has a relief of 20 m (Fig. 2C), whereas the northern channel has a stream relief of 17 m (Fig. 2D). The southern and northern channels are approximately 430 and 400 m long in length before they reach a confluence at the southeastern margin of the watershed, where samples used in this study were collected. Stream gradients are 46.5 and 37.5 m/km for the southern and northern channels, respectively.

The channel section (~ 5 m wide) at this confluence (Fig. 3A) contains sediment sorted into multiple grain-size fractions (Fig. 3B) during fluvial transport. Sediments toward the outer section of the channel section are fine enough to produce mud cracks

during desiccation. Local small patches of accessory mineral deposits that contain distinctively darker grains are located in the main channels.

4. METHODS

4.1 Field Work

Five sediment samples (CD-1, CD-2, CD-3, CD-4, and CD-5; Fig. 4A-E) were collected in the channel (Fig. 3B) at the confluence of the north and south channels. Samples were collected with a shovel from areas where grain size was relatively consistent at the surface and at depth (~30 cm) and placed into locking plastic bags. Additional samples collected within the watershed include one magnetite concentrate (CD-M; Fig. 4F), one fresh bedrock sample (CD-BR), and one saprolite sample (CD-SAP). Structural measurements were made on joint surfaces of exposed bedrock across the field area.

4.2 Textural Analysis and Sample Preparation

To determine the grain-size distributions of the samples, each was individually sieved from -2 to 5 Φ in 0.5 Φ intervals (Table 1). Other statistical parameters of grain-size distributions, such as mean, median, mode, kurtosis, skewness, and modality following the approach in Folk and Ward (1957), were calculated (Table 1) by using the particle size analysis software GRADISTAT (Blott and Pye, 2001). Following sieving, each sample (CD-1, CD-2, CD-3, CD-4, and CD-5; Fig. 4A-E) was re-homogenized and coned-and-quartered into two separate aliquots, one for thin section petrography and the other for geochemical analysis.

In order to produce thin sections, sediment aliquots were stabilized in epoxy then cut into rectangular billets. The saprolite thin section was cut out from a hand sample of friable saprolite, bathed in epoxy, vacuum impregnated, dried, and cut into a rectangular

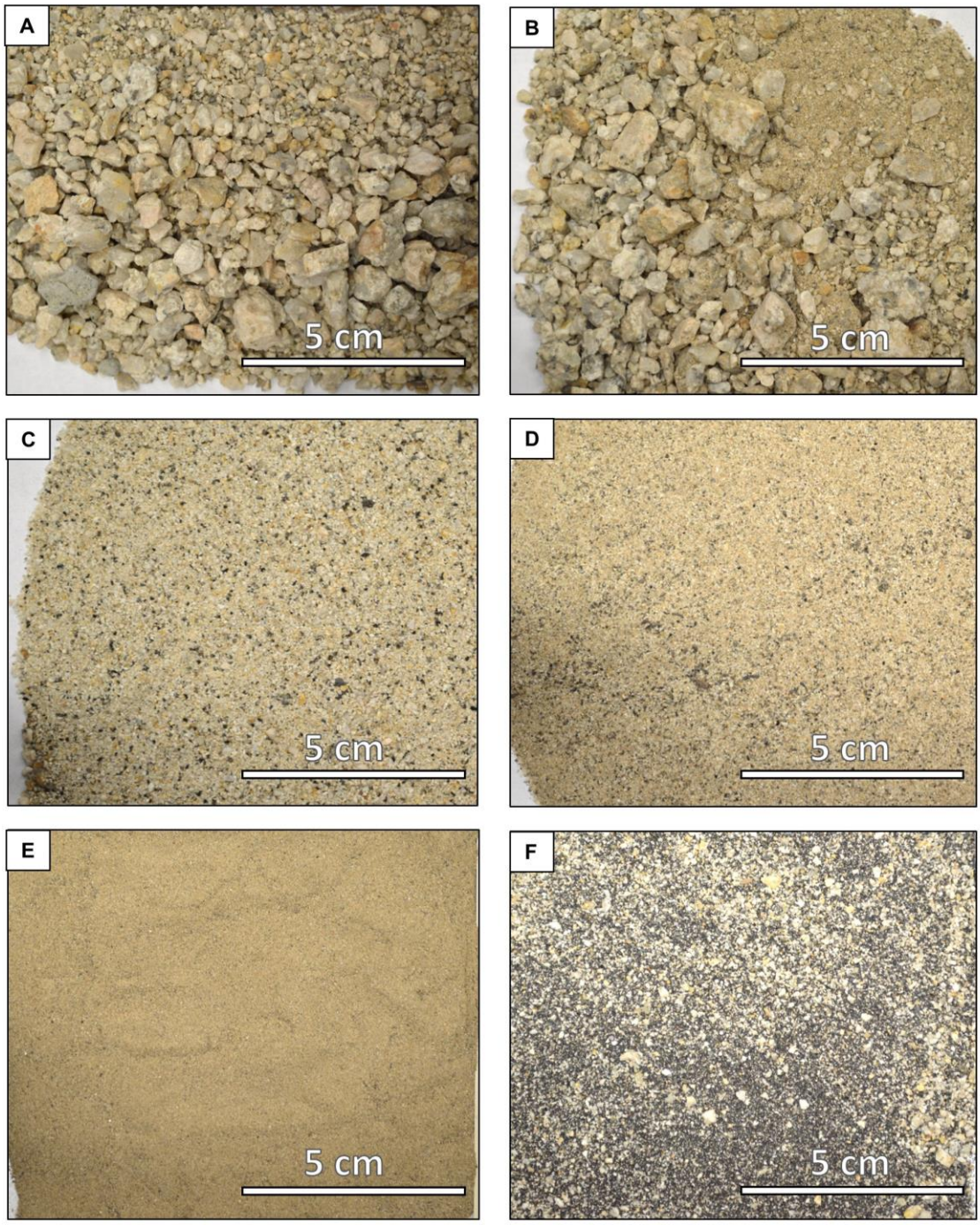

Figure 4A-F. Images of five samples collected from the channel section and the magnetite concentrate. (A) CD-1 – very fine gravel; (B) CD-2 – very coarse sand; (C) CD-3 – medium sand; (D) CD-4 – fine sand; (E) CD-5 – very fine sand. (F) Magnetite concentrate, CD-M, was collected as a heavy mineral deposit near the channel section.

Table 1. Textural descriptions for Stepladder sediments

	Stepladder Sediments					
	CD-1	CD-2	CD-3	CD-4	CD-5	CD-M
Textural Class[a]	Sandy gravel	Sandy gravel	Gravelly sand	Gravelly sand	Muddy sand	Gravelly sand
Modality	Bimodal	Unimodal	Unimodal	Unimodal	Unimodal	Unimodal
Rounding[b]	1 *Very angular*	1 *Very angular*	1 *Very angular*	2 *Angular*	2 *Angular*	1 *Very angular*
Avg. grain size[c] **($\bar{x}$)**	-1.245 Φ *vf Gravel*	-0.726 Φ *vc Sand*	1.008 Φ *m Sand*	2.415 Φ *f Sand*	3.621 Φ *vf Sand*	1.72 Φ *m Sand*
Sorting[d] **(σ)**	1.1 *Poor*	1.841 *Poor*	0.873 *Moderate*	0.980 *Moderate*	0.794 *Moderate*	0.895 *Moderate*
Skewness[e] **(*Sk*)**	0.365 *Very fine skewed*	0.632 *Very fine skewed*	-0.038 *Symmetrical*	0.100 *Symmetrical*	-0.010 *Symmetrical*	-0.370 *Very coarse skewed*
Kurtosis[f] **(*K*)**	1.035 *Mesokurtic*	0.871 *Platykurtic*	1.128 *Leptokurtic*	1.130 *Leptokurtic*	0.954 *Mesokurtic*	1.30 *Leptokurtic*
	Grain-size distributions in %					
-2 Φ	31	38	0	0	0	0
-1.5 Φ	16	12	1	0	0	1
-1 Φ	16	9	1	0	0	1
-0.5 Φ	13	7	3	0	0	2
0 Φ	8	5	7	1	0	3
0.5	6	5	14	1	0	4
1 Φ	3	4	23	3	0	7
1.5 Φ	2	4	25	9	1	11
2 Φ	1	4	16	19	2	25
2.5 Φ	1	3	6	23	5	31
3 Φ	1	2	2	19	13	13
3.5 Φ	1	2	1	11	23	2
4 Φ	0	2	1	7	25	0
4.5 Φ	0	1	0	4	16	0
5 Φ	1	2	0	3	15	0
Total	100	100	100	100	100	100
Sieving Error	0.1 %	0.2%	0.0%	0.2%	0.1%	0.2%

[a]Textural classifications and calculations after Folk (1974).
[d]Sorting calculated after Folk (1974).
[b]Roundness calculated using rho scale from Folk (1955) and diagrams from Powers (1953). Scale: 0 (very angular) to 6 (very rounded).
[c]Grain sizes represented in phi (Φ) units where $\Phi = -\log_2(d)$. d = grain size measured in mm. Abbreviations: vf = very fine; f = fine; m = medium; vc = very coarse.
[e]Skewness calculated from Folk (1974): $Sk = (\Phi 95 - \Phi 5)/2.44(\Phi 75 - \Phi 25)$.
[f]Kurtosis calculated from Folk (1974): $K = (\Phi 16+\Phi 84-2\Phi 50) / 2(\Phi 16+\Phi 84) + (\Phi 5+\Phi 95-2\Phi 50) / 2(\Phi 95+\Phi 5)$.

billet. Two bedrock thin sections were made by cutting sample CD-BR into two rectangular billets, referred to as CD-BR1 and CD-BR2. All billets were made into conventional 25 x 46 mm polished thin sections.

Aliquots of sediment samples reserved for geochemical analysis were pulverized in a ceramic shatterbox dish. Two aliquots of the coarsest sample (CD-1; Fig. 3A) were powdered separately and treated as individual samples during geochemical analysis to test for reproducibility in the dissolution process.

4.3 Petrography

Petrographic work was performed on thin sections using a Nikon LV100D POL microscope with a Conwy Valley Systems automated point counter attached to a computer. The program PETROG was used to create a grid of points for counting across the thin section space. Modal compositions of each sample were determined by point counting procedures using the Gazzi-Dickinson (Dickinson, 1970; Ingersoll et al., 1984) approach, where the mineralogical composition at 500 to 600 points across each thin section was identified (Table 2). For comparison with the Gazzi-Dickinson point counting technique, the Folk approach (Folk, 1974) was also employed that involves counting any polymineralic grains as lithic fragments regardless if the mineral under the cross hair is identifiable. General observations of clast roundness and shape were accomplished using a Nikon SMZ-800 incident light microscope (Table 1).

4.4 Geochemical analysis

Geochemical analyses were conducted by using powdered aliquots of the five collected sediment samples and the magnetite concentrate. Major (Table 3) and trace-element (Table 4) contents were determined by inductively coupled mass spectrometry

Table 2. Point-counted mineralogical modes of Stepladder sediments, saprolite, and bedrock.

		Sediment Samples					Bedrock			Saprolite
		CD-1	CD-2	CD-3	CD-4	CD-5	CD-BR1	CD-BR2	*Avg.*	CD-SAP
Point Counting Results	**Qm**	97	116	105	95	72	136	210	173	69
	Qp	10	5	1	3	0	13	2	7.5	41
	P	99	123	125	125	84	208	210	209	229
	K	108	126	81	79	52	108	41	74.5	122
	B	9	17	36	55	89	17	28	22.5	19
	Cc	2	1	12	5	5	0	0	0	0
	Op	1	7	9	13	20	6	6	6	6
	Ap	0	1	0	3	3	3	1	2	2
	Zr	0	0	0	1	2	0	0	0	0
	Total	326	396	369	379	327	491	498	495.5	490
	Misc	2	6	4	44	129	0	0	0	0
Normalized mineralogy (%)					**Folk QFL**					
	Q	1	14	21	29	34	-	-	-	-
	F	4	27	52	59	63	-	-	-	-
	L	95	59	27	12	3	-	-	-	-
					Gazzi-Dickinson QFL					
	Q	35	33	34	32	35	-	-	-	-
	F	65	67	66	68	65	-	-	-	-
	L	0	0	0	0	0	-	-	-	-
	Q	34	33	34	32	35	32	46	39	24
	P	32	33	40	42	40	45	45	45	50
	K	34	34	26	26	25	23	9	16	26
	Q	33	32	30	27	24	31	43	37	23
	F	64	64	60	57	46	66	51	59	73
	B	3	4	10	16	30	3	6	4	4

Qm: total monocrystalline quartz
Qp: total polycrystalline quartz
P: total plagioclase
K: total K-feldspar;
total feldspar (P+ K)
B: total biotite
Cc: total calcite from caliche
D: total opaque minerals
Ap: total apatite
Zr: total zircon
L: total lithic fragments
Total: total points counted as minerals
Misc: unidentifiable grains

Table 3. Major element oxides for Stepladder sediment, bedrock, and saprolite. Oxides reported in weight percent.

	SiO_2	TiO_2	Al_2O_3	Fe_2O_3	MnO	MgO	CaO	Na_2O	K_2O	P_2O_5	CO_2	LOI	Total	CIA
Sediment Samples														
CD-1 (1)	74.95	0.2	13.07	1.24	0.02	0.26	1.32	3.23	4.87	0.06	0.09	0.89	100.1	50.8
CD-1 (2)	75.6	0.18	12.47	1.25	0.02	0.26	1.44	2.99	4.04	0.05	0.11	0.89	99.19	51.9
Avg CD-1	75.27	0.19	12.77	1.24	0.02	0.26	1.38	3.11	4.45	0.06	0.1	0.89	99.64	51.4
CD-2	71.9	0.34	13.02	2.16	0.03	0.5	2.01	3.54	3.87	0.1	0.19	1.35	98.89	50.1
CD-3	66.7	0.54	16.66	2.45	0.04	0.69	2.68	4.9	3.38	0.15	0.28	2.02	100.2	51.6
CD-4	59.81	0.59	17.25	3.46	0.06	1.19	4.12	4.62	2.83	0.22	1.04	4.62	98.77	53.1
CD-5	58.79	0.63	16.45	4.06	0.08	1.79	4.39	3.23	2.67	0.18	1.36	7.67	99.93	56.6
Magnetite Concentrate														
CD-M	21.5	5.71	5.34	60.66	0.26	0.31	1.33	1.34	0.99	0.5	-	0.63	98.57	-
Bedrock*														
ST09-02	70.71	0.33	15.38	1.93	0.03	0.57	2.09	4.76	3.63	0.11	-	0.85	100.39	50.1
CF00-18	71.84	0.31	15.09	1.68	0.03	0.61	2.27	4.66	3.45	0.10	-	0.65	100.69	49.7
CF96-4	71.39	0.25	15.32	1.75	0.03	0.48	2.01	4.24	4.19	0.10	-	0.44	100.2	50.7
CF96-8	73.69	0.22	14.75	1.45	0.03	0.49	1.92	4.4	3.37	0.08	-	0.51	100.91	51
Avg	71.91	0.28	15.14	1.70	0.03	0.54	2.07	4.52	3.66	0.10	-	0.61	-	50.4
Saprolite*														
CF00-04	71.59	0.29	14.54	1.9	0.02	0.4	1.85	4.23	4.11	0.08	0.02	0.75	99.78	50
CF00-05	73.69	0.23	14.48	1.41	0.02	0.36	1.82	4.24	3.94	0.09	0.12	0.57	100.97	50.7
Avg	72.64	0.26	14.51	1.66	0.02	0.38	1.84	4.24	4.03	0.09	0.07	0.66	-	50.3

*Data from Modi (2011)

Table 4. Trace element analyses of Stepladder samples. Element abundances reported in ppm.

	Sediment Samples								Bedrock*	Saprolite*
	CD-1 (1)	CD-1 (2)	CD-1 *Avg.*	CD-2	CD-3	CD-4	CD-5	CD-M	*Avg.*	*Avg.*
Be	2	2	2	2	3	3	3	2	2.6	1.9
Sc	1.5	1.3	1.4	2.8	4	6.2	8.2	16.1	0.62	0.63
V	20	17	18.5	31	38	53	61	928	21.73	17.24
Cr	-	-	-	13	-	32	23	130	1.51	1.33
Co	1	1	1	3	3	6	8	24	1.21	1.18
Cu	20	20	20	10	10	20	50	10	1.99	1.87
Zn	30	30	30	50	50	80	90	230	11.47	16.46
Ga	16	15	15.5	19	23	24	22	46	16.56	15.61
Ge	1.1	1	1.05	1.1	1.3	1.7	1.6	2.2	-	-
Rb	103	94	98.5	108	103	95	95	29	44.56	63.74
Sr	423	390	406.5	431	494	496	421	165	345.3	296.97
Y	4.5	4.2	4.35	8.2	9.3	19.9	25.8	99.7	6.17	4.53
Zr	101	103	102	162	178	242	352	2381	170.2	130.75
Nb	2.50	1.90	2.20	5.50	9.30	8.70	10	58.20	7.42	5.67
Cs	0.60	0.60	0.60	1	1.20	1.70	2.50	0.40	0.97	0.65
Ba	1420	1137	1278.5	813	541	558	626	329	744.02	755.1
La	22.4	21.5	21.95	32.6	30.2	47.6	48.3	1160	21.74	20.39
Ce	42.3	40.7	41.5	63.8	60	95.7	94.9	2440	32.86	32.64
Pr	4.47	4.34	4.4	6.8	6.48	10.5	10.9	231	4.68	4.39
Nd	15.3	15.1	15.2	25	23.5	38.2	39.7	807	16.45	15.1
Sm	2.31	2.38	2.34	4	3.95	7.08	7.73	116	2.63	2.36
Eu	0.63	0.625	0.63	0.77	0.84	1.26	1.38	5.16	0.7	0.64
Gd	1.48	1.51	1.49	2.59	2.79	5.07	5.98	60.4	1.7	1.52
Tb	0.18	0.19	0.18	0.33	0.36	0.7	0.87	6.32	0.22	0.19
Dy	0.85	0.94	0.89	1.72	1.92	3.71	4.65	26.5	1.07	0.94
Ho	0.15	0.16	0.15	0.3	0.33	0.67	0.88	3.79	0.19	0.17
Er	0.45	0.45	0.45	0.84	0.91	1.78	2.46	9.03	0.5	0.44
Tm	0.06	0.06	0.06	0.12	0.13	0.27	0.36	1.07	0.07	0.06
Yb	0.45	0.42	0.43	0.74	0.85	1.78	2.43	6.19	0.46	0.4
Lu	0.07	0.06	0.07	0.1	0.11	0.26	0.38	0.94	0.07	0.06
Hf	2.2	2.1	2.15	4.1	4.6	5.1	5.9	59.3	4.72	3.65
Ta	0.4	0.29	0.34	0.51	0.8	1.06	1.05	5.18	0.47	0.38
Tl	0.37	0.35	0.36	0.42	0.47	0.22	0.31	0.14	0.43	0.42
Pb	10	10	10	12	14	24	24	46	10.33	13.71
Th	6.28	5.73	6	10.8	18.1	14.3	11.3	571	6.61	5.74
U	1.02	0.83	0.92	1.47	2.49	2.1	2.41	37.3	0.29	0.39

*Data from Modi (2011)

and instrumental neutron activation analysis (FUS-ICP/MS; INAA) through Activation Laboratories Ltd. under the Lithogeochemistry Research Package. Detection limits of most major oxides were at 0.01 wt. %, with the exception of Mn and Ti that had detection limits of 0.001 wt. %. A total of 45 trace elements were analyzed in parts per million with detection limits that varied per element.

Approximately 10 mg of each powdered sample was used to determine total carbon and carbonate CO_2 by coulometry with combustion and acid evolution techniques, respectively. Results were corrected for carbonate and phosphate content by subtracting CaO and P_2O_5 from total CaO to obtain the CaO contents in the silicate fraction only. Precision for analytical uncertainty for coulometry was better than 1% for all samples.

5. ANALYSIS OF STEPLADDER BEDROCK AND SAPROLITE

In order to test for the compositional variability between bedrock and locally derived sediment, it is essential to establish a single reference composition of fresh bedrock to compare with the sediment. As both fresh bedrock and saprolite outcrops are exposed throughout the watershed and contribute to sediment production, the petrology and geochemistry of each were also compared to each other to ensure they are compositionally similar. Original geochemical data for bedrock and saprolite come from Modi (2011).

5.1 Stepladder Bedrock

5.1.1 Petrology

In the field, Stepladder bedrock was classified as a compositionally and texturally homogenous, coarse-grained biotite granodiorite with a hypidiomorphic igneous fabric (Fig. 5). The two bedrock thin sections examined (CD-BR1 and CD-BR2) are chiefly composed of plagioclase, followed by quartz, K-feldspar, and biotite (Table 2). In Quartz – Alkali feldspar – Plagioclase (QAP) compositional space (Streckeisen, 1976; Appendix. Fig. D1), bedrock samples CD-BR1 and CD-BR2 are classified as granodiorite, as Modi (2011) also found. Mineralogical variety between the two samples within the granodiorite field can be attributed to how much area on the 25 x 46 mm thin section was accounted for by a single K-feldspar megacryst (typically ranging from 1 – 3 cm; Fig. 5B).

Plagioclase is the most abundant mineral in the Stepladder granodiorite and commonly occurs as euhedral to subhedral megacrysts with distinctive concentric zoning and albite twinning (Fig. 5C). Clay alteration occurs in plagioclase predominately along twinning planes or within calcic zones (Fig. 5C). Potassium feldspar occurs as either

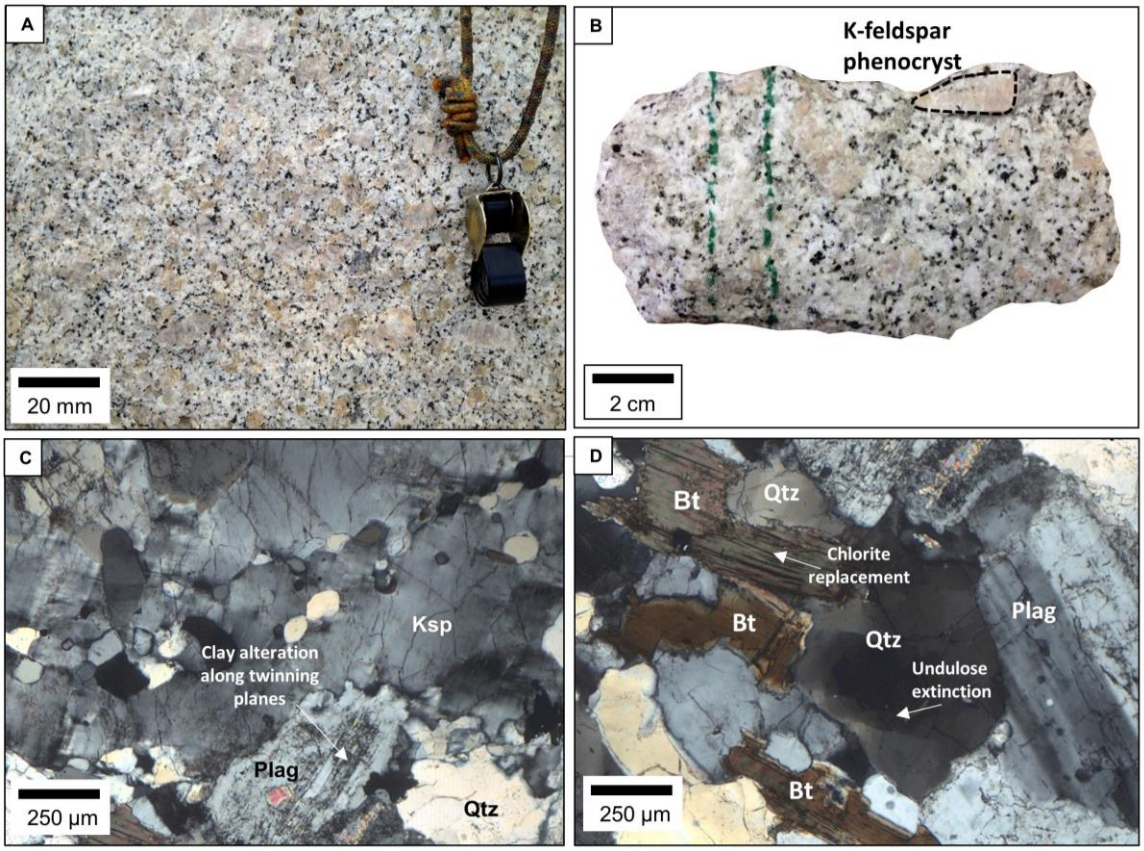

Figure 5A-D. Bedrock field and hand sample photographs and photomicrographs. (A) Surface of fresh Stepladder granodiorite (B) Hand sample of Stepladder granodiorite used for thin sectional analysis. Note size of K-feldspar phenocryst. (C) Photomicrograph of bedrock (crossed polarized) showing slight clay alteration of plagioclase grain. (D) Photomicrograph of bedrock (crossed polarized) showing albite twinning of plagioclase and undulose extinction of quartz. Abbreviations: Plag = plagioclase; Ksp = K-feldspar; Qtz = quartz; Bt = biotite.

subhedral to euhedral perthitic megacrysts or microcline with inclusions of quartz, plagioclase, biotite, and accessory minerals (Fig. 5C). Quartz mostly occurs as subhedral interstitial crystals that commonly exhibit undulatory extinction (Fig. 5D), but also occurs as polycrystalline aggregates. Biotite, the dominant mafic mineral, occurs predominately as elongated interstitial grains (Fig. 5D) or poikilitically included in plagioclase and K-feldspar megacrysts. Minor chlorite replaces biotite crystals along grain boundaries and cleavage planes (Fig. 5D). Accessory phases, such as apatite, zircon, and magnetite, occur either as interstitial grains or as poikilitic inclusions.

5.1.2 Geochemistry

All geochemical data of the Stepladder pluton summarized here come from Modi (2011), where four samples of bedrock were analyzed for major-, trace-, and rare-earth element contents. For this study, the average geochemical composition of the four Stepladder bedrock samples was calculated in order to have a single set of geochemical data to compare with sediment (Tables 3-4).

5.1.2.1 Major Elements

Other than normalized mineralogy, numerous compositional variables and plots can be used to characterize the bedrock. The SiO_2 content of the Stepladder bedrock ranges from 70.7 to 73.7 wt. % with an average of 71.9 % (Table 3). Ratio values of A/CNK (Al_2O_3/CaO+Na_2O+K_2O; Shand, 1943) and A/NK (Al_2O_3/ Na_2O+K_2O; Shand, 1943) ranges from 0.97 to 1.03 and 1.30 to 1.35, respectively (Appendix Table D1). The Aluminum Saturation Index (ASI = Al/Ca – 1.67P + Na + K; Shand, 1943) ranges from 1.48 to 1.54, with an average of 1.50 (Appendix Table D1). The Fe-number (Fe* = FeO_{tot}/ FeO_{tot} + MgO; Miyashiro, 1970) across bedrock samples ranges from 0.71 to 0.76

with an average value of 0.74 (Appendix Table D1). Alkali-lime indices of the bedrock ($Na_2O + K_2O – CaO$; Peacock, 1931) range from 5.84 to 6.42, with an average of 6.11 (Appendix Table D1). Bulk geochemical compositions across all bedrock samples show little variation between each other and are classified as alkali-calcic (Fig. 6A), magnesian (Fig. 6B), peraluminous (Fig. 6C), and alkali granites (Fig. 6D) on different discrimination plots.

5.1.2.2 Trace- and rare-earth elements

When discussing trace-element compositions used in provenance research, elements are commonly divided into the following categories based upon groups of elements with similar geochemical properties: large ion lithophile elements (LILEs; Rb, Ba, Cs, Sr), transition metals (V, Co, Cr), and high field strength elements (HFSEs; Sc, Y, Th, U, Pb, Zr, Hf, Nb, Ti), and rare-earth elements. Trace-element patterns of two bedrock samples normalized to average Upper Continental Crust (UCC; McLennan, 2001) show considerable depletions in Rb, Cs, and U, and are strongly depleted in the transition metals Co, Cr, and Sc (Fig. 7A).

Chondrite-normalized patterns of REEs are conventionally used in provenance work describe the behavior of the LREEs (La, Ce, Pr, Nd, and Sm), HREEs (Gd, Tb, Dy, Ho, Er, Tm, Yb, and Lu), total REE content, and Eu anomaly. Chondrite-normalized REE contents of average Stepladder bedrock generate sub-parallel patterns with little compositional variation between each sample (Fig. 7B). Chondrite-normalized ratios between end-member LREEs, lanthanum and samarium ($La_{CN}/Sm_{CN} = 5.16$), indicate that the LREEs are more fractionated than the HREEs ($Gd_{CN}/Yb_{CN} = 2.98$), with an overall fractionation of (La_{CN}/Yb_{CN}) of 32.1.

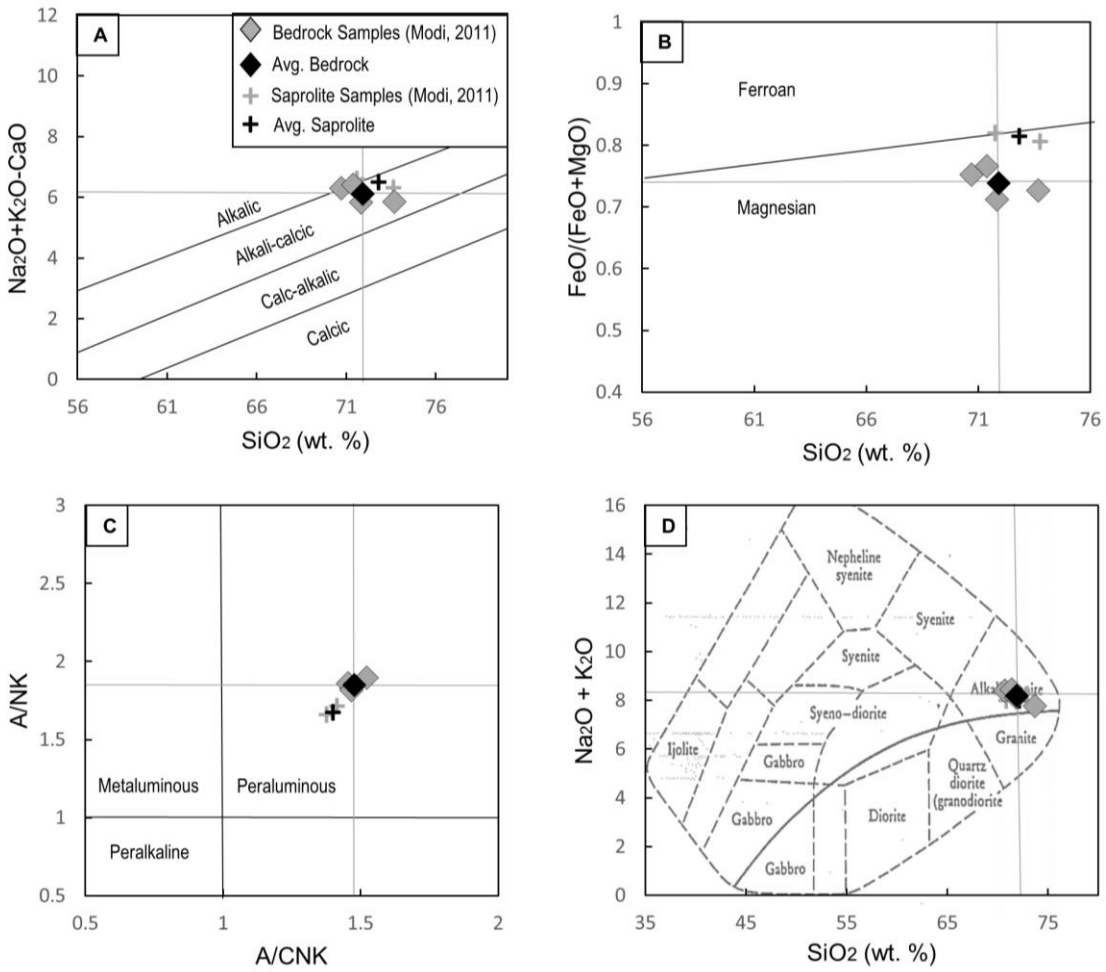

Figure 6A-D. Geochemical plots characterizing Stepladder bedrock and saprolite samples. (A) Na_2O + K_2O –CaO (Alkali-lime index) vs SiO_2 (wt. %) of Frost et al. (2011). (B) $FeO_t/(MgO+FeO_t)$ vs SiO_2 (wt. %) plot of Miyashiro (1974). (C) A/NK vs A/CNK plot of Shand (1943). (D) Na_2O + K_2O vs SiO_2 bedrock classification plot of Cox et al. (1979), where samples plot in the alkali-granite space. All plots use geochemical bedrock data collected by Modi (2011).

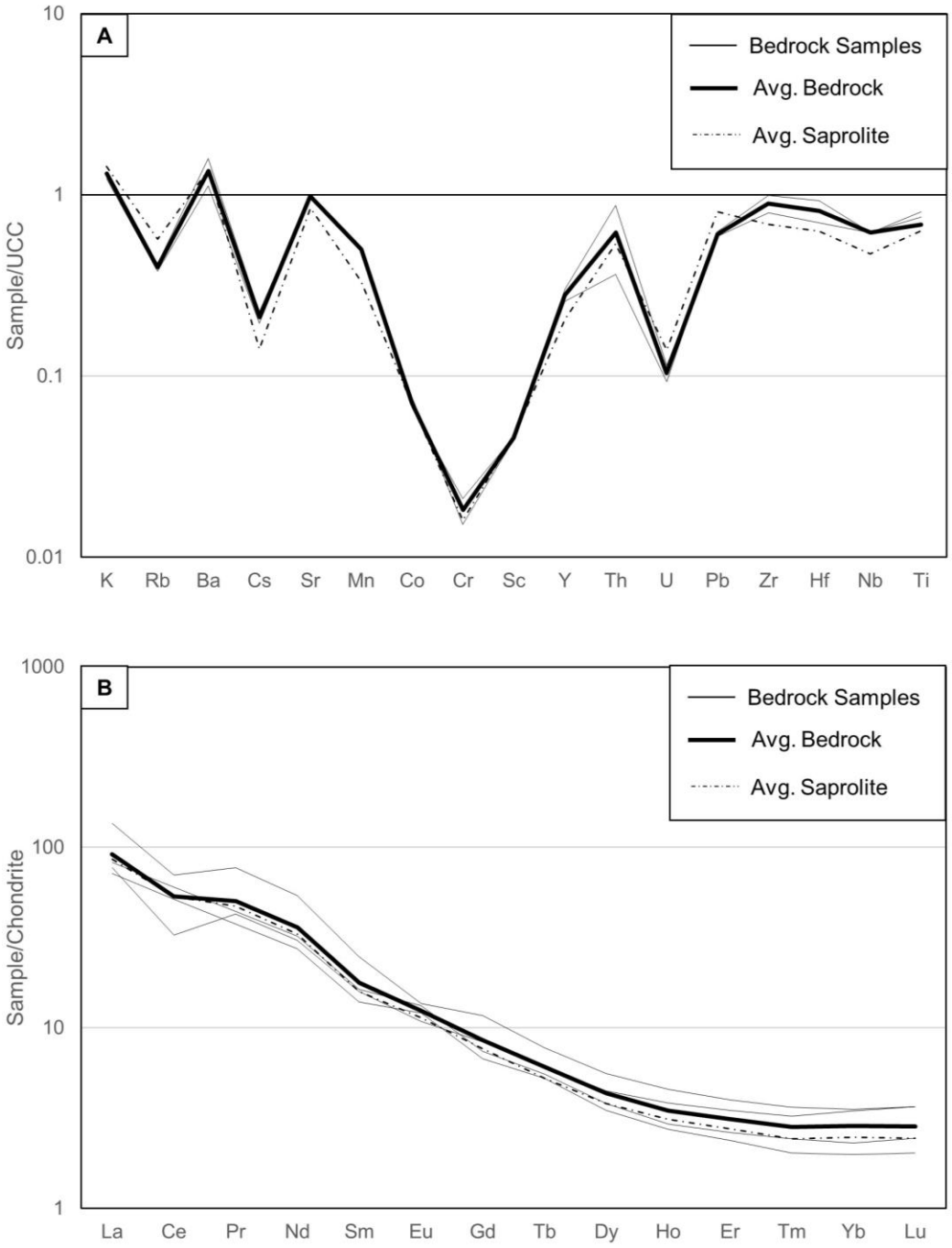

Figure 7A-B. Bedrock and saprolite trace and rare-earth element spider-plots. All geochemical bedrock and saprolite geochemical data from Modi (2011). (A) Bedrock samples and average saprolite trace element contents normalized to Upper Continental Crust (McLennan, 2001). (B) All bedrock samples and average saprolite REE contents normalized to chondrite (McDonough and Sun, 1995).

Europium anomalies are calculated by the geometric average of the ratio of neighboring rare-earth elements Sm and Gd, assuming that the ratio between the neighboring element concentrations remains constant ($Eu^*_{CN} = (Sm_{CN} – Gd_{CN})^{1/2}$; McLennan, 1989). Ratios with values < 1 are considered negative anomalies, whereas ratios > 1 are considered positive anomalies. Average Stepladder bedrock has a negligible Eu anomaly (0.99; Table 5).

Cerium anomalies are calculated by the differences in concentration between neighboring elements Pr and Nd, assuming that the difference in the neighboring elements is constant ($Ce^*_{CN} = 2 * Pr_{CN} – Nd_{CN}$; Lawrence and Kamber, 2006). Average Stepladder bedrock has a slightly negative chondrite-normalized Ce anomaly (0.83; Table 5).

5.2 Stepladder Saprolite

Saprolite is fractured at all scales throughout the watershed and is easily decomposed into sand (Fig. 8A). In contrast to fresh bedrock, saprolite had a brown varnish and a friable texture (Fig. 8B). The following section demonstrates that the saprolite resembles fresh bedrock in terms of both petrology and geochemistry.

5.2.1 Petrology

Despite being fractured, Stepladder saprolite is mineralogically similar to fresh bedrock. In QAP ternary space (Streckeisen, 1976; Appendix Fig. D1), the saprolite sample CD-SAP plots within the granodiorite compositional field with comparable K-feldspar contents observed in the bedrock sample CD-1. The saprolite sample is composed of primarily plagioclase (46%), followed by quartz (22%), orthoclase (25%), and biotite (4%) (Table 2). Observed accessory minerals include magnetite, apatite, and

Table 5. Chondrite- and bedrock-normalized rare-earth element ratios of Stepladder sediment, bedrock, and saprolite samples.

		Sediment Samples						Bedrock*	Saprolite*
		CD-1 *Avg.*	CD-2	CD-3	CD-4	CD-5	CD-M	*Avg.*	*Avg.*
Bedrock Normalized	Eu/Eu^*_{BN}	1.02	0.72	0.77	0.64	0.61	0.19	1.00	1.02
	Ce/Ce^*_{BN}	1.31	1.40	1.36	1.34	1.29	1.49	1.00	1.04
	La_{BN}/Yb_{BN}	1.07	0.93	0.75	0.57	0.42	3.96	1.00	1.08
	Gd_{BN}/Yb_{BN}	0.93	0.95	0.89	0.77	0.67	2.64	1.00	1.03
	La_{BN}/Sm_{BN}	1.13	0.99	0.92	0.81	0.76	1.21	1.00	1.05
Chondrite Normalized	Eu/Eu^*_{CN}	1.03	0.73	0.77	0.64	0.62	0.19	1.01	1.03
	Ce/Ce^*_{CN}	1.09	1.13	1.10	1.09	1.04	1.24	0.83	0.86
	La_{CN}/Yb_{CN}	34.27	29.93	24.13	18.17	13.50	127.30	32.11	34.63
	Gd_{CN}/Yb_{CN}	2.78	2.83	2.66	2.30	1.99	7.89	2.99	3.07
	La_{CN}/Sm_{CN}	5.85	5.09	4.77	4.19	3.90	6.24	5.16	5.39
	∑REE	89.77	139.71	132.38	214.58	220.92	4873.40	83.34	79.30
	LREE Tot	87.52	135.56	127.77	205.41	208.89	4819.56	80.76	77.04
	HREE Tot	2.25	4.15	4.61	9.17	12.03	53.84	2.58	2.26
	LREE/HREE	38.84	32.62	27.68	22.39	17.36	89.51	31.30	34.09

*Data from Modi (2011)

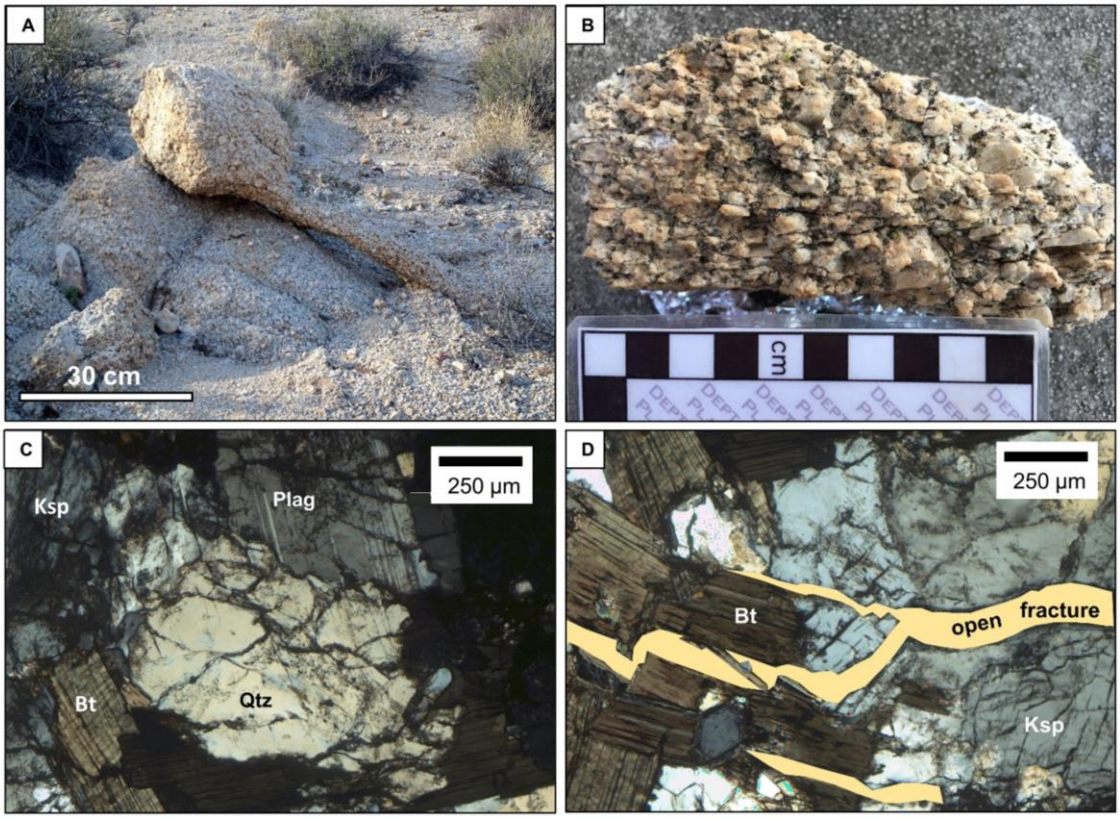

Figure 8A-D. Saprolite field and hand sample photographs and photomicrographs. (A) Weathered field saprolite. Note sediment directly below saprolite. (B) Hand sample of saprolite. Note friable texture. (C) Photomicrograph of saprolite sample under cross polarized light showing condition of mineral surfaces. (D) Photomicrograph of saprolite sample under cross polarized light showing fracture dissecting biotite and K-feldspar. Abbreviations: Plag = plagioclase; Ksp = K-feldspar; Qtz = quartz; Bt = biotite.

zircon. Similar to bedrock, both plagioclase and K-feldspar grains appear slightly cloudy from minor weathering, whereas quartz grains remained largely intact (Fig. 8C).

Fractures in the saprolite dissect grains regardless of mineralogical composition and commonly follow cleavage planes of plagioclase, biotite, and K-feldspar (Fig. 8D), while dissecting grains of K-feldspar and quartz. Large fractures commonly have a thin coat of brown, autochthonous material as well as accumulations of small lithic fragments.

5.2.2 Geochemistry

Saprolite geochemistry is derived from Modi (2011), where two samples were analyzed for major- and trace-element compositions. For this study, the average geochemical composition of the two samples were calculated in order to have a single set of geochemical content to compare with fresh bedrock and sediment (Tables 3-4).

5.2.2.1 Major elements

The SiO_2 contents of the saprolite range from 71.6 to 73.7 wt. %, with an average of 72.6 wt. % (Table 3). Ratio values of A/CNK and A/NK range from 1.43 to 1.45 and 1.74 to 1.77, respectively (Appendix Table D1). The ASI value range from 1.45 to 1.47 (Appendix Table D1). The Fe* values across saprolite samples range from 0.80 to 0.81 (Appendix Table D1). Alkali-lime indexes of the saprolite range from 6.36 to 6.49 (Appendix Table D1). Bulk geochemical compositions of all saprolite samples show little variation between each other, and are classified as alkalic to alkali-calcic (Fig. 6A), slightly ferroan to magnesian (Fig. 6B), peraluminous (Fig. 6C), and alkali granites (Fig. 6D) on different discrimination plots.

5.2.2.2 Trace- and rare-earth elements

The UCC-normalized trace-element pattern of average saprolite closely followed the composition of average bedrock that displayed considerable depletions in Rb, Cs, and U and was heavily depleted in Co, Cr, and Sc (Fig. 7A). Average saprolite chondrite-normalized REE contents possessed a pattern similar to average bedrock with steeply fractionated LREEs (La_{CN}/Sm_{CN} = 5.39; Table 5) relative to HREEs (Gd_{CN}/Yb_{CN} = 3.07; Table 5) (Fig. 7B). Average saprolite had a slightly negative Ce anomaly (0.86; Table 5) and a negligible Eu anomaly (1.03; Table 5).

5.3 Joint Sets

Exposed outcrops of granodioritic bedrock are crosscut by three distinct joint sets, which were observed in outcrops throughout the watershed (Fig. 9). Fracture spacing varied from meter scale (Fig. 9B) to millimeter scale (Fig. 9C). A total of 57 strike-and-dip measurements were taken across the watershed (Fig. 9D; Appendix Table B1) and the orientations plotted on a lower hemisphere equal-area stereonet (Fig. 9E). Out of the three joint sets, the dominant fracture system strikes NE, with a steep vertical-to-SE dip (Fig. 9E). In lesser prevalence, but still readily seen was the NW striking joint set with a steep vertical-to-NE dip (Fig. 9E). The least common joint set strikes NE, with a shallow westward dip (Fig. 9E).

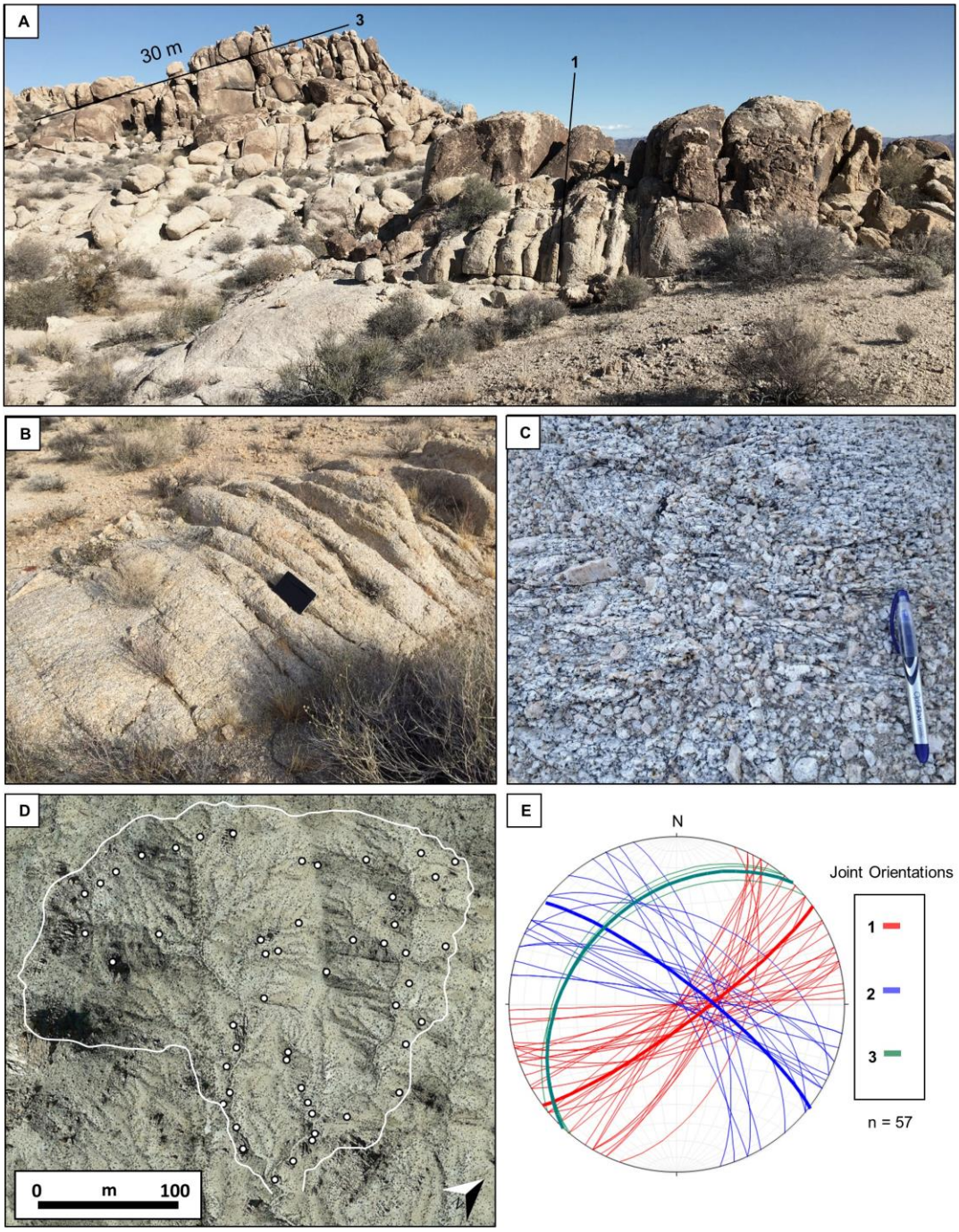

Figure 9A-E. Fracture system field photographs and joint orientations. (A) Field photograph of exposed bedrock in watershed, showing joint sets 1 and 3 (2 not visible from camera angle). (B) Outcrop showing meter scale fractures. (C) Outcrop showing microscale fractures and sediment production. (D) Aerial view of watershed showing location of 50 strike/dip measurements taken in field (white dots). Multiple measurements were taken at some locations. Outline of watershed is delineated in white. (E) Stereonet projection of 57 total measured joints across watershed. Bold projections indicate the average of each joint set.

6. ANALYSIS OF STEPLADDER SEDIMENT

6.1 Textural analysis

All sediment samples were sieved to determine grain-size distribution of each sample. Each sample has an average mean grain size that falls into a unique Φ bin (Fig. 10) based upon the Wentworth grain-size classification scale (Wentworth, 1922). The collective average grain-size distributions of all sediment samples range from very fine gravel to very fine sand ($\bar{x}$ = -1.2 Φ to 3.6 Φ; Table 1). Standard deviation values for each curve do not deviate considerably between samples (σ = 0.7 to 1.8; Table 1). Skewness values of curve shapes between samples range between 0.3 and -0.03 (very fine skewed to symmetrical; Table 1). Kurtosis values range from 1.1 and 0.8 (Table 1).

6.1.1 CD-1

Sediment sample CD-1 is a very fine gravel with a mean grain size of -1.245 Φ (Table 1; Fig. 10), across a range from fine gravel to very coarse silt, with the most abundant clast size being very fine gravel. The sample is a poorly sorted (σ = 1.123), bimodal, sandy gravel, with a fine skewed (*Sk* = 0.365), mesokurtic (*K* = 1.035) grain-size distribution. In terms of grain shape, lithic fragments and monomineralic grains of quartz, plagioclase, and K-feldspar are compact-bladed to compact-elongate, while biotite is platy (Fig. 11A). On average, all grains are angular to sub-angular.

6.1.2 CD-2

Sediment sample CD-2 is a very coarse sand with a mean grain size of -0.726 Φ (Table 1; Fig. 10), across a range from fine gravel to very coarse silt, which is similar to CD-1 with very fine gravel being the most abundant clast size. The sample is a poorly

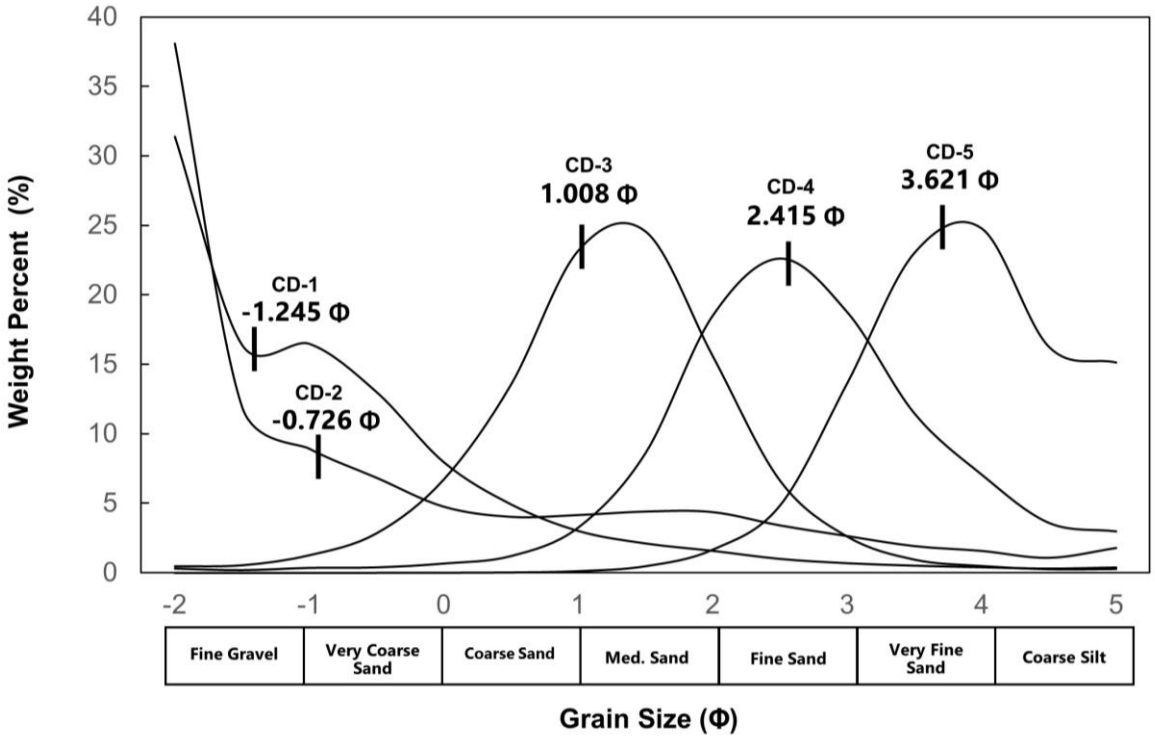

Figure 10. Frequency and cumulative percent distribution curves of the five sediment samples collected across the channel section. Classifications for phi scale from -2 to 5 based on Wentworth scale (Wentworth, 1922).

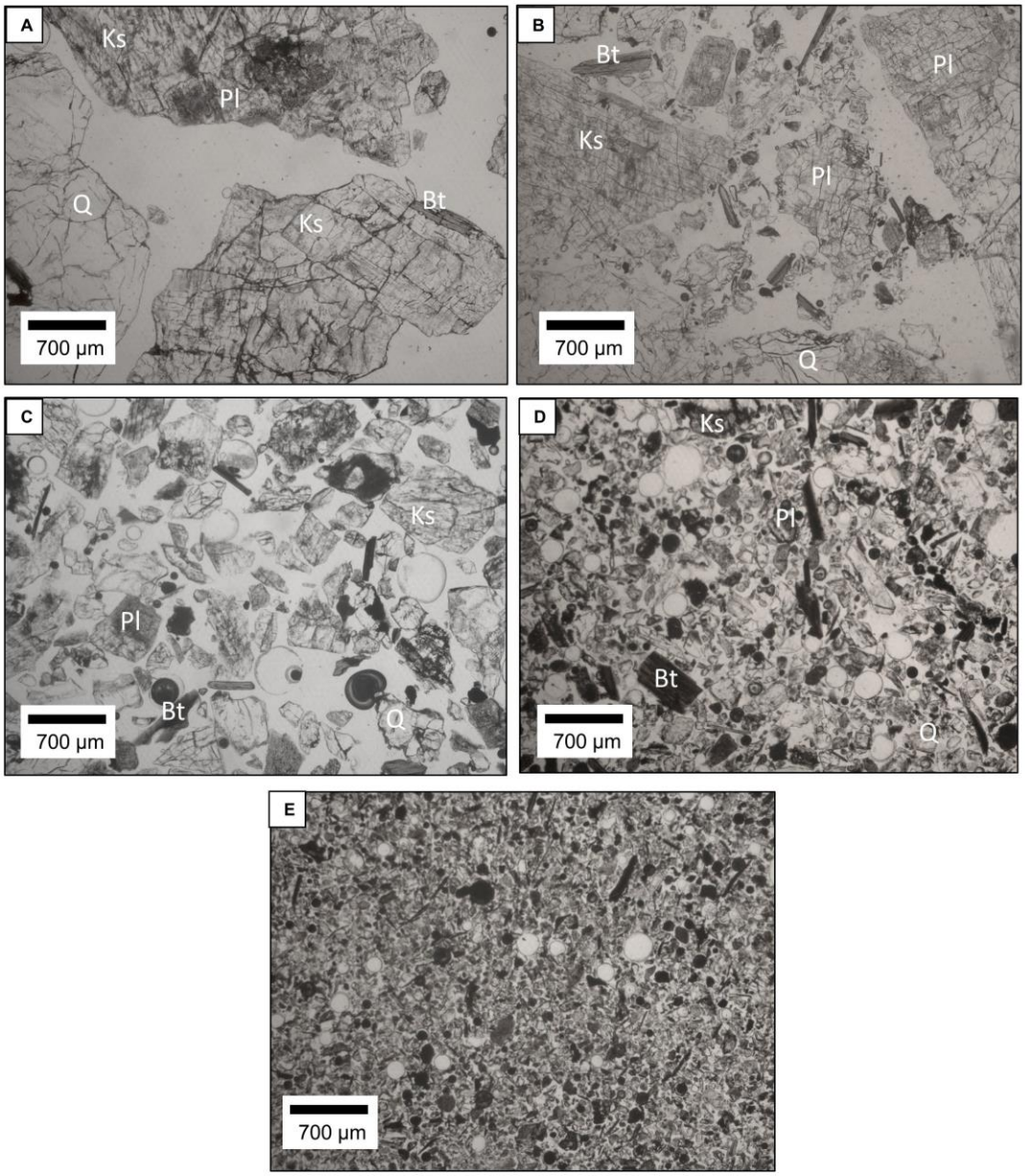

Figure 11A-E. Channel sediment sample photomicrographs. (A) CD-1 – very fine gravel; (B) CD-2 – very coarse sand; (C) CD-3 – medium sand; (D) CD-4 – fine sand; (E) CD-5 – very fine sand. All photomicrographs are in plane polarized light.

sorted (σ = 1.841), unimodal, sandy gravel, with a fine skewed (*Sk* = 0.632), platykurtic (*K* = 0.871), grain-size distribution. In terms of grain shape, lithic fragments and monomineralic quartz, plagioclase, and K-feldspar grains are compact-bladed to compact-elongate, while biotite is platy (Fig. 11B). On average, most grains are angular.

6.1.3 CD-3

Sediment sample CD-3 is a medium sand with a mean grain size of 1.008 Φ (Table 1; Fig. 10), across a range from gravel to very coarse silt. The sample is a moderately sorted (σ = 0.873), unimodal, slightly gravelly sand, with a symmetrical (*Sk* = -0.038), leptokurtic (*K* = 1.128) grain-size distribution. In terms of grain shape, lithic fragments and monomineralic quartz, plagioclase, and K-feldspar grains are compact-bladed, while biotite is platy (Fig. 11C). On average, most grains are sub-angular, while others are angular.

6.1.4 CD-4

Sediment sample CD-4 is a fine sand with a mean grain size of 2.415 Φ (Table 1; Fig. 10), across a range from fine gravel to very coarse silt. The sample is a moderately sorted (σ = 0.980), unimodal, slightly gravelly sand, with a symmetrical (*Sk* = 0.100), leptokurtic (*K* = 1.130) grain-size distribution. In terms of grain shape, lithic fragments and monomineralic quartz, plagioclase, and K-feldspar grains are compact-bladed to compact-elongate, while biotite is platy to bladed (Fig. 11D). On average, most grains are sub-angular, while others are angular.

6.1.5 CD-5

Sediment sample CD-5 is a very fine sand with a mean grain size of 3.621 Φ (Table 1; Fig. 10), across a range from coarse sand to very coarse silt. The sample is a

moderately sorted (σ = 0.794), unimodal, muddy sand, with a symmetrical (*Sk* = -0.010), mesokurtic (*K* = 0.954) grain-size distribution. In terms of grain shape, lithic fragments and monomineralic quartz, plagioclase, and K-feldspar grains are compact-bladed, while biotite is platy (Fig. 11E). On average, most grains are sub-angular, while few are angular.

6.1.6 CD-M

The magnetite concentrate was collected from near the vicinity of the other samples, but in a different channel. Sediment sample CD-M is a medium sand with a mean grain size of 1.729 Φ (Appendix. Table C2), across a range from fine gravel to very coarse silt. The sample is classified as a moderately sorted (σ = 0.895), unimodal, slightly gravelly sand, with a very coarse skewed (*Sk* = -0.370), leptokurtic (*K* = 1.305) grain-size distribution. The sample is largely composed of sub-angular, compact magnetite grains, with some interspersed quartz, feldspar, and biotite.

6.2 Petrography

The mineralogical components of the sediment samples include plagioclase, quartz, K-feldspar, biotite, magnetite, apatite, and zircon. Although the descriptive characteristics of individual minerals (i.e., cloudy surfaces, twinning, chemical zoning, crystal shape, etc.) remain the same between samples, average modal abundances of these minerals vary across samples (Table 2). In particular, there is a systematic depletion of quartz and K-feldspar and an enrichment of plagioclase (Fig. 12A) and biotite (Fig. 12B) from fine to coarse samples.

All counted lithic fragments in sediment samples are amalgamations of the same mineralogical components as found in the Stepladder bedrock. Using the Gazzi-

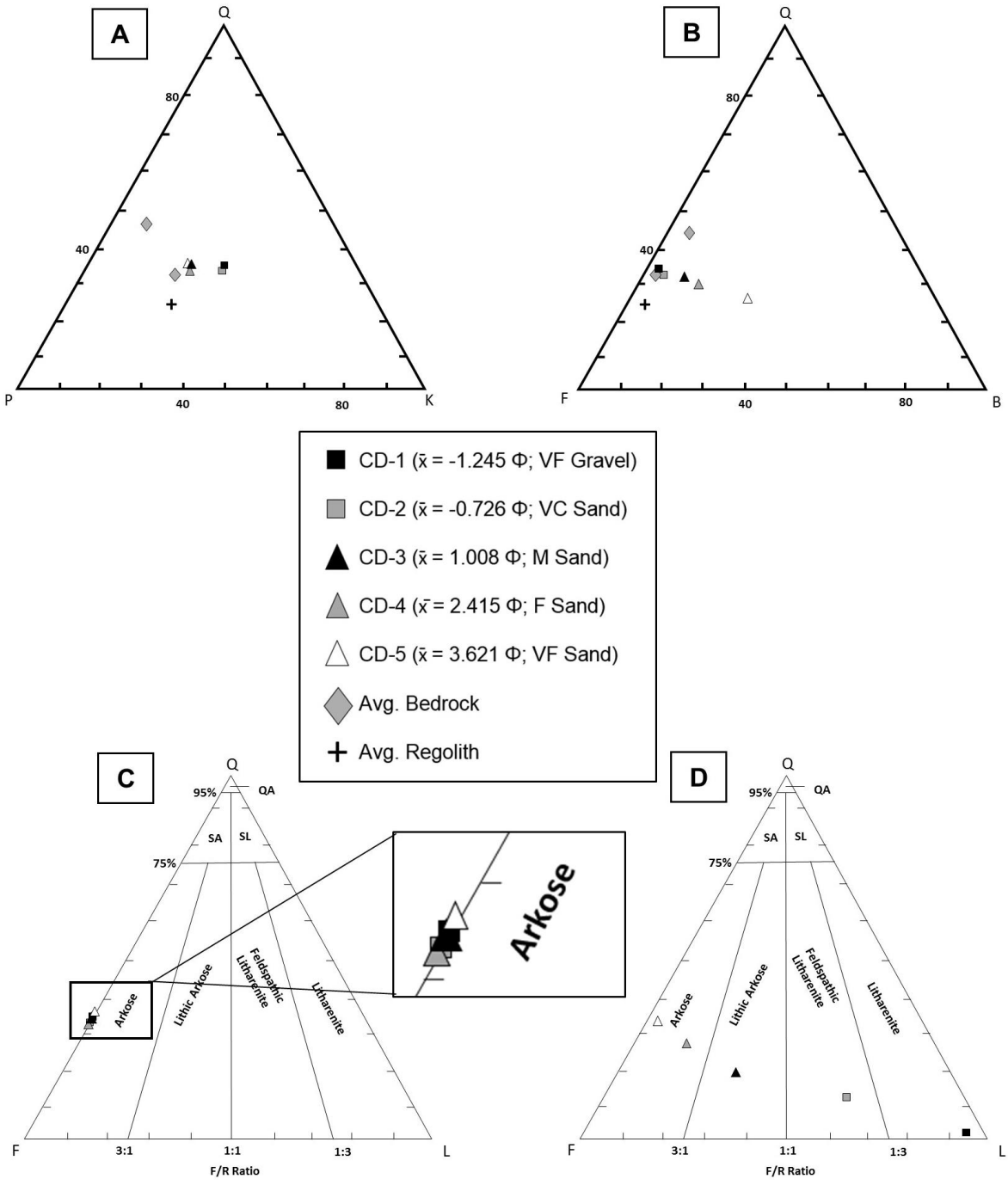

Figure 12A-D. QPK, QFB, and QFL plots of Stepladder sediments. Q = total quartz; F = total plagioclase + K-feldspar; L = total lithic fragments; B = total biotite; P = total plagioclase; K = K-feldspar. (A) QFL rock classification ternary diagram based upon the Gazzi-Dickinson point counting method (Dickinson, 1970; Ingersoll et al., 1984). (B) QFL rock classification ternary diagram based upon the Folk point counting method (Folk, 1974). Abbreviations: QA = quartz arenite; SA = subarkose; and SL = sublithic arenite. (C) QPK ternary plot of Stepladder sediments, bedrock, and saprolite. (D) QFB ternary plot of Stepladder sediments, bedrock, and saprolite.

Dickinson point-counting approach, all sediment samples plot as arkoses in Quartz – Feldspar – Lithic (QFL) space (Fig. 12C). Using the Folk (1974) point-counting approach, sediments plot across litharenite, feldspathic litharenite, lithic arkose, and arkose classifications in QFL space (Fig. 12D). Abundances of lithic fragments systematically decrease from coarser to fine-grained samples (Fig. 12D).

Caliche coats bedrock and fill fractures in saprolite in the Stepladder vicinity (Modi, 2011), and occurs as clasts in the sediment samples. Caliche grains proportionally account for less than 1% of all thin section mineralogy, except for sample CD-3 in which it accounts for 3% of the sample (Table 2).

6.2.1 Quartz

In all samples, quartz occurs as sub-angular to sub-rounded, monocrystalline grains or less commonly as polycrystalline aggregates (Fig. 11A-C). Both straight and undulose extinction is present. As quartz is resistant to alteration, no clay minerals were observed on grains. Quartz is abundant in all collected sediment samples and has a modal abundance that ranges between 32 to 15%. Both monomineralic quartz and quartz incorporated into lithic fragments was found to be more prevalent in coarser-sized samples (CD-1 and CD-2).

6.2.2 Plagioclase

Plagioclase occurs as angular to sub-angular grains. Well-defined albite twinning and oscillatory zoning are distinctive features in nearly all plagioclase grains, which both locally occur in a single grain. As expected (e.g. Nesbitt and Markovics, 1997), the occurrence of minor chemical weathering is more evident in plagioclase than any other mineral in Stepladder sediment, as secondary clays gave grains a cloudy appearance

along twinning planes and the more calcic oscillatory zones. Plagioclase is abundant in all sediment samples, and has a modal abundance that ranges between 18 to 33%. Monomineralic plagioclase grains are particularly prevalent in the finer samples (CD-3, CD-4, and CD-5), whereas lithic fragments containing plagioclase are more common in coarser samples (CD-1 and CD-2). Using the Michel Levy method for determining plagioclase composition, all measured grains across all samples are classified as oligoclase (An_{22} and An_{30}).

6.2.3 K-feldspar

Potassium feldspar in sediment most commonly occurs as perthitic megacrysts, which locally display a slightly cloudy appearance, and suggests that clays have replaced the exsolved plagioclase zones during hydrolysis. In addition to perthite, microcline occurs as angular grains that locally exhibit minor alteration. Both perthite and microcline contain poikilitically included grains of plagioclase, quartz, and accessory minerals. Potassium feldspar increases in modal abundance from fine to coarser sediment samples, and ranges from 11 to 33% (Table 2), respectively. Potassium feldspar grains, as both monomineralic and within lithic fragments, are more prevalent in the coarser sediment samples (CD-1 and CD-2).

6.2.4 Biotite

Biotite grains commonly have a platy shape with frayed edges. Alteration affects many biotite grains through partial replacement by chlorite and Fe-oxides. Biotite increases in modal abundance from coarser to finer grained samples with a range between 3 to 19%. Most commonly, biotite occurs as an monomineralic grain across all samples, except for CD-1, in which it was mostly incorporated in a lithic fragment.

6.2.5 Accessory phases

As with the bedrock, magnetite, apatite, and zircon comprise the dominant accessory phases within the sediment samples. In coarser samples (CD-1, CD-2, and CD-3), accessory phases occur mostly as inclusions in biotite and plagioclase, whereas in finer grained samples (CD-4 and CD-5), magnetite and apatite commonly occur as monomineralic grains. All accessory phases increased in abundance from coarser to finer-grained samples (Table 2).

6.3 Geochemistry

6.3.1 Major elements

There is a decrease in SiO_2 content with decreasing grain size, ranging from 75.2 to 58.8 % from coarser to finer-grained samples (Table 3). Contents of K_2O also decrease with decreasing grain size. An opposite relationship is exhibited by the contents of TiO_2, Fe_2O_3, MgO, CaO, Na_2O, and P_2O_5, all of which are systematically enriched with decreasing grain size (Table 3). Coarser samples CD-1 and CD-2 are considerably depleted in Al_2O_3 relative to finer-grained samples CD-3, CD-4, and CD-5 (Table 3).

6.3.2 Trace-elements

Trace-element contents of all sediment samples were normalized to the average bedrock composition to illustrate differences in sediment composition relative to the known source (Fig. 13A). Elements K, Ba, Sr, Hf, and Nb do not appreciably depart from bedrock composition (less than 5x the average bedrock composition), whereas elements Rb, Cs, Mn, Th, Pb, and Zr are highly variable between sediment samples (Fig. 13A). The greatest departures from average bedrock composition are exhibited by elements Co, Cr, Sc, Y, and U (Fig. 12A) for all samples. As expected for an accessory mineral

concentrate, sample CD-M is enriched with most trace elements, in particular V, Cr, Co, Zr, and the REEs (Table 4).

Samples CD-1 and CD-3 have Cr values below detection limits (< 5 ppm). Values of other elements mineralogically associated with Cr (i.e. Sc, Co, Fe) increase in abundance from coarse to fine-grained samples (Appendix. Fig. D2), suggesting that an analytical anomaly may have caused sample CD-3 to report Cr values below detection limits; by contrast, the actual abundance of Cr in CD-1 is most likely below 5 ppm because bedrock values are < 5 ppm. To determine what the Cr abundances of these two samples may actually be, elemental abundances of Cr in two samples collected by Modi (2011) with similar grain-size distribution curve shapes to CD-1 and CD-3 (Appendix. Fig. C1) were used in an iterative analysis (Appendix. Fig. D3). Here, the Cr abundances of the samples from Modi (2011) were used in conjunction with the Th and Sc abundances collected in this study to be plotted in Cr/Th vs Th/Sc compositional space against values of Cr ranging from 1 to 5. It is clear from this approach that Cr values for CD-1 are actually below detection limits, whereas the low Cr value for CD-3 is most likely an analytical error. Thus, the Cr values from the respective samples from Modi (2011) will be used as proxy abundances for Cr values for samples CD-1 and CD-3 in spider-plots and discrimination diagrams.

6.3.3 Rare-earth elements

In general, the total REE content of each sediment sample increases with decreasing grain size ($\sum$REE = 89.77 to 220.92 ppm; Table 5), as well as total LREE ($LREE_{tot}$ = 87.52 to 208.89 ppm; Table 5) and HREEs ($HREE_{tot}$ = 2.25 to 12.03 ppm; Table 5), which is typical in sedimentary deposits. Values of LREE/HREE decreased

with decreasing grain size (LREE/HREE = 38.84 to 17.36; Table 5), which confirms that finer sediments are enriched with HREEs relative to LREEs.

Although the REE pattern of sample CD-1 most closely resembles the composition of average bedrock (Fig. 13B), fine-grained samples progressively deviate from bedrock composition. Chondrite-normalized REE contents of sediments generate patterns with compositional variations between each sample (Fig. 13C). Chondrite-normalized ratios indicate that the LREEs (La_{CN}/Sm_{CN} = 5.85 to 3.90; Table 5) are overall more fractionated than the HREEs (Gd_{CN}/Yb_{CN} = 2.83 to 1.99; Table 5). Negative Eu anomalies occur in nearly all sediment samples (the exception being sample CD-1; Fig. 13B), where Eu/Eu^*_{CN} values became increasingly more negative with decreasing grain size (Eu/Eu^*_{CN} = 1.03 to 0.62; Table 5).

Sample CD-M is strongly enriched in all REEs ($\sum$REE = 4873.40 ppm, $LREE_{tot}$ = 4819.56 ppm, $HREE_{tot}$ = 53.84 ppm; Table 5) and like the channel sediments, exhibits highly fractionated LREEs (La_{CN}/Sm_{CN} = 6.24; Table 5). However, CD-M exhibits a much steeper slope for HREEs (Gd_{CN}/Yb_{CN} = 7.89; Table 5) than any other sediments. The europium anomaly in sample CD-M is much more negative than any of the other samples (Eu/Eu^*_{CN} = 0.19; Table 5).

Positive Ce anomalies occur in all sediment samples with Ce/Ce^*_{BN}, ranging from 1.29 to 1.49 (Table 5). Positive Ce anomalies have been interpreted to be the result of weathering as Ce^{3+} oxidizes to insoluble Ce^{4+} (Braun and Pagel, 1994). In the case of Stepladder sediments, a positive Ce anomaly is seen across all grain-size populations, which does not considerably change between samples (Fig. 13B). This suggests the Ce anomaly is likely a result of redox processes occurring during weathering.

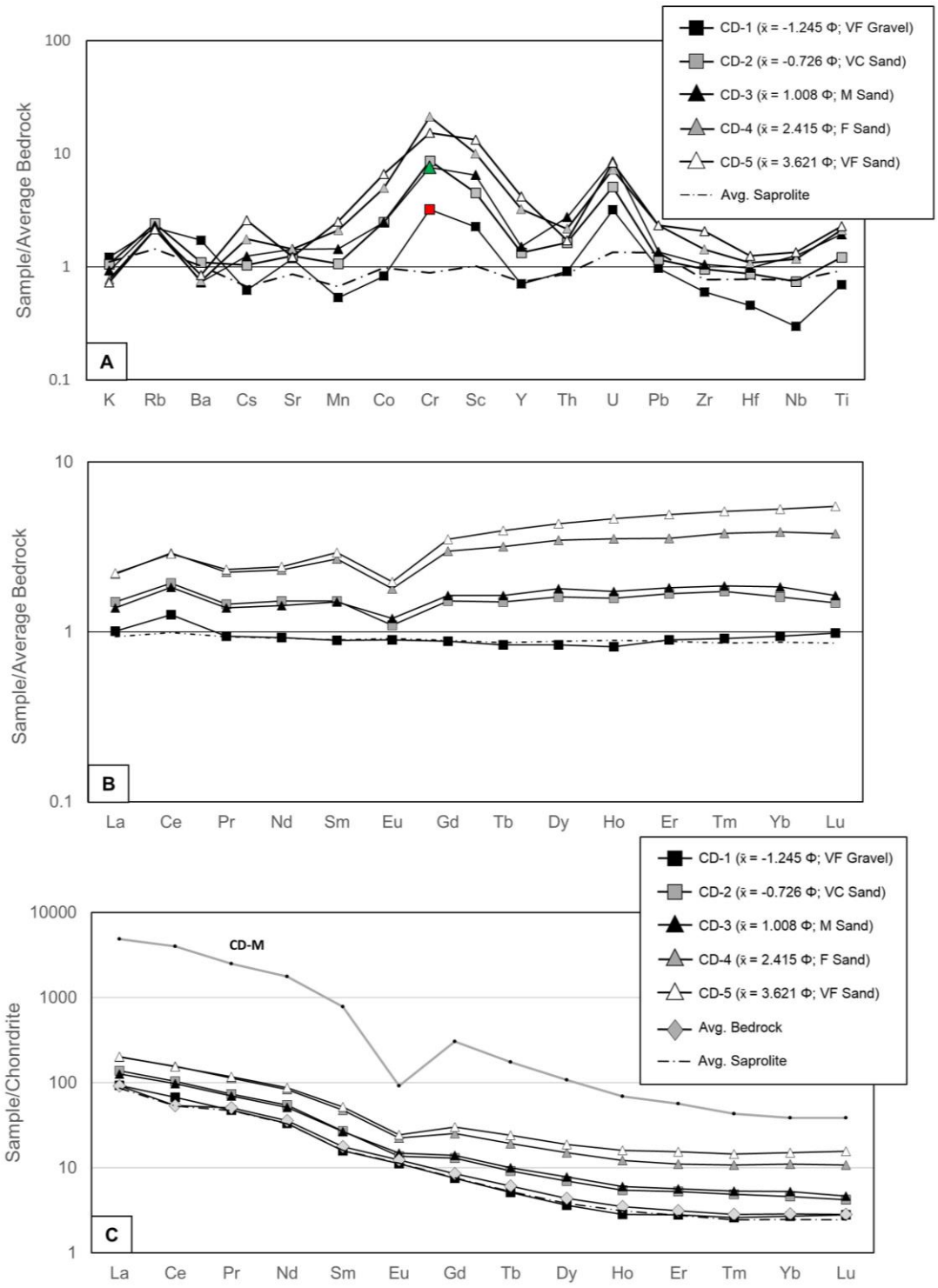

Figure 13A-C. Trace- and rare-earth element plots for Stepladder sediments, saprolite, and bedrock. (A) Trace element contents of sediments, and average saprolite normalized to average Stepladder bedrock. Red square denotes value for Cr derived from Modi (2011) used for CD-1. Green triangle denotes value for Cr derived from Modi (2011) used for CD-3. (B) REE contents of sediments and average saprolite normalized to average Stepladder bedrock. (C) REE contents of sediments, magnetite concentrate CD-M, average saprolite, and average bedrock normalized to chondrite (McDonough and Sun, 1995).

7. EVALUATION OF THE PROCESSES AFFECTING SEDIMENT GEOCHEMISTRY

7.1 Chemical Weathering

The present climate of the Mojave Desert is arid (Stoffer, 2004). Consequently, it is unlikely that compositional and geochemical variations in the modern channel sediments were produced from extensive chemical weathering of Stepladder pluton bedrock. However, to isolate mechanical sorting as the sole cause of compositional variability amongst the collected samples, an examination of the extent of chemical alteration in the studied sediments is needed.

The Al_2O_3–CaO^*+Na_2O–K_2O (A–CN–K) compositional ternary diagram (Fig. 14A; Nesbitt and Young, 1984, 1989; Fedo et al., 1995) has been widely used to evaluate chemical weathering trends. Early stages of chemical weathering begin with the hydrolysis of plagioclase that results in the production of kaolinite, which plots directly on the A apex (Fig. 14A). Thus, samples that endured chemical weathering should have larger proportions of aluminous weathering products and follow a predictable trend towards the A-apex parallel to the A-CN boundary (Nesbitt and Young 1984, 1989; Fig. 14A).

The Chemical Index of Alteration (CIA) is a numerical value between 50 and 100 used as an intensity scale for chemical weathering (Nesbitt and Young, 1982) and is calculated as follows:

$$CIA = (Al_2O_3 / Al_2O_3 + CaO^* + Na_2O + K_2O) * 100 \quad \text{(Eq. 1)}$$

where the oxide values are in molecular proportions, and CaO* is representative of CaO content in silicates only by subtracting apatite and carbonate components

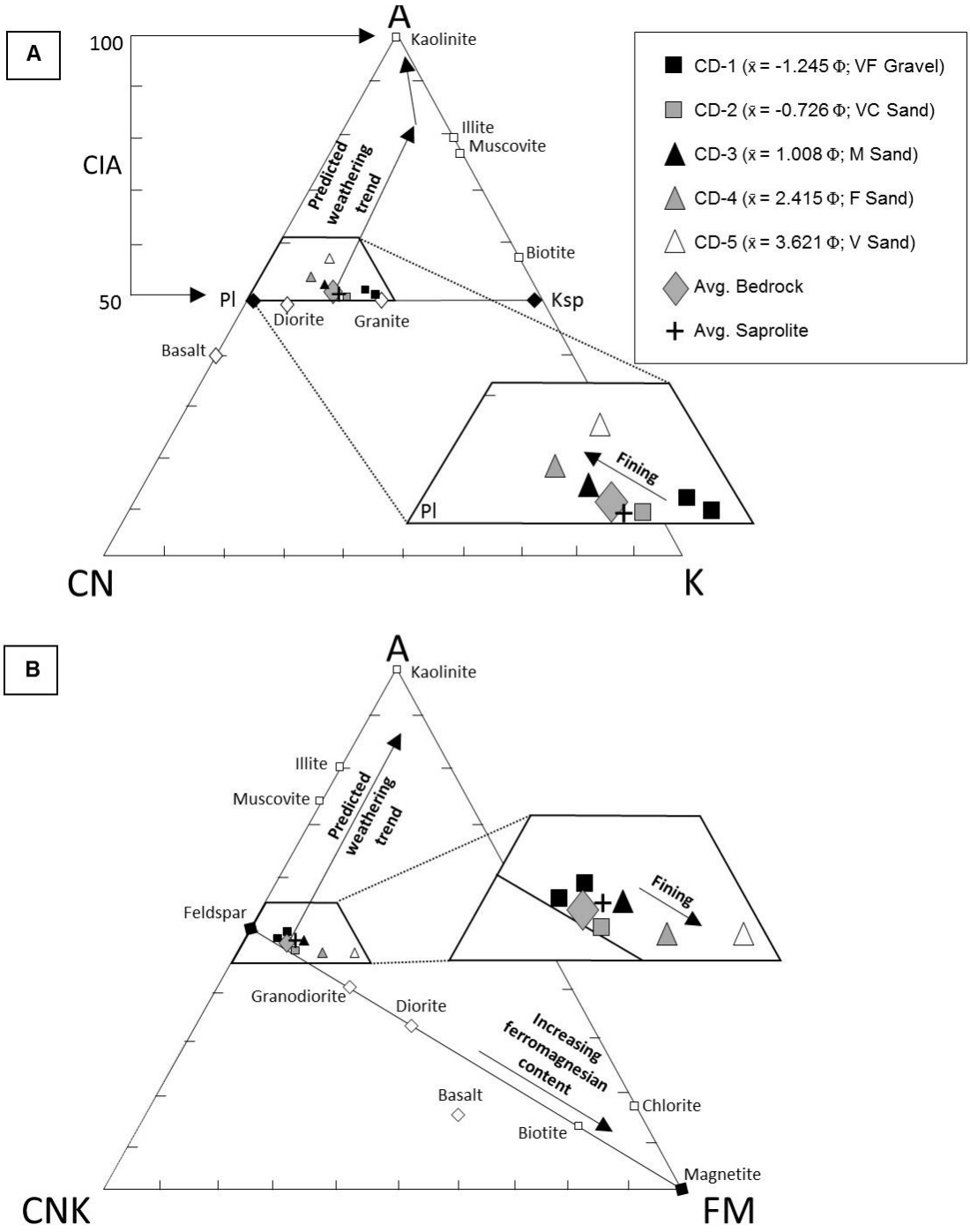

Figure 14A-B. A-CN-K and A-CNK-FM compositional plots for the average Stepladder bedrock, saprolite, and channel sediments. (A) A-CN-K compositional diagram. Note the fining of sediments toward plagioclase composition. (B) A-CNK-FM compositional diagram. Note the fining of sediments toward the FM apex. Both diagrams from Nesbitt and Young (1984, 1989).

($CaO^* = CaO_{tot} – (10/3)P_2O_5 – CO_2$; Nesbitt and Young, 1982, 1989). The CIA values of individual samples represent the A values in A–CN–K space (Fig. 14A). Fresh granitic bedrock and unweathered samples have CIA values of 50, whereas values greater than 80 indicate intense weathering (Fedo et al., 1995).

The four fresh Stepladder bedrock samples have an average CIA value of 50.3 (Table 3), indicating that bedrock has experienced negligible chemical weathering. Similarly, the CIA value of saprolite is also 50.3 (Table 3), demonstrating a lack of geochemical evidence for the chemical weathering of the saprolite. Thus, two possible weathering histories are envisioned for the origin of the saprolite: (1) it formed under wetter climatic conditions prior to the last glacial maximum and is a remnant of the incipient zone of a weathering profile, or (2) it formed in equilibrium with the modern, arid climate of the Mojave Desert. Regardless of either possibility, the saprolite releases modern sediment identical in mineralogical composition to the fresh bedrock.

All sediment samples group along the feldspar join (Fig. 14A), and have CIA values ranging from 50.1 to 56.6 (Table 3). These values indicate that chemical weathering has had some, but overall a very minor effect on sediment composition. Sample CD-5 had the highest CIA value, most likely because any small amount of weathering products being produced from very minor plagioclase dissolution is concentrated in finer grain-size populations during transport. Similar to the A–CN–K diagram is the Al_2O_3–CaO^*+Na_2O+K_2O–FeO+MgO (A–CNK–FM) diagram (Nesbitt and Young, 1989; Fig. 14B), which includes Fe and Mg content. All sediments plot as a group on the feldspar-FM tie line, which implies that no chemical weathering has occurred to the sediment.

7.2 Physical Sorting

There is evidence to suggest that the compositional heterogeneity among samples plotting along the feldspar tie line (Fig. 14A) is controlled by physical sorting. Samples with larger average mean grain sizes (CD-1 and CD-2) plot to the right of average bedrock and contain larger proportions of K-feldspar, whereas samples with smaller average mean grain sizes (CD-3, CD-4, and CD-5) plot left of average bedrock and contain larger proportions of plagioclase, which is similar to findings in Modi (2011). In A–CNK–FM space (Fig. 14B), samples (CD-4 and CD-5) plot preferentially towards the FM apex, which suggests that biotite and magnetite have become depleted in coarser samples and are enriched in fine grained samples. These observations are supported by point-counting data (Table 2), that demonstrate preferential concentration of biotite and magnetite in fine-grained samples.

An explanation for this can be attributed to the differences in textural properties of minerals in the Stepladder bedrock. The hydrodynamic shape of biotite allows it to float in water during transport which increases the likelihood of biotite being sorted apart from quartz and feldpsar during fluvial transport. Magnetite, conversely, has a greater density (~5.15 g/cm^3) than other minerals in the Stepladder bedrock (quartz ~ 2.65 g/cm^3; plagioclase ~ 2.68 g/cm^3; and K-feldspar ~ 2.56 g/cm^3), thus allowing it to become preferentially sorted and concentrated. Considering that biotite and magnetite are both minerals that possibly contain greater proportions of compatible trace elements than quartz or feldspars, it is possible that physical sorting has distorted the immobile element provenance signatures from source composition.

8. EVALUATION OF THE UTILITY OF PROVENANCE INDICATORS

The overarching purpose of this research was to evaluate whether first-cycle sediment that has travelled no further than a few hundred meters from its bedrock source, that experienced no quantifiable chemical weathering, can predict the provenance composition by using conventional geochemical discrimination plots. This becomes a test to determine the extent to which, if at all, physical sorting impacts the geochemical composition of naturally sorted clastic sediment.

More directly, this work questions whether commonly used discriminative plots are representative of actual source compositions, and how accurate past studies that have used bulk geochemistry to interpret the provenance of sandstones (Roser and Korsch, 1999; Armstrong-Altrin et al., 2004; Bakkiaraj et al., 2010) and mudrocks (Cullers, 2000; Bhat and Ghosh, 2001; Lee, 2002; Hofmann et al., 2003) may be. In this study, clastic sediments were collected from a single location in a fluvial channel where the source composition is known. Samples span the types of grain sizes (fine pebbles to coarse silt) that comprise the sedimentary record, and that are commonly used in provenance work. If these samples fail to reconstruct the same, known source composition regardless of grain size, the accuracy of using whole-rock geochemistry to interpret provenance may be more limited by physical sorting than previously thought.

8.1 Major elements

8.1.1 A–CN–K and A–CNK–FM diagrams

In addition to evaluating chemical weathering trends, A–CN–K (Fig. 14A) and A–CNK–FM (Fig. 14B) diagrams can also be used to infer provenance composition by

tracing sediment compositions parallel to the A-CN boundary back to the feldspar tie line (Fedo et al., 1995; Nesbitt and Markovics, 1997). Although Stepladder sediment samples were derived from the same source, sediments separated by grain-size fractions span the compositional range between average compositions of granite, granodiorite, and diorite in A–CN–K space (Fig. 14A). In A–CNK–FM (Fig. 14B) space, fine-grained samples plot closer to more mafic provenances, whereas coarser samples indicate a more felsic source. Reasoning behind these compositional variations can be supported by petrographic observations, which revealed the preferential sorting of plagioclase and biotite in fine-grained sediment fractions. However, interpretations of provenance using these plots would permit a range of possible source compositions.

8.1.2 Discriminant function plots

The compositional plots of Roser and Korsch (1988) incorporate major elements in the form of discriminant functions that distinguish between felsic, intermediate, mafic, or quartzose sedimentary sources of sediment. These discriminant functions are based on the oxides of TiO_2, Al_2O_3, Fe_2O_3, MgO, CaO, Na_2O, and K_2O, which were determined by Roser and Korsch (1988) to be the most effective at differentiating provenance. Sediments plotted in Figure 15A designate a felsic igneous provenance, with fine-grained sediments trending towards a more intermediate composition. To circumvent the problem of CaO and SiO_2 content derived from biogenic sources, Roser and Korsch (1988) developed an alternative plot that uses discriminant functions based on the same major elements, but as ratios with Al_2O_3. This discriminate function plot (Fig. 15B) places bedrock within the intermediate compositional field, and fine-grained sediments trend towards a mafic provenance.

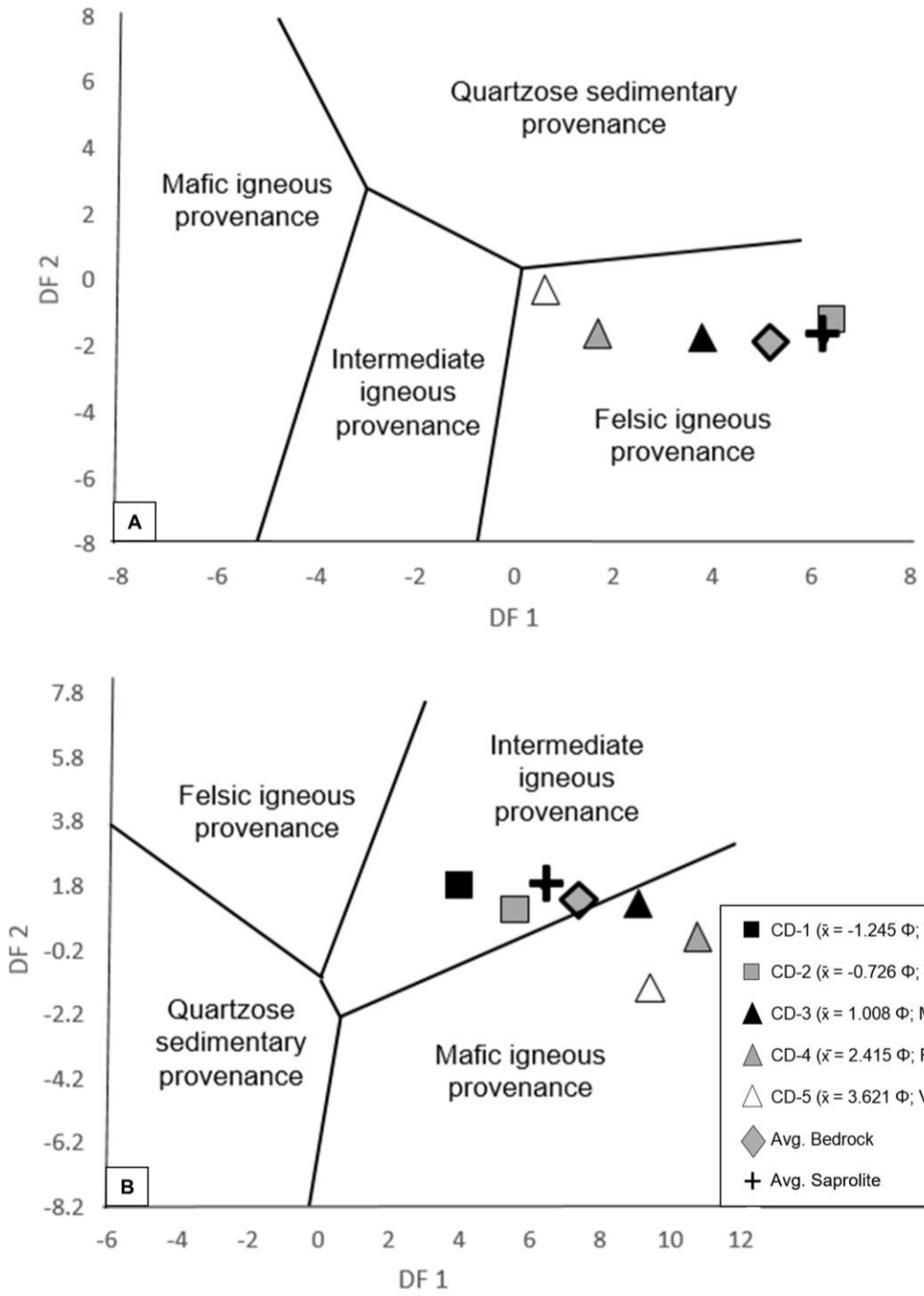

Figure 15A-B. Discriminant function plots used to interpret source compositions of Stepladder sediments. All plots and discriminant functions by Roser and Korsch (1988). (A) Discriminant function plot. DF 1 = (-1.773*TiO_2) + (0.607*Al_2O_3) + (0.76*Fe_2O_3) – (1.5*MgO) + (0.616*CaO) + (0.509*Na_2O) + (-1.22*K_2O) - 0.909 and DF2 = (0.445* TiO_2) + (0.07* Al_2O_3) – (0.25* Fe_2O_3) – (1.142* MgO) + (0.438* CaO) + (0.432*Na_2O) + (1.426*K_2O) - 6.861 (B) Discriminant function plot correcting for biogenic CaO and SiO_2. DF1 = 30.638*(TiO_2/Al_2O_3) - 12.541*(Fe_2O_3/Al_2O_3) + 7.329*(MgO/Al_2O_3) + 12.031*(Na_2O/Al_2O_3) + (35.402*(K_2O/Al_2O_3) - 6.382 and DF2 = 56.5*(TiO_2/Al_2O_3) - 10.879*(Fe_2O_3/Al_2O_3) + 30.875*(MgO/Al_2O_3) - 5.404*(Na_2O/Al_2O_3) + 11.112*(K_2O/Al_2O_3) - 3.89.

As sorting is likely causing these compositional variations across grain-size populations, the utility of these plots in correctly predicting the provenance of sorted sediments from an unknown source composition may be problematic. Despite the compositional variations between samples, the first discriminant plot (Fig. 15A) was successful at predicting a felsic provenance for all sediments, as well as average bedrock. In the case of the alternative discriminative function plot (Fig. 15B), two different igneous provenances can be interpreted across the spectrum of samples derived from the same source. As several studies have used these plots to interpret the source composition of transported sediments (Roser et al., 1996; Bahlburg, 1998; Roser and Korsch, 1999; Oni et al., 2014; Armstrong-Altrin et al., 2015; Eizenhöfer et al., 2015), it should be noted that only coarser-sized sediment fractions (between fine gravel and medium sand) may plot near the actual source composition within an appropriate provenance field.

8.2 Trace elements

8.2.1 Incompatible to compatible element ratio plots

Trace elements are suitable for provenance interpretation in the form of ratios of incompatible and compatible elements. To discriminate between felsic and mafic sources, incompatible elements (La, Th, Hf, Zr) that are abundant in felsic minerals are compared with compatible elements (Sc, Cr, Co) abundant in mafic minerals (Cullers et al., 1988). Thus, when these trace elements of sand-sized sediments are represented as incompatible to compatible element ratios (Th/Sc, La/Sc, Th/Co, La/Co, Cr/Th), they can indicate provenance composition (Taylor and McLennan, 1985; Bhatia and Crook, 1986; Condie and Wronkiewicz, 1990), and more specifically, uncover the relative contribution of felsic to mafic inputs. However, because mineral fractionation can occur during transport

(Fralick and Kronberg, 1997), the use of these ratios and elements to make interpretations of provenance are potentially only valid for locally derived sediments. In order to test if first-cycle sediments from a known source would predict provenance, sediments were plotted in Th/Sc vs Sc ppm, Cr/Th vs Th/Sc, and Th/Co vs La/Sc diagrams along with Stepladder pluton and saprolite reference compositions, probable sources of Meso-Cenozoic basalt, Phanerozoic granite, Meso-Cenozoic andesite, and tonalite-trondhjemite-granodiorite (TTG) (Condie, 1993). All plots include reference lines on average bedrock composition, which forms an end member mixing model with basalt.

In the Th/Sc vs Sc ppm plot (McLennan and Taylor, 1991; Fedo et al., 1996; Fig. 16A), average bedrock has a relatively high Th/Sc value of 10.66, whereas sediment samples exhibit immediately lower Th/Sc values that range from 4.29 to 1.37 from coarse to fine populations. The systematic decrease in Th/Sc values with decreasing grain size occurs because the Sc contents in sediment become enriched up to thirteen times the original bedrock Sc values, whereas Th values in sediment are only enriched up to 1.7 times the original bedrock Th values (Fig. 13A). The coarsest sample, CD-1, even exhibits a considerably low Th/Sc ratio of 4.29, which demonstrates that small, overall contribution of fine-grained sediment in a sample composed of mostly gravel can still distort immobile element signatures. Despite the fact that sediment collected for this study was sourced from a single pluton, the data scatter supports source mixing of the average bedrock and a basaltic end member (Fig. 16A) to produce the ranges of possible sediment compositions observed.

On the Cr/Th vs Th/Sc plot (Condie and Wronkiewicz, 1990; Condie et al., 2001; Fig. 16B), sediments display increasing Cr/Th values with decreasing grain size. This is

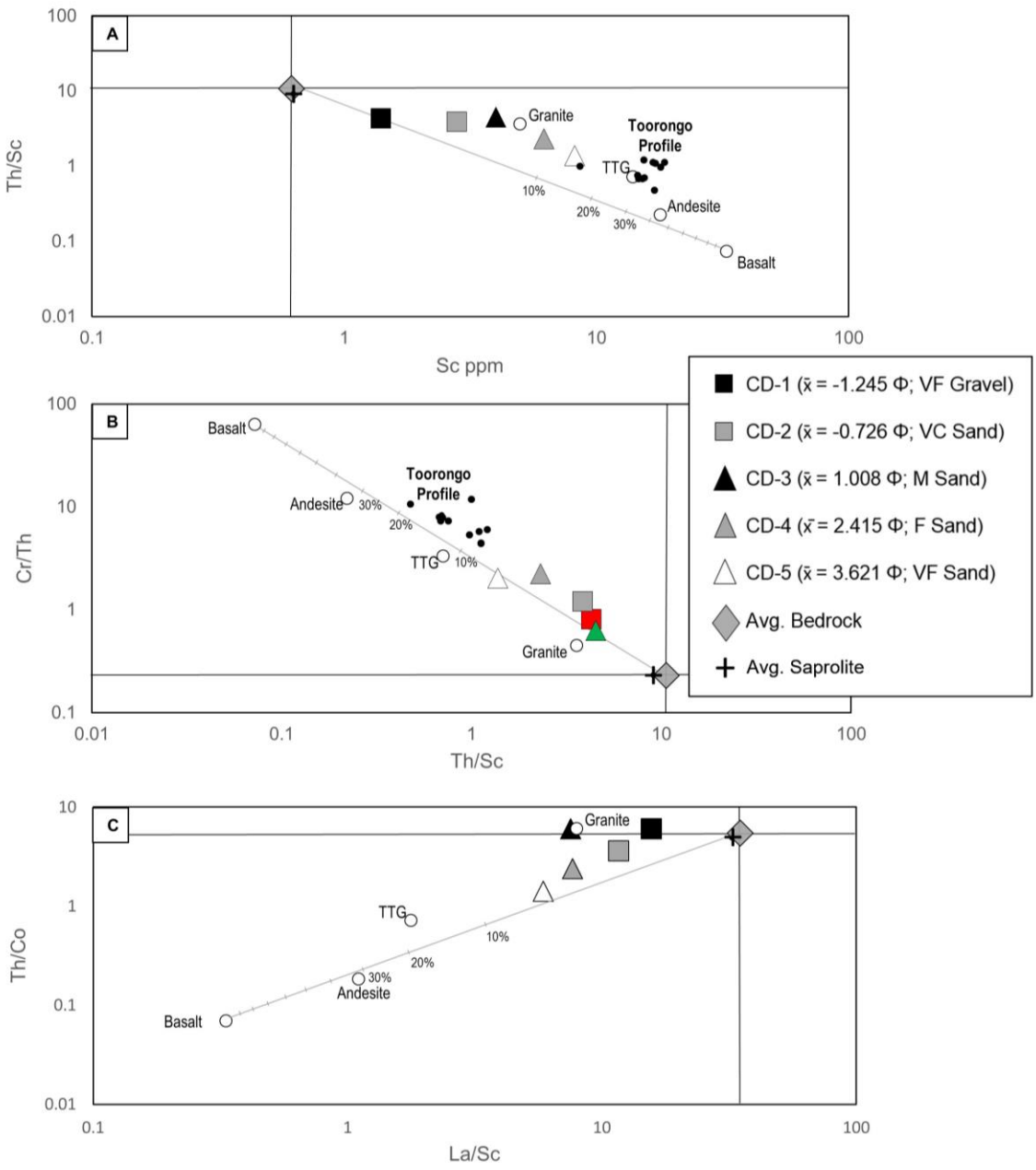

Figure 16A-C. Incompatible to compatible trace element plots of Stepladder sediment, saprolite, and bedrock. (A) Th/Sc vs Sc ppm diagram (B) Cr/Th vs Th/Sc diagram. Red square denotes sample CD-1 that used Cr value from Modi (2011). Green triangle denotes sample CD-3 that used Cr value from Modi (2011). (C) Th/Co vs La/Sc diagram. Reference compositions of average Meso-Cenozoic basalt, Phanerozoic granite, Meso-Cenozoic andesite, and tonalite-trondhjemite-granodiorite (TTG) from Condie (1993). Compositions of samples of the Toorongo granodiorite weathering profile (black dots) from Nesbitt and Markovics (1997).

likely the result of Cr increasing in concentration across decreasing grain sizes, more so than Th (Fig. 13A). The data scatter suggests that sediments are derived from the mixing of greater contributions of mafic components with decreasing grain size. However, it is unlikely that any process other than sorting caused these compositional variations. Saprolite values plot virtually next to the composition of average bedrock, which suggests that sediment transport and natural sorting are primarily responsible for compositional variability.

On the Th/Co vs La/Sc plot (Cullers, 2002; Gu et al., 2002; Oni et al., 2014; Fig. 16C), bedrock and saprolite plot close to each other, whereas sediments begin to deviate towards more mafic compositions. Thorium/cobalt values in sediments become generally lower with decreasing grain sizes whereas La/Sc values increase. These compositional variations can be attributed to how compatible elements, Sc and Co, become strongly enriched with decreasing grain size, relative to the incompatible elements, Th and La (Fig. 13A; Table 4).

Enrichment in compatible elements in fine-grained sediments indicates that the preferential sorting of minerals comprised of these trace elements can cause considerable shifts in provenance interpretations. Elevated transition metal concentrations can be attributed to the "nugget effect" (Wendt and Thomas, 1990), which is caused by the enrichment of a non-abundant mineral in a sediment sample containing trace elements only held within that mineral (in this case, Co, Cr and Sc in biotite). Thus, preferential sorting of biotite in fine-grained sediment sizes leads to elemental enrichments relative to the source composition.

To test if chemical weathering from a similar source composition would result in considerable departures in provenance, a selection of 12 increasingly chemically weathered samples of Toorongo granodiorite profile (range of CIA = 50 – 99) studied in Nesbitt and Markovics (1997) were plotted alongside the Stepladder sediments in the diagrams of Th/Sc vs Sc ppm and Cr/Th vs Th/Sc (no cobalt reported in Toorongo geochemical dataset, thus the Th/Co vs La/Sc plot was excluded). The trend of the increasingly chemically weathered samples from the Toorongo weathering profile show increasing Th/Sc ratios and Sc content with increasing CIA (Fig. 16A), which is a different trend observed from the Stepladder samples from increased sorting. In the Cr/Th vs Th/Sc plot (Fig. 16B), decreasing Cr/Th values correlate with increasing CIA values. Even the most strongly chemically weathered samples of the Toorongo profile (CIA = 99) do not vary from the least weathered samples (CIA = 50) as much as the coarsest sample CD-1 varies from average Stepladder bedrock due to sorting. Thus, using immobile element ratios to interpret source composition of chemically weathered samples is better suited for provenance interpretation than using sediments that have become sorted. Such findings imply that sorting after very minimal transport can fractionate sediments from source composition more so than chemical weathering can.

Despite being locally derived from the same source, Stepladder sediments indicate a wide compositional range between the pluton and the mixing of a generic basaltic end member (Fig. 16A-C), which is similar to Modi's (2011) conclusions. Such outcomes show that, even though immobile trace elements are thought to be quantitatively transferred to the sedimentary record during chemical weathering (e.g. Cullers et al., 1987, 1988; Bhatia and Taylor, 1981; Bhatia and Crook, 1986; Taylor and

McLennan, 1985; Cullers and Stone, 1991; McLennan et al., 1993), mineral sorting, even after minimal transport, can cause these elements to differ from the source material. Of important note, is that the greatest compositional deviations occur in the finest-grained material, which challenges the accuracy of provenance work using these immobile elements to interpret the source of mudstones (Cullers, 2000; Bhat and Ghosh, 2001; Lee, 2002; Hofmann et al., 2003). Furthermore, even the coarsest samples that most closely should resemble bedrock composition contain enough fine-material with mafic trace elements to cause compositional deviations from bedrock. Thus, any work using immobile elements to interpret provenance may be strongly limited by physical sorting regardless of what grain-size population is considered. Bearing in mind that sorting is a process that occurs in all cases of bedload transport, and that many studies have interpreted the provenance of sedimentary rocks or sediments that have travelled further distances than those studied here (Cullers et al., 1988; Slack and Stevens, 1994; Bahlburg, 1998; Bauluz et al., 2000; Roser and Korsch, 1999; Cullers and Podkovyrov, 2000; Condie et al., 2001; Gu et al., 2002; Zimmerman and Bahlburg, 2003; Oni et al., 2014; Eizenhöfer et al., 2015; Xiang et al., 2015), the conventionally accepted notion that certain immobile elements behave as a closed system throughout sedimentary processing is rejected.

8.2.2 Sediment recycling ratio plots

Other trace element ratio plots, such as Th/Sc vs Zr/Sc (McLennan et al., 1993; Fig. 17A), have been used to infer zircon enrichment by sediment recycling over a range of compositions (Bahlburg, 1998; Roser and Korsch, 1999; Zimmerman and Bahlburg, 2003; Oni et al., 2014; Xiang et al., 2015; Moradi et al., 2016). The distribution of

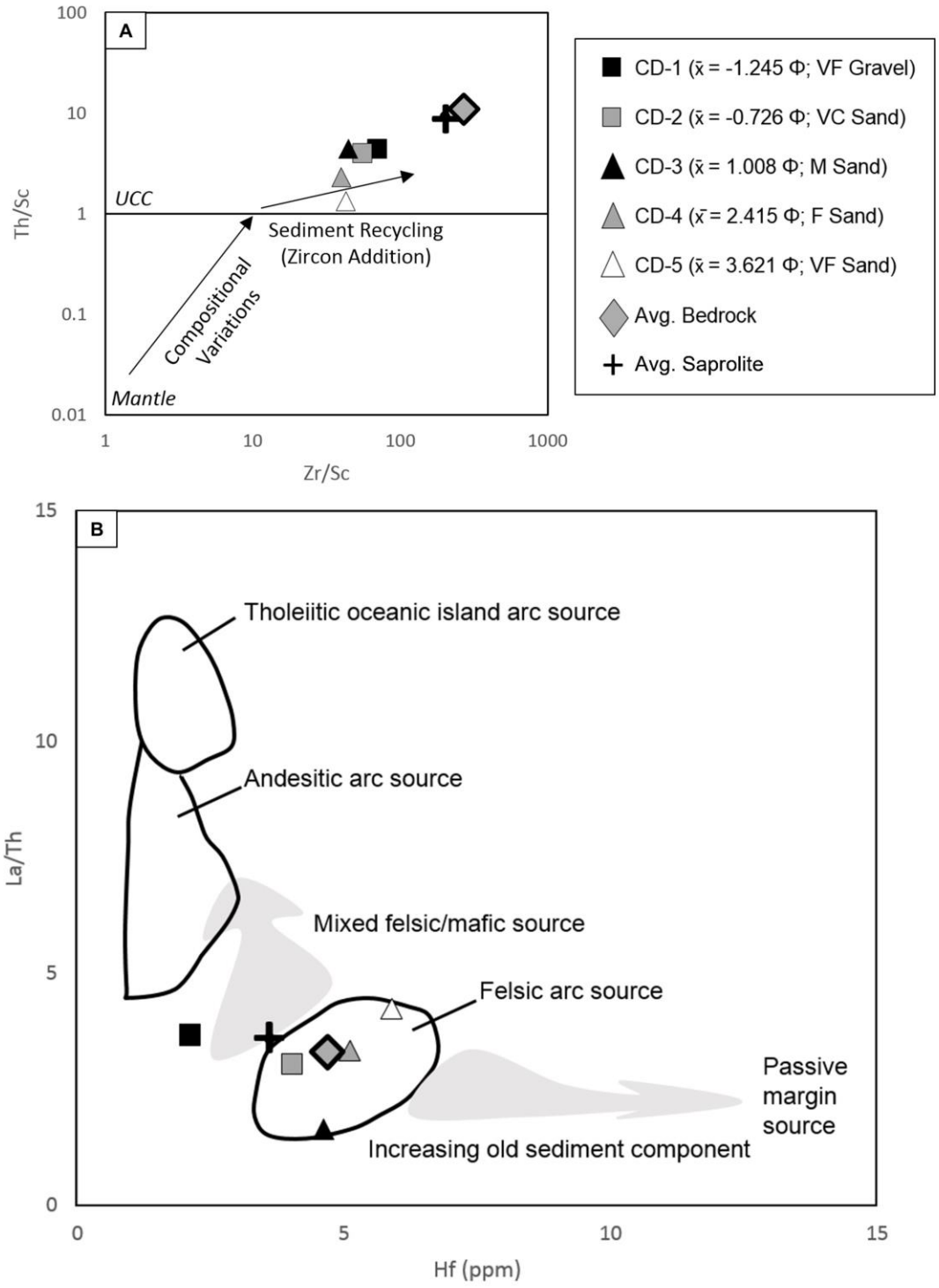

Figure 17A-B. Plots demonstrating extent of sediment recycling. (A) Th/Sc vs Zr/Sc diagram from McLennan et al. (1993). (B) La/Sc vs Hf ppm diagram from Floyd and Leveridge (1987).

Stepladder sediments plotted in the Th/Sc vs Zr/Sc diagram (Fig. 17A) indicates that the sediments were derived from a felsic source, with Th/Sc values ranging between 1 and 10. Sediments have Zr/Sc values that range from 72.8 to 39 from coarser- to fine-grained samples, suggesting varying degrees of recycling across samples. However, bedrock and saprolite Zr/Sc values are much higher, equaling 274.5 and 207.5, respectively. Such variations in the Zr/Sc ratio between sediment and bedrock are likely due to large departures in Sc concentrations from bedrock composition compared to Zr (Fig. 13A). However, increases in Zr/Sc values from fine to coarse samples (Fig. 17A) suggest that the coarser samples endured sediment recycling, despite that all sediments were first cycle materials.

Another common plot, La/Th vs Hf (Floyd and Leveridge, 1987; Fig. 17B), has been used to recognize older sediment components formed by sediment recycling (Gu et al., 2002; Xiang et al., 2015; Moradi et al., 2016). As La/Th is a good indicator of source composition (Taylor and McLennan, 1985), an increasing concentration of Hf in sediment is correlated with zircon enrichment (Floyd and Leveridge, 1987). All sediments except for sample CD-1 correctly plot within the felsic arc source with low La/Th values (between 0 and 5) that are characteristic of felsic compositions (Fig. 17B). Coarser samples show relatively low Hf values, which suggests a non-recycled origin, whereas fine-grained sediment samples have slightly higher values than coarser samples (Fig. 17B). Interestingly, the La/Th vs Hf plot (Fig. 17B) proved to be better at matching sediment compositions to the known source than the Th/Sc vs Zr/Sc plot (Fig. 17A), which is because there are greater departures in Sc from average bedrock relative to those of Zr (Fig. 13A). Thus, the ratio of Zr/Sc is likely sensitive to mineral sorting.

While interpretations of different source compositions and degrees of sediment recycling can be made for the Stepladder samples, all compositional variations can likely be attributed to mostly to physical sorting. Variations in abundances of Zr and Hf across all the Stepladder sediments do not necessarily imply that these sediments had endured varying degrees of recycling, but rather that zircon had become preferentially concentrated in finer grain-size populations during minimal transport. Therefore, it must be understood that sorting does not only hold the capacity to influence the concentrations of transition metals in sediment, but also certain elements held within weathering-resistant minerals.

8.3 Rare-earth elements

Rare-earth elements have been widely considered very useful indicators of provenance under the premise that they are not easily fractionated between sediment and source, and that sources ranging from felsic to ultramafic have distinct REE patterns (Taylor and McLennan, 1985; Cullers, 1988; McLennan and Taylor, 1991). Characteristics of these patterns that describe the slopes of LREEs and HREEs, as well as the magnitude of the Eu anomaly, can be displayed as ratios (La/Sm, Gd/Yb, La/Yb, Eu/Eu*) and have been used as indicators of provenance (Cullers and Podkovyrov, 2000; Slack and Stevens, 1994; Bauluz et al., 2000; Condie et al., 2001; Gu et al., 2002; Zimmerman and Bahlburg, 2003; Oni et al., 2014; Xiang et al., 2015; Armstrong-Altrin et al., 2015; Moradi et al., 2016). Although the Stepladder sediment samples have broadly similar bedrock-normalized REE patterns (Fig. 13B), these ratios, as well as total REE content, depart from bedrock composition with decreasing grain size. To examine the role

of sorting on REE composition, each feature (∑REE, La_{BN}/Sm_{BN}, Gd_{BN}/Yb_{BN}) can be comparatively discussed with Eu/Eu^*_{BN} values (Fig. 18A-C).

8.3.1 Rare-earth element plots

8.3.1.1 Total REE content

Total REE contents of Stepladder sediments increase with decreasing grain size, resulting in sediments plotting between a range of reference compositions, with most samples differing in composition from average bedrock (Fig. 18A). Finer-grained samples, CD-4 and CD-5, most closely resemble the more felsic reference composition of Meso-Cenozoic granite than the known source (Fig. 18A). Coarser-grained samples CD-2 and CD-3 most closely resemble the composition of TTG, but with marginally higher total REE content (Fig. 18A).

Variations in REE content across grain sizes can occur as finer fractions are more likely to be dominated by heavy minerals (Cullers et al., 1987; Cullers et al., 1988). In the case of the Stepladder sediments, increasing total REE content with decreasing grain size may be a result of accessory minerals concentrating in fine-grained sediment populations, as the magnetite concentrate, CD-M, has vastly more REE content (∑REE = 4873.4 ppm) than any other sample. Zircon concentration may also be a factor, as abundances of both Zr and Hf increase from coarse to fine samples (Fig. 13A).

8.3.1.2 Europium anomaly

Four of the sediment samples have a negative Eu anomaly, with Eu/Eu^*_{BN} values that range from 0.72 to 0.61 (CD-2 through CD-5; Table 5). The coarsest sediment sample, CD-1, exhibits a slightly positive Eu/Eu^*_{BN} value of 1.02. Bedrock and saprolite

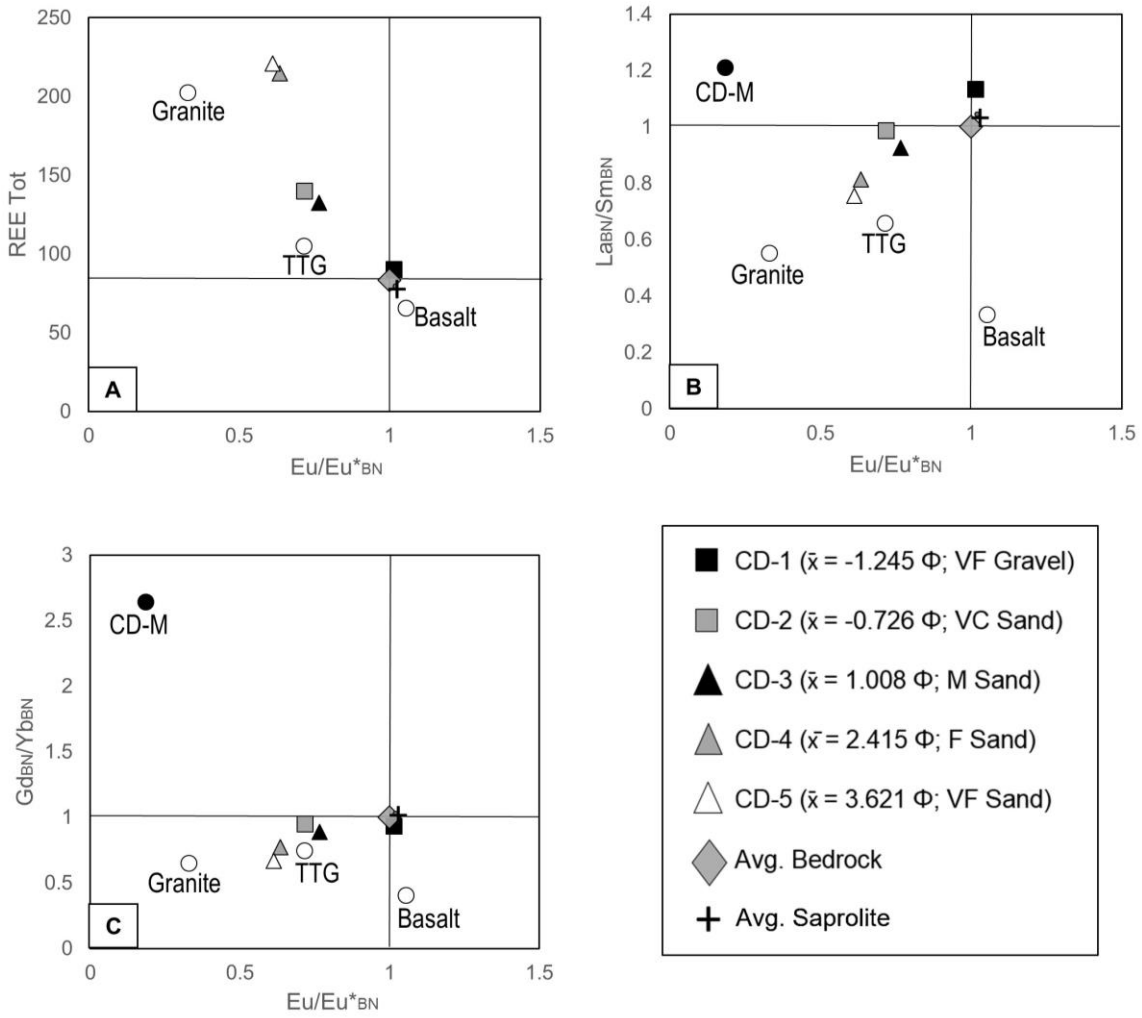

Figure 18A-C. Bedrock-normalized Eu/Eu* plots. All plots from McLennan (1989). (A) REE Total vs Eu anomaly (B) La/Sm vs Eu anomaly (C) Gd/Yb vs Eu anomaly. Reference compositions of average Meso-Cenozoic basalt, Phanerozoic granite, and tonalite-trondhjemite-granodiorite (TTG) from Condie (1993).

Eu/Eu^*_{BN} values are 1.00 and 1.03, respectively, illustrating that a negative europium signature is developed as soon as sediment becomes sorted as coarse sand.

As the magnetite concentrate, sample CD-M, has a strongly negative Eu/Eu^*_{BN} value (Fig. 18B-C), it can be suggested that the preferential sorting of magnetite in finer grain sizes may partly influence the europium signature. It is also possible that zircon enrichment in finer grain-size fractions somewhat controls the Eu anomaly as zircons commonly have depleted Eu signatures relative to Sm and Gd (Trail et al., 2012). This is problematic, however, as pioneering provenance work considers the negative Eu signature to be inherited from a more felsic source than granodiorite (McLennan et al., 1993). As sediments collected in this study range from having no Eu anomaly to a negative one, the value of Eu/Eu* in sorted sediment fractions finer than coarse sand may not necessarily reflect true source composition.

8.3.1.3 LREE and HREE content

Fractionation of LREEs decreases with decreasing grain size (Fig. 18B; La_{BN}/Sm_{BN} = 1.13 for CD-1 to 0.76 for CD-5). Heavy REE fractionation also decreases from coarse to fine sediments (Fig. 18C; Gd_{BN}/Yb_{BN} = 0.93 for CD-1 to 0.67 for CD-5). Decreasing fractionations of both LREEs and HREEs may be due to an enrichment of certain accessory minerals across all samples. However, it is unclear if magnetite may control fractionation behavior, as sample CD-M does not exhibit similar slopes for LREEs and HREEs (Fig. 13C), nor does it have La_{BN}/Sm_{BN} (Fig. 18B) or Gd_{BN}/Yb_{BN} (Fig. 18C) values that show a correlation with decreasing grain size. Conversely, zircon, which increases in abundance with decreasing grain-size fractions (Table 2), may be

responsible for the behavior of increasing HREE slopes as it commonly has high HREE content (Borges et al. 2008; Mahjoor et al., 2009).

For both LREEs and HREEs, finer-grained sediments trend toward more felsic compositions (Fig. 18B-C). Interestingly, this opposes the data scatter in the incompatible to compatible trace element plots (Fig. 16A-C), which indicated finer-grained sediments trend toward more mafic compositions. Such a finding illustrates that there are inconsistencies between interpretations of source composition that can be made, depending on which elements are considered. Consequently, the utility of trace and rare-earth elements as reliable indicators of provenance may be strongly challenged by the impact physical sorting has on sediment composition.

9. SUMMARY AND CONCLUSIONS

1. The goal of this study was to test the effectiveness of commonly used geochemical and petrographic techniques applied to provenance interpretations for sediment produced from a known source and subsequently sorted during minimal fluvial transport. The Stepladder Mountains in the Mojave Desert, CA, reside in an arid setting where modern sediments within an enclosed drainage basin should ideally resemble the single, known source because of essentially minimal chemical weathering and transport. Previous work by Modi (2011) has shown that sediments are naturally sorted by grain size in fluvial channels that dissect the source region. The hypothesis tested was that if sediments could be substantially sorted by grain size after only meters of transport in an arid climate, then they would exhibit mineralogical and thus, geochemical deviations from the known source.
2. Within the watershed, five sediment samples were collected across a single channel and had become sorted into five distinct grain-size populations. Every sediment sample, despite mean grain size differences, comprised the same mineralogy as the granitic bedrock, which consisted of plagioclase, K-feldspar, quartz, and biotite. Accessory minerals include magnetite, apatite, and zircon. Coarser sediments (CD-1 and CD-2) were enriched in quartz, whereas fine-grain sediments (CD-3, CD-4, and CD-5) were enriched in plagioclase, biotite, and magnetite.
3. The low CIA values in both sediment and bedrock indicate that the degree of chemical weathering influencing sediment composition is negligible. However,

data suggest that if a small amount weathering products were present, they are concentrated in finer grain sizes. Fractionation of FeO and MgO from Al_2O_3, CaO, Na_2O, and K_2O occurs during transport, and biotite and magnetite were concentrated in fine-grained samples.

4. Trace-element plots normalized to average bedrock show strong departures in Cr, Co, and Sc which are thought to be immobile during sedimentary processing, and thus are commonly used as components in provenance discriminating ratios. Sediment ratios successfully interpret the felsic source composition of the bedrock. However, fine-grained samples reveal preferential trends toward mafic compositions. Several trace-element ratios, La/Sc, Th/Sc, Th/Co reveal that sediment may have acquired its composition from the mixing of a basaltic compositional end member with the actual source to produce the composition of the fine-grained sediment. Samples of the fresh and chemically weathered components of a weathering profile indicated that sorting has a greater effect on distorting the expected outcomes of ratios using immobile elements than chemical weathering does. Particular diagrams, Th/Sc vs Zr/Sc and La/Th vs Hf ppm, successfully indicate that appreciable sediment recycling has not occurred, but demonstrate any ratios using supposedly immobile elements, such as Sc, cause sediments to deviate from source composition. Coarser samples had greater Zr/Sc ratios, and thus appeared to have undergone greater sediment recycling than fine-grained samples.
5. Rare-earth element patterns normalized to average bedrock show that sediments with decreasing grain sizes have increasingly greater total REE content, negative

Eu anomalies, and fractionated LREE and HREE slopes. High rare-earth element contents of the magnetite concentrate, sample CD-M, suggest that increasing proportions of magnetite in fine-grained samples may control total REE content. Variations in the strength of the Eu anomaly, as well as the LREE and HREE contents across samples, may be controlled by accessory mineral concentration as magnetite, zircon, and apatite increase in modal abundance in the finer grain sizes.

6. Despite that the diagrams used in this study are thought to be insensitive to sedimentary processing, the only factor responsible for causing the composition of these sediment samples to deviate from another or bedrock is mineral sorting during less than 0.1 km of transport. This work shows that sediment sorting is capable of inducing compositional and geochemical changes between source and sediment, even within trace elements, and that these changes begin to take effect immediately within the source terrain. Therefore, the ability to accurately reconstruct provenance from sediment deposited at any distance from the source rock may be more problematic than previously recognized. Henceforth, provenance evaluation should consider the influence of fluvial sorting on sediment composition.

REFERENCES CITED

Anderson, J.L. and Bender, E.E., 1989. Nature and origin of Proterozoic A-type granitic magmatism in the southwestern United States of America. Lithos, v. 23, no. 1, p. 19-52.

Anderson, J.L. and Cullers, R.L., 1990. Middle to upper crustal plutonic construction of a magmatic arc; an example from the Whipple Mountains metamorphic core complex. Geological Society of America Memoirs, v. 174, p. 47-70.

Armstrong-Altrin, J. S., Lee, Y. I., Verma, S. P., and Ramasamy, S., 2004. Geochemistry of sandstones from the upper Miocene Kudankulam Formation, southern India: Implications for provenance, weathering, and tectonic setting. Journal of Sedimentary Research, v. 74, no. 2, p. 285-297.

Armstrong-Altrin, J.S., Machain-Castillo, M.L., Rosales-Hoz, L., Carranza-Edwards, A., Sanchez-Cabeza, J.A. and Ruíz-Fernández, A.C., 2015. Provenance and depositional history of continental slope sediments in the Southwestern Gulf of Mexico unraveled by geochemical analysis. Continental Shelf Research, v. 95, p. 15-26.

Bahlburg, H., 1998. The geochemistry and provenance of Ordovician turbidites in the Argentine Puna. Geological Society, London, Special Publications, v. 142, no. 1, p. 127-142.

Bakkiaraj, D., Nagendra, R., Nagarajan, R. and Armstrong-Altrin, J.S., 2010. Geochemistry of sandstones from the Upper Cretaceous Sillakkudi Formation, Cauvery Basin, southern India: implication for provenance. Journal of the Geological Society of India, v. 76, no. 5, p. 453-467.

Basu, A.R., 1976. Petrology of Holocene fluvial sand derived from plutonic source rocks; implications to paleoclimatic interpretation. Journal of Sedimentary Research, v. 46, p. 694–709.

Basu, A., 1985. Influence of climate and relief on compositions of sands released at source areas. In Provenance of Arenites, Springer Netherlands, v. C-148, p. 1-18.

Bauluz, B., Mayayo, M.J., Fernandez-Nieto, C. and Lopez, J.M.G., 2000. Geochemistry of Precambrian and Paleozoic siliciclastic rocks from the Iberian Range (NE Spain): implications for source-area weathering, sorting, provenance, and tectonic setting. Chemical Geology, v. 168, no. 1, p. 135-150.

Bhat, M.I. and Ghosh, S.K., 2001. Geochemistry of the 2.51 Ga old Rampur Group pelites, western Himalayas: implications for their provenance and weathering. Precambrian Research., v. 108, p. 1-16.

Bhatia, M.R., 1983. Plate tectonics and geochemical composition of sandstones. The Journal of Geology, v. 91, p. 611-627.

Bhatia, M. R., and Crook, K. A., 1986. Trace element characteristics of graywackes and tectonic setting discrimination of sedimentary basins. Contributions to mineralogy and petrology, v. 92, no. 2, p. 181-193.

Blott, S.J. and Pye, K., 2001. GRADISTAT: a grain size distribution and statistics package for the analysis of unconsolidated sediments. Earth Surface Processes and Landforms, v. 26, p. 1237-1248.

Borges, J.B., Huh, Y., Moon, S. and Noh, H., 2008. Provenance and weathering control on river bed sediments of the eastern Tibetan Plateau and the Russian Far East. Chemical Geology, v. 254, no. 1, p.52-72.

Braun, J.J. and Pagel, M., 1994. Geochemical and mineralogical behavior of REE, Th and U in the Akongo lateritic profile (SW Cameroon). Catena, v. 21, no. 2, p.173-177.

Condie, K.C., Noll, P.D. and Conway, C.M., 1992. Geochemical and detrital mode evidence for two sources of Early Proterozoic sedimentary rocks from the Tonto Basin Supergroup, central Arizona. Sedimentary Geology, v. 77, no. 1, p. 51-76.

Condie, K.C., Lee, D. and Farmer, G.L., 2001. Tectonic setting and provenance of the Neoproterozoic Uinta Mountain and Big Cottonwood groups, northern Utah: constraints from geochemistry, Nd isotopes, and detrital modes. Sedimentary Geology, v. 141, p. 443-464.

Condie, K.C. and Wronkiewicz, D.J., 1990. The Cr/Th ratio in Precambrian pelites from the Kaapvaal Craton as an index of craton evolution. Earth and Planetary Science Letters v. 97, p. 256–267.

Condie, K.C., 1993. Chemical composition and evolution of the upper continental crust: contrasting results from surface samples and shales. Chemical geology, v. 104, no. 1, p. 1-37.

Cox, K.G., Bell, J.D. and Pankhurst, R.J., 1979. The Interpretation of Igneous Rocks, Springer Netherlands, p. 42-82.

Cullers, R., 1988. Mineralogical and chemical changes of soil and stream sediment formed by intense weathering of the Danburg granite, Georgia, USA. Lithos, v. 21, no. 4, p. 301-314.

Cullers, R. L., 1994. The chemical signature of source rocks in size fractions of Holocene stream sediment derived from metamorphic rocks in the wet mountains region, Colorado, USA. Chemical Geology, v. 113, no. 3, p. 327-343.

Cullers, R.L., 2000. The geochemistry of shales, siltstones and sandstones of Pennsylvanian– Permian age, Colorado, USA: implications for provenance and metamorphic studies. Lithos, v. 51, p. 181– 203.

Cullers, R. L., 2002. Implications of elemental concentrations for provenance, redox conditions, and metamorphic studies of shales and limestones near Pueblo, CO, USA. Chemical Geology, v. 191, no. 4, p. 305-327.

Cullers, R.L., Barrett, T., Carlson, R. and Robinson, B., 1987. Rare-earth element and mineralogic changes in Holocene soil and stream sediment: a case study in the Wet Mountains, Colorado, USA. Chemical geology, v. 63, no. 3, p. 275-297.

Cullers, R.L., Basu, A. and Suttner, L.J., 1988. Geochemical signature of provenance in sand-size material in soils and stream sediments near the Tobacco Root batholith, Montana, USA. Chemical Geology, v. 70, no. 4, p. 335-348.

Cullers, R.L. and Podkovyrov, V.N., 2000. Geochemistry of the Mesoproterozoic Lakhanda shales in southeastern Yakutia, Russia: implications for mineralogical and provenance control, and recycling. Precambrian Research, v. 104, no. 1, p. 77-93.

Cullers, R.L. and Stone, J., 1991. Chemical and mineralogical comparison of the Pennsylvanian Fountain Formation, Colorado, USA (an uplifted continental block) to sedimentary rocks from other tectonic environments. Lithos, v. 27. no. 2, p. 115-131.

DeWitt, E.D., Armstrong, R.L., Sutter, J.F. and Zartman, R.E., 1984. U-Th-Pb, Rb-Sr, and Ar-Ar mineral and whole-rock isotopic systematics in a metamorphosed granitic terrane, southeastern California. Geological Society of America Bulletin, v. 95, no. 6, p. 723-739.

Dickinson, W.R., 1970. Interpreting detrital modes of graywacke and arkose. Journal of Sedimentary Petrology, v. 40, p. 695–707.

Dickinson, W.R., Beard, L.S., Brakenridge, G.R., Erjavec, J.L., Ferguson, R.C., Inman, K.F., Knepp, R.A., Lindberg, F.A. and Ryberg, P.T., 1983. Provenance of North American Phanerozoic sandstones in relation to tectonic setting. Geological Society of America Bulletin, v. 94, no. 2, p. 222-235.

Dickinson, W.R. and Suczek, C.A., 1979. Plate tectonics and sandstone compositions. The American Association of Petroleum Geologists Bulletin, v. 63, p. 2164–2182.

Dickinson, W. R., and Valloni, R., 1980. Plate settings and provenance of sands in modern ocean basins. Geology, v. 8, no. 2, p. 82-86.

Dickinson, W. R., Beard, L. S., Brakenridge, G. R., Erjavec, J. L., Ferguson, R. C., Inman, K. F., and Ryberg, P. T., 1983. Provenance of North American Phanerozoic sandstones in relation to tectonic setting. Geological Society of America Bulletin, v. 94, no. 2, p. 222-235.

Dohrenwend, J. C., 1988. Age of the formation and evolution of pediment domes in the area of the Cima volcanic field, Mojave Desert, California. In This extended land: geological journeys in the Southern Basin and Range: field trip guidebook, Geological Society of America, Cordilleran Section Meeting, Las Vegas, Nevada, 1988, p. 214.

Eizenhöfer, P.R., Zhao, G., Zhang, J., Han, Y., Hou, W., Liu, D. and Wang, B., 2015. Geochemical characteristics of the Permian basins and their provenances across the Solonker Suture Zone: assessment of net crustal growth during the closure of the Palaeo-Asian Ocean. Lithos, v. 224, p. 240-255.

Fedo, C.M., Nesbitt, H.W. and Young, G.M., 1995. Unraveling the effects of potassium metasomatism in sedimentary rocks and paleosols, with implications for paleoweathering conditions and provenance. Geology, v. 23, no. 10, p. 921-924.

Fedo, C.M., Eriksson, K.A. and Krogstad, E.J., 1996. Geochemistry of shales from the Archean (~ 3.0 Ga) Buhwa Greenstone Belt, Zimbabwe: implications for provenance and source-area weathering. Geochimica et Cosmochimica Acta, v. 60, no. 10, p. 1751-1763.

Fedo, C.M. and Cooper, J.D., 2001. Sedimentology and sequence stratigraphy of Neoproterozoic and Cambrian units across a craton-margin hinge zone, southeastern California, and implications for the early evolution of the Cordilleran margin. Sedimentary Geology, v. 141, p. 501-522.

Fedo, C.M., McGlynn, I.O. and McSween, H.Y., 2015. Grain size and hydrodynamic sorting controls on the composition of basaltic sediments: Implications for interpreting martian soils. Earth and Planetary Science Letters, v. 423, p. 67-77.

Feng, R. and Kerrich, R., 1990. Geochemistry of fine-grained clastic sediments in the Archean Abitibi greenstone belt, Canada: implications for provenance and tectonic setting. Geochimica et Cosmochimica Acta, v. 54, no. 4, p. 1061-1081.

Floyd, P.A. and Leveridge, B.E., 1987. Tectonic environment of the Devonian Gramscatho basin, south Cornwall: framework mode and geochemical evidence from turbiditic sandstones. Journal of the Geological Society, v. 144, no. 4, p. 531-542.

Folk, R.L., 1955. Student operator error in determination of roundness, sphericity, and grain size. Journal of Sedimentary Research, v. 25, no. 4, p. 297-301.

Folk, R.L., 1974. Petrology of sedimentary rocks. Texas (Hemphill Publishing Co.). 182 p.

Folk, R.L. and Ward, W.C., 1957. Brazos River bar: a study in the significance of grain-size parameters. Journal of Sedimentary Research, v. 27, no. 1, p. 3-32.

Fralick, P. W., and Kronberg, B. I. 1997. Geochemical discrimination of clastic sedimentary rock sources. Sedimentary Geology, v. 113, no. 1, p. 111-124.

Gu, X.X., Liu, J.M., Zheng, M.H., Tang, J.X. and Qi, L., 2002. Provenance and tectonic setting of the Proterozoic turbidites in Hunan, South China: geochemical evidence. Journal of sedimentary Research, v. 72, no. 3, p. 393-407.

Hofmann, A., Bolhar, R., Dirks, P. and Jelsma, H., 2003. The Geochemistry of Archean shales derived from a mafic volcanic sequence, Belingwe greenstone belt, Zimbabwe: Provenance, source area unroofing and submarine versus subaerial weathering. Geochim. Cosmochim. Acta, v. 67, p. 421-440.

Holail, H.M. and Moghazi, A.K.M., 1998. Provenance, tectonic setting and geochemistry of greywackes and siltstones of the Late Precambrian Hammamat Group, Egypt. Sedimentary Geology, v. 116, no. 3, p. 227-250.

Howard, K.A. and John, B.E., 1987. Crustal extension along a rooted system of imbricate low-angle faults: Colorado River extensional corridor, California and Arizona. Geological Society, London, Special Publications, v. 28, no. 1, p. 299-311.

Ingersoll, R. V., Bullard, T. F., Ford, R. L., Grimm, J. P., Pickle, J. D., and Sares, S. W., 1984. The effect of grain size on detrital modes: a test of the Gazzi-Dickinson point-counting method. Journal of Sedimentary Research, v. 54, no. 1, p. 103-116.

Johnsson, M. J., 1993. The system controlling the composition of clastic sediments. Geological Society of America Special Papers, v. 284, p. 1-20.

Lawrence, M.G. and Kamber, B.S., 2006. The behaviour of the rare earth elements during estuarine mixing—revisited. Marine Chemistry, v. 100, no. 1, p. 147-161.

Lee, Y., II., 2002. Provenance derived from the geochemistry of the Palaeozoic-early Mesozoic mudrocks of the Pyeongan Supergroup, Korea. Sedimentary Geol., v. 149, p. 219- 235

Mahjoor, A.S., Karimi, M. and Rastegarlari, A., 2009. Mineralogical and geochemical characteristics of clay deposits from South Abarkouh district of clay deposit (Central Iran) and their applications. Journal of Applied Sciences, v. 9, no. 4, p. 601-614.

McDonald, E. V., McFadden, L. D., and Wells, S. G., 2003. Regional response of alluvial fans to the Pleistocene-Holocene climatic transition, Mojave Desert, California. Special papers – Geological Society of America, v. 368, p. 189-206.

McDonough, W.F. and Sun, S.S., 1995. The composition of the Earth. Chemical geology, v. 120, no. 3, p. 223-253.

McLennan, S. M., 1989. Rare earth elements in sedimentary rocks; influence of provenance and sedimentary processes. Reviews in Mineralogy and Geochemistry, v. 21, no. 1, p. 169-200.

McLennan, S.M., 2001. Relationships between the trace element composition of sedimentary rocks and upper continental crust. Geochemistry, Geophysics, Geosystems, v. 2, doi:10.1029/2000GC000109.

McLennan, S. M. and Taylor, S. R., 1991. Sedimentary rocks and crustal evolution: tectonic setting and secular trends. The Journal of Geology, v. 99, p. 1-21.

McLennan, S. M., Hemming, S., McDaniel, D. K., and Hanson, G. N., 1993. Geochemical approaches to sedimentation, provenance, and tectonics. Geological Society of America Special Papers, v. 284, p. 21-40.

Miller, C.F. and Wooden, J.L., 1994. Anatexis, hybridization and the modification of ancient crust: Mesozoic plutonism in the Old Woman Mountains area, California. Lithos, v. 32, no. 1, p. 111-133.

Miyashiro, A., 1974. Volcanic rock series in island arcs and active continental margins. American Journal of Science, v. 274, no. 4, p. 321-355.

Modi, A. L., 2011. Processes controlling the composition of first-cycle sediments deposited in an arid-climate, with implications for provenance reconstruction studies.

Moradi, A.V., Sarı, A. and Akkaya, P., 2016. Geochemistry of the Miocene oil shale (Hançili Formation) in the Çankırı-Çorum Basin, Central Turkey: Implications for Paleoclimate conditions, source–area weathering, provenance and tectonic setting. Sedimentary Geology. v. 341, p. 289-303.

Nesbitt, H. W., and Markovics, G., 1980. Chemical processes affecting alkalis and alkaline earths during continental weathering. Geochimica et Cosmochimica Acta, v. 44, no. 11, p. 1659-1666.

Nesbitt, H.W. and Markovics, G., 1997. Weathering of granodioritic crust, long-term storage of elements in weathering profiles, and petrogenesis of siliciclastic sediments. Geochimica et Cosmochimica Acta, v. 61, no. 8, p. 1653-1670.

Nesbitt, H.W. and Young, G.M., 1982. Early Proterozoic climates and plate motions inferred from major element chemistry of lutites. Nature, v. 299, no. 5885, p. 715-717.

Nesbitt, H.W. and Young, G.M., 1984. Prediction of some weathering trends of plutonic and volcanic rocks based on thermodynamic and kinetic considerations. Geochimica et Cosmochimica Acta, v. 48, no. 7, p. 1523-1534.

Nesbitt, H.W. and Young, G.M., 1989. Formation and diagenesis of weathering profiles. The Journal of Geology, v. 97, p. 129-147.

Nesbitt, H.W. and Young, G.M., 1996. Petrogenesis of sediments in the absence of chemical weathering: effects of abrasion and sorting on bulk composition and mineralogy. Sedimentology, v. 43, no. 2, p. 341-358.

Nichols, K.K., Bierman, P.R., Hooke, R.L., Clapp, E.M. and Caffee, M., 2002. Quantifying sediment transport on desert piedmonts using ^{10}Be and ^{26}Al. Geomorphology, v. 45, no. 1, p. 105-125.

Nichols, K.K., Bierman, P.R., Caffee, M., Finkel, R. and Larsen, J., 2005. Cosmogenically enabled sediment budgeting. Geology, v. 33, no. 2, p. 133-136.

Oni, S.O., Olatunji, A.S. and Ehinola, O.A., 2014. Determination of Provenance and Tectonic Settings of Niger Delta Clastic Facies Using Well-Y, Onshore Delta State, Nigeria. Journal of Geochemistry, v. 2014, Article ID 960139.

Peacock, M.A., 1931. Classification of igneous rock series. The Journal of Geology. v. 39, p. 54-67

Powers, M.C., 1953. A new roundness scale for sedimentary particles. Journal of Sedimentary Petrology, v. 23, p. 117-119.

Roser, B.P. and Korsch, R.J., 1988. Provenance signatures of sandstone-mudstone suites determined using discriminant function analysis of major-element data. Chemical geology, v. 67, no. 1, p. 119-139.

Roser, B.P. and Korsch, R.J., 1999. Geochemical characterization, evolution and source of a Mesozoic accretionary wedge: the Torlesse terrane, New Zealand. Geological Magazine, v. 136, no. 5, p. 493-512.

Roser, B.P., Cooper, R.A., Nathan, S. and Tulloch, A.J., 1996. Reconnaissance sandstone geochemistry, provenance, and tectonic setting of the lower Paleozoic terranes of the West Coast and Nelson, New Zealand.New Zealand Journal of Geology and Geophysics, v. 39, no. 1, p. 1-16.

Schoenborn, W.A., Fedo, C.M. and Farmer, G.L., 2012. Provenance of the Neoproterozoic Johnnie Formation and Stirling Quartzite, southeastern California, determined by detrital zircon geochronology and Nd isotope geochemistry. Precambrian Research, v. 206, p. 182-199.

Shand, S.J., 1943. Eruptive rocks: Their genesis, composition, and classification, with a chapter on meteorites. J. Wiley and sons, Incorporated.

Singh, P., 2009. Major, trace and REE geochemistry of the Ganga River sediments: influence of provenance and sedimentary processes. Chemical Geology, v. 266, no. 3, p. 242-255.

Slack, J.F. and Stevens, B.P., 1994. Clastic metasediments of the early Proterozoic Broken Hill Group, New South Wales, Australia: geochemistry, provenance, and metallogenic significance. Geochimica et Cosmochimica Acta, v. 58, no. 17, p. 3633-3652.

Stoffer, P.W., 2004. Desert landforms and surface processes in the Mojave National Preserve and Vicinity, no. 2004-1007.

Streckeisen, A., 1976. To each plutonic rock its proper name. Earth-science reviews, v. 12, no. 1, p. 1-33.

Suttner, L. J., Basu, A., and Mack, G. H., 1981. Climate and the origin of quartz arenites. Journal of Sedimentary Research, v. 51, no. 4, p. 1235-1246.

Tang, Y., Sang, L., Yuan, Y., Zhang, Y. and Yang, Y., 2012. Geochemistry of Late Triassic pelitic rocks in the NE part of Songpan-Ganzi Basin, western China: Implications for source weathering, provenance and tectonic setting. Geoscience Frontiers, v. 3, no. 5, p. 647-660.

Taylor, S. R., and McLennan, S. M., 1985. The continental crust: its composition and evolution. Blackwell, Oxford, p. 312.

Thomas, W.M., Clark, H.S., Young, E.D., Orrell, S.E. and Anderson, J.L., 1988. Proterozoic high-grade metamorphism in the Colorado River region, Nevada, Arizona, and California. Metamorphism and crustal evolution of the western United States, Rubey, v. 7, p. 526-537.

Trail, D., Watson, E.B. and Tailby, N.D., 2012. Ce and Eu anomalies in zircon as proxies for the oxidation state of magmas. Geochimica et Cosmochimica Acta, v. 97, p.70-87.

Wendt, C.J., and Thomas, S.W., 1990. Placer sampling and reserve estimation, in Kennedy, B.A., ed., Surface mining (2d ed.): Littleton, Colo., Society for Mining, Metallurgy, and Exploration, Inc., p. 1194.

Wentworth, C.K., 1922. A scale of grade and class terms for clastic sediments. The Journal of Geology, v. 30, no. 5, p.377-392.

Wooden, J.L. and Miller, D.M., 1990. Chronologic and isotopic framework for Early Proterozoic crustal evolution in the eastern Mojave Desert region, SE California. Journal of Geophysical Research: Solid Earth, v. 95, no. B12, p. 20133-20146.

Wronkiewicz, D.J. and Condie, K.C., 1987. Geochemistry of Archean shales from the Witwatersrand Supergroup, South Africa: source-area weathering and provenance. Geochimica et Cosmochimica Acta, v. 51, no. 9, p. 2401-2416.

Xiang, Z., Yan, Q., White, J.D., Song, B. and Wang, Z., 2015. Geochemical constraints on the provenance and depositional setting of Neoproterozoic volcaniclastic rocks on the northern margin of the Yangtze Block, China: implications for the tectonic evolution of the northern margin of the Yangtze Block. Precambrian Research, v. 264, p. 140-155.

Young, G. M., and Nesbitt, H. W., 1998. Processes controlling the distribution of Ti and Al in weathering profiles, siliciclastic sediments and sedimentary rocks. Journal of Sedimentary Research, v. 68, no. 3, p. 448-455.

Zimmermann, U. and Bahlburg, H., 2003. Provenance analysis and tectonic setting of the Ordovician clastic deposits in the southern Puna Basin, NW Argentina. Sedimentology, v. 50, no. 6, p. 1079-1104.

APPENDICES

Appendix A

Sample Images

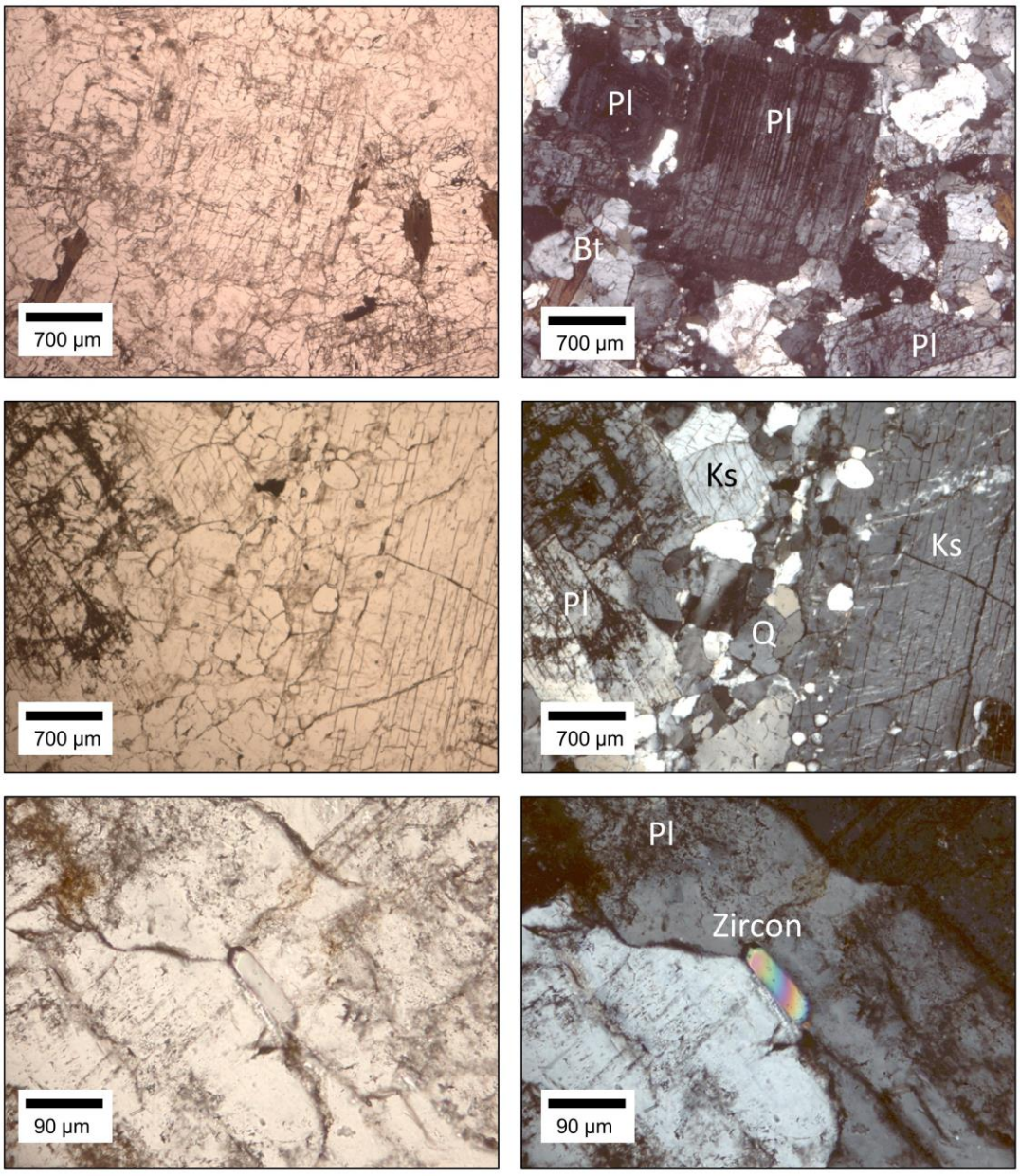

Figure A 1. Photomicrographs of Stepladder bedrock.

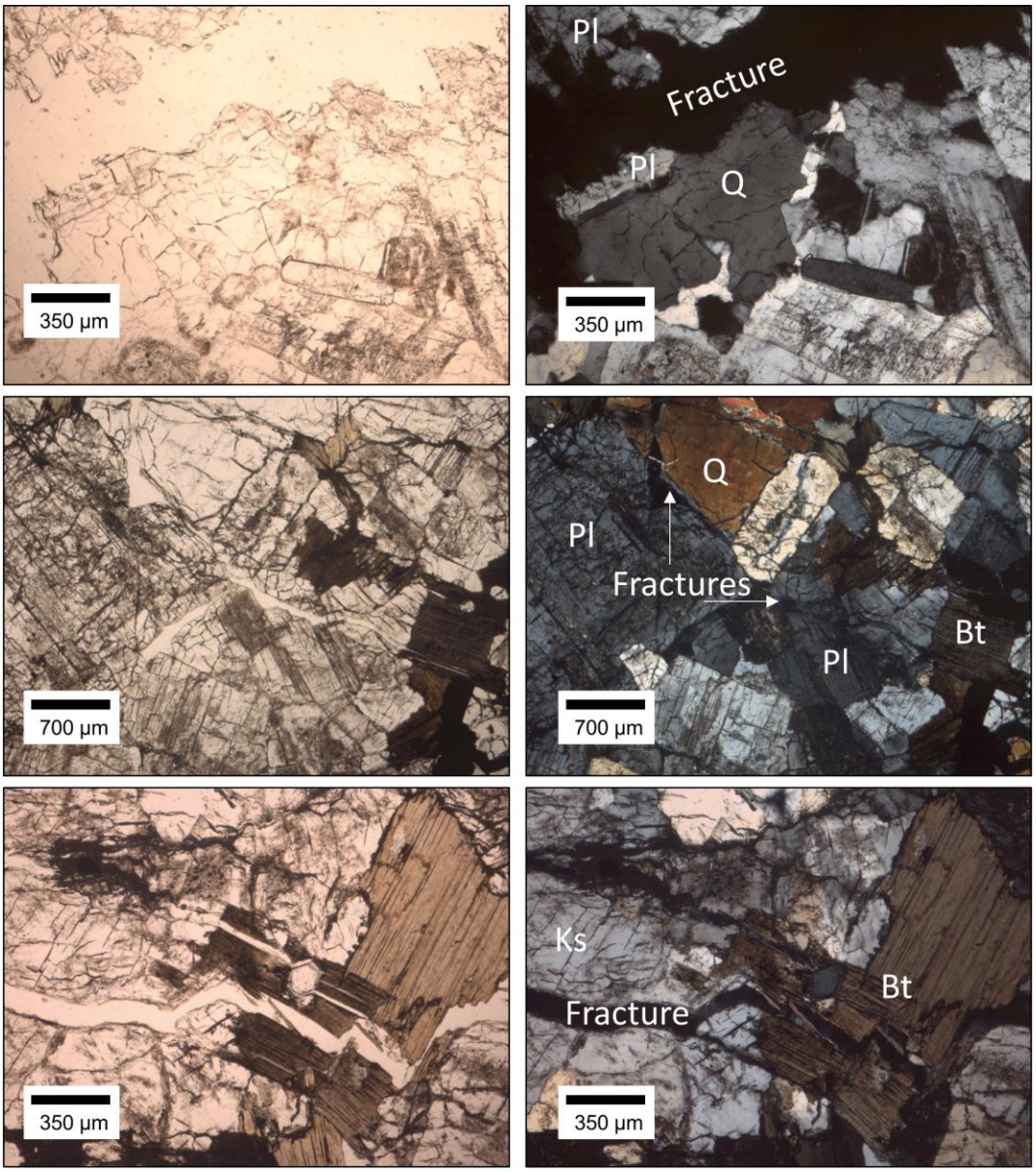

Figure A 2. Photomicrographs of Stepladder saprolite.

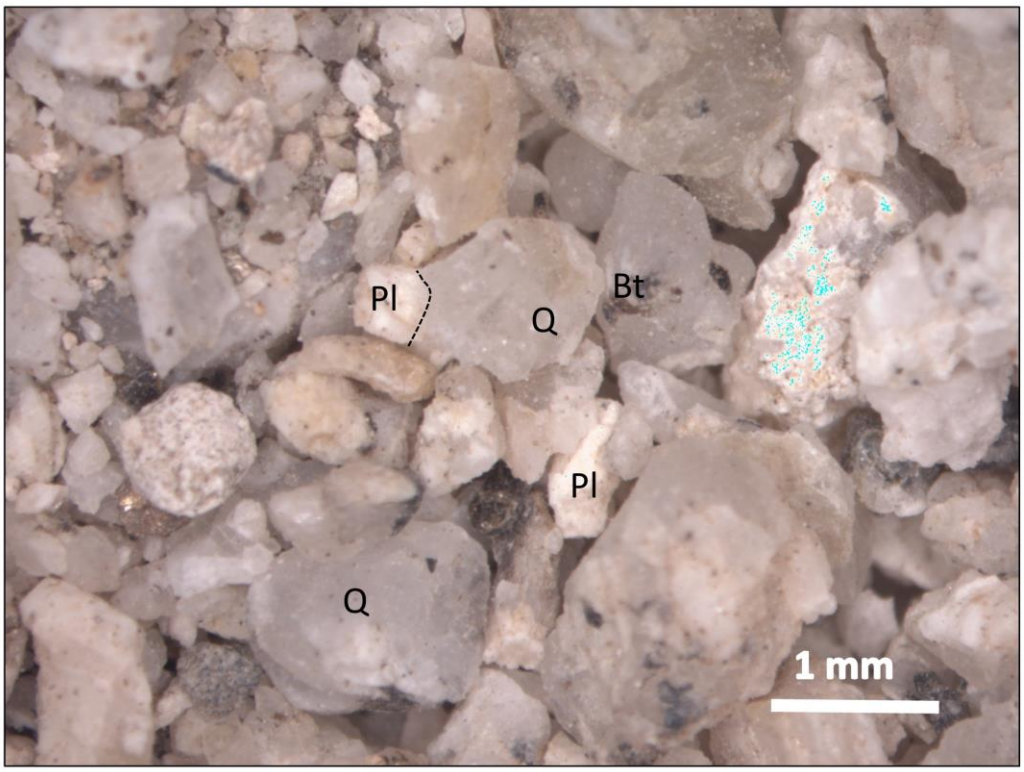

Figure A 3. Loose sediment from sample CD-1.

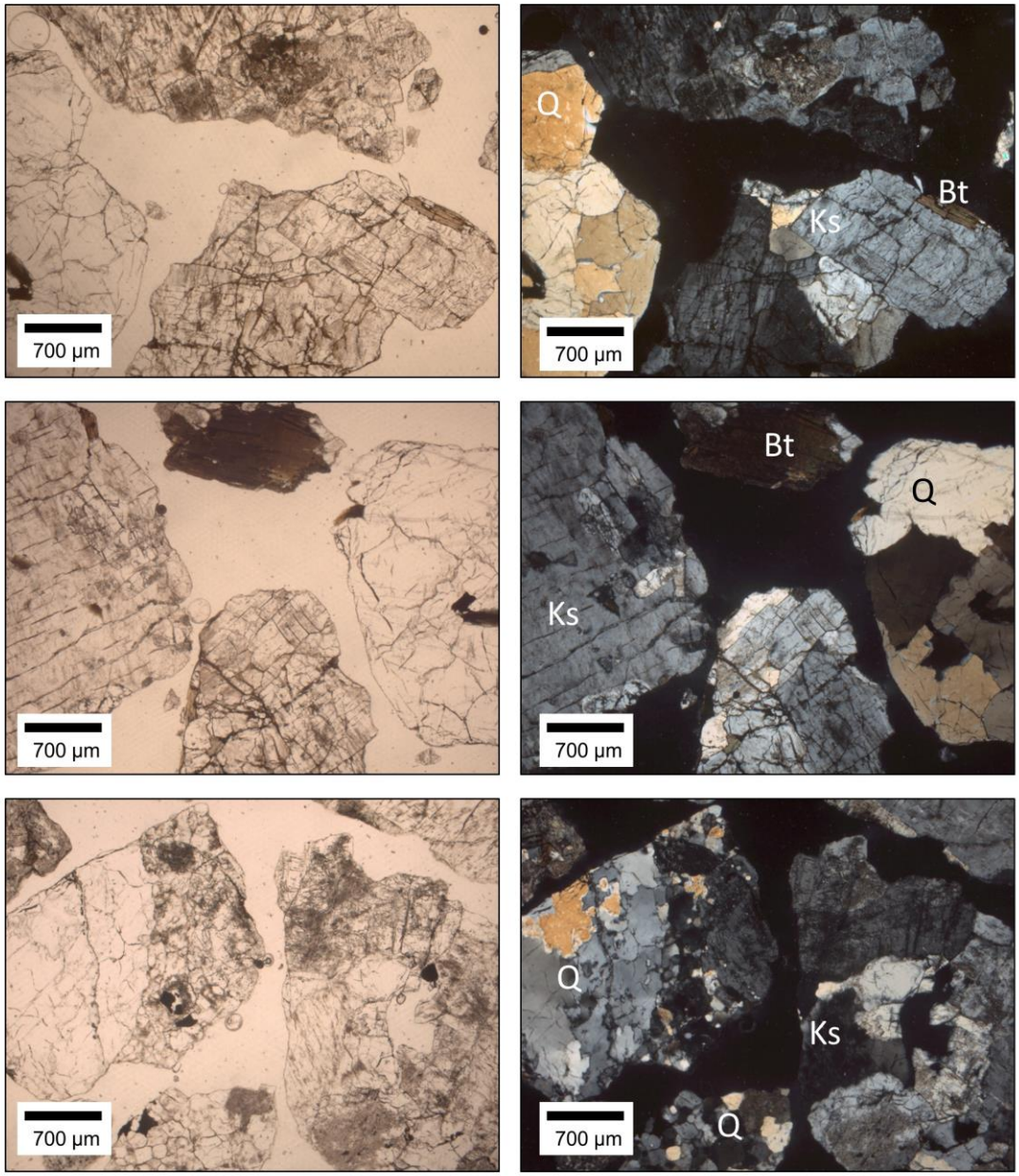

Figure A 4. Photomicrographs of sample CD-1.

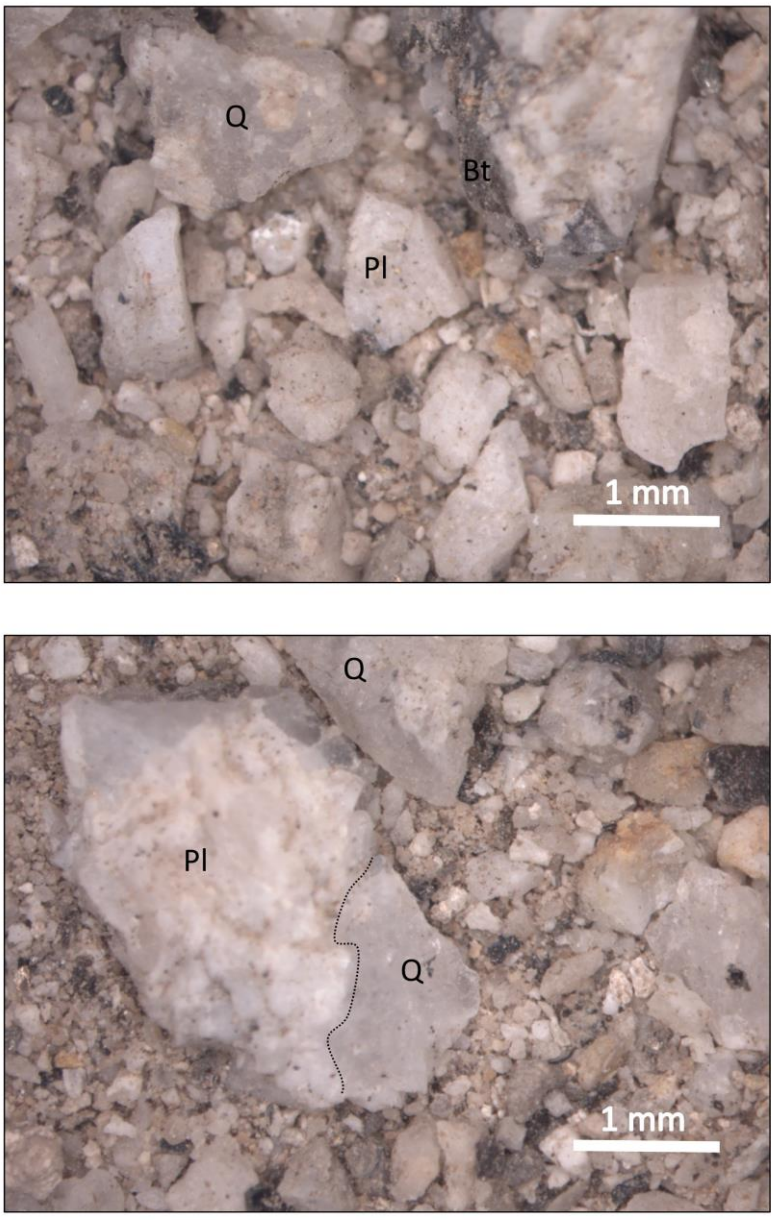

Figure A 5. Loose sediment from sample CD-2.

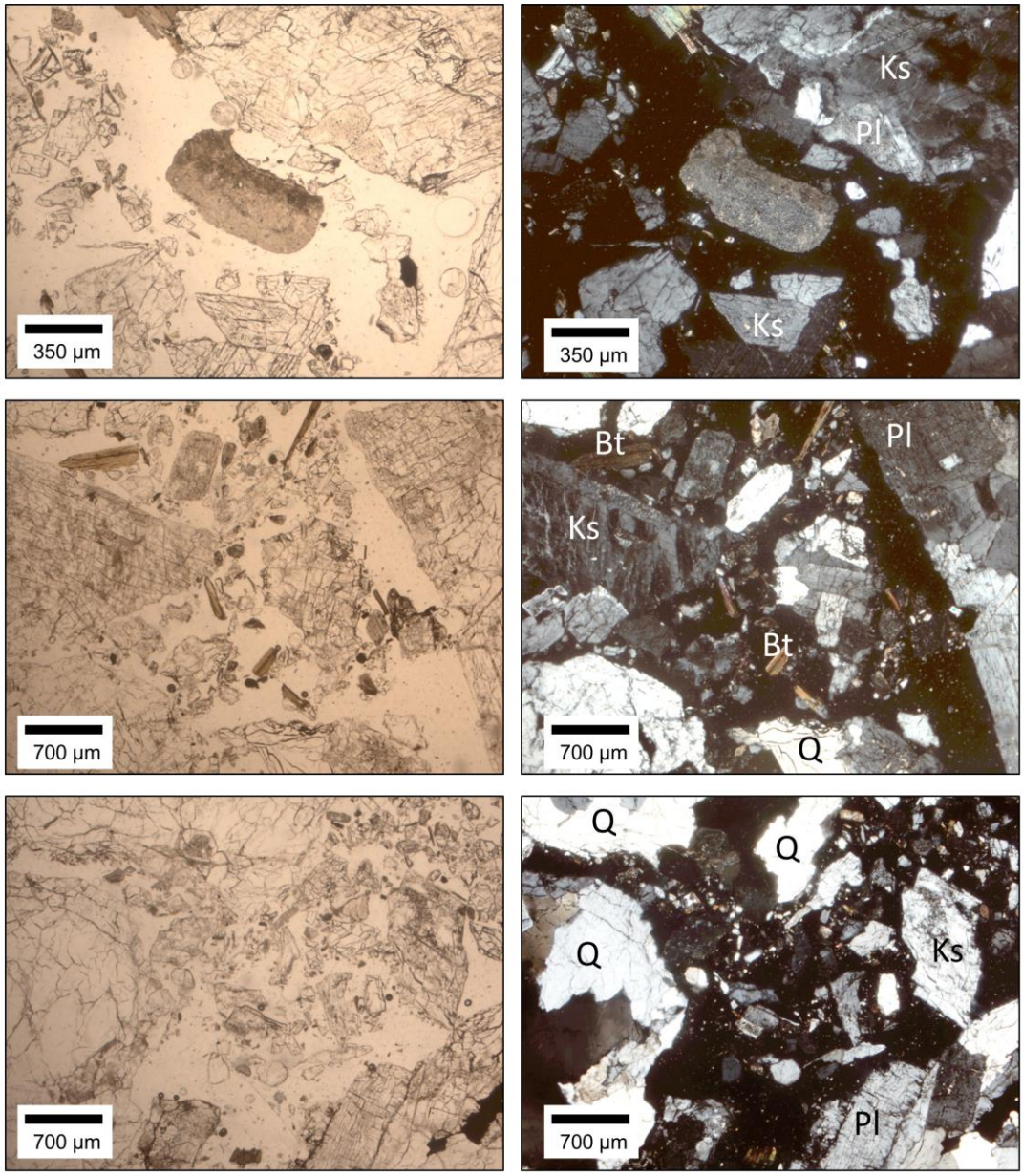

Figure A 6. Photomicrographs of sample CD-2.

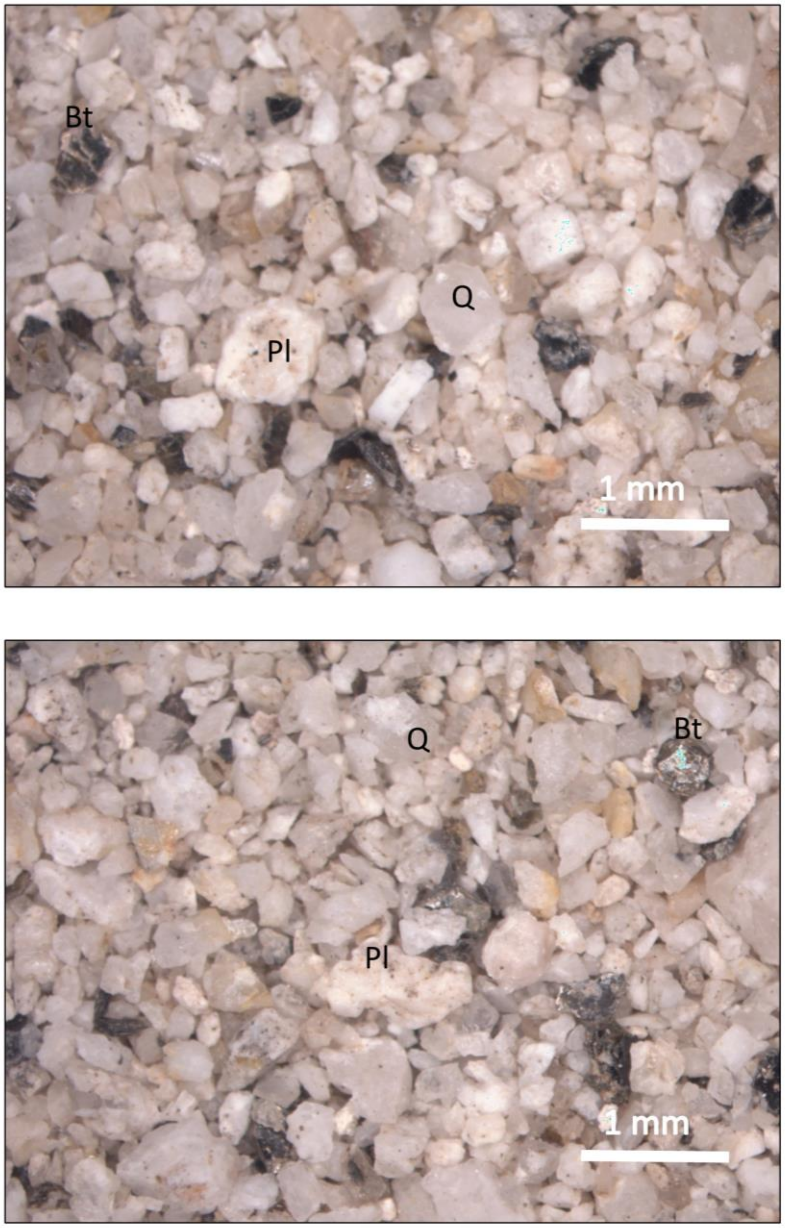

Figure A 7. Loose sediment from sample CD-3.

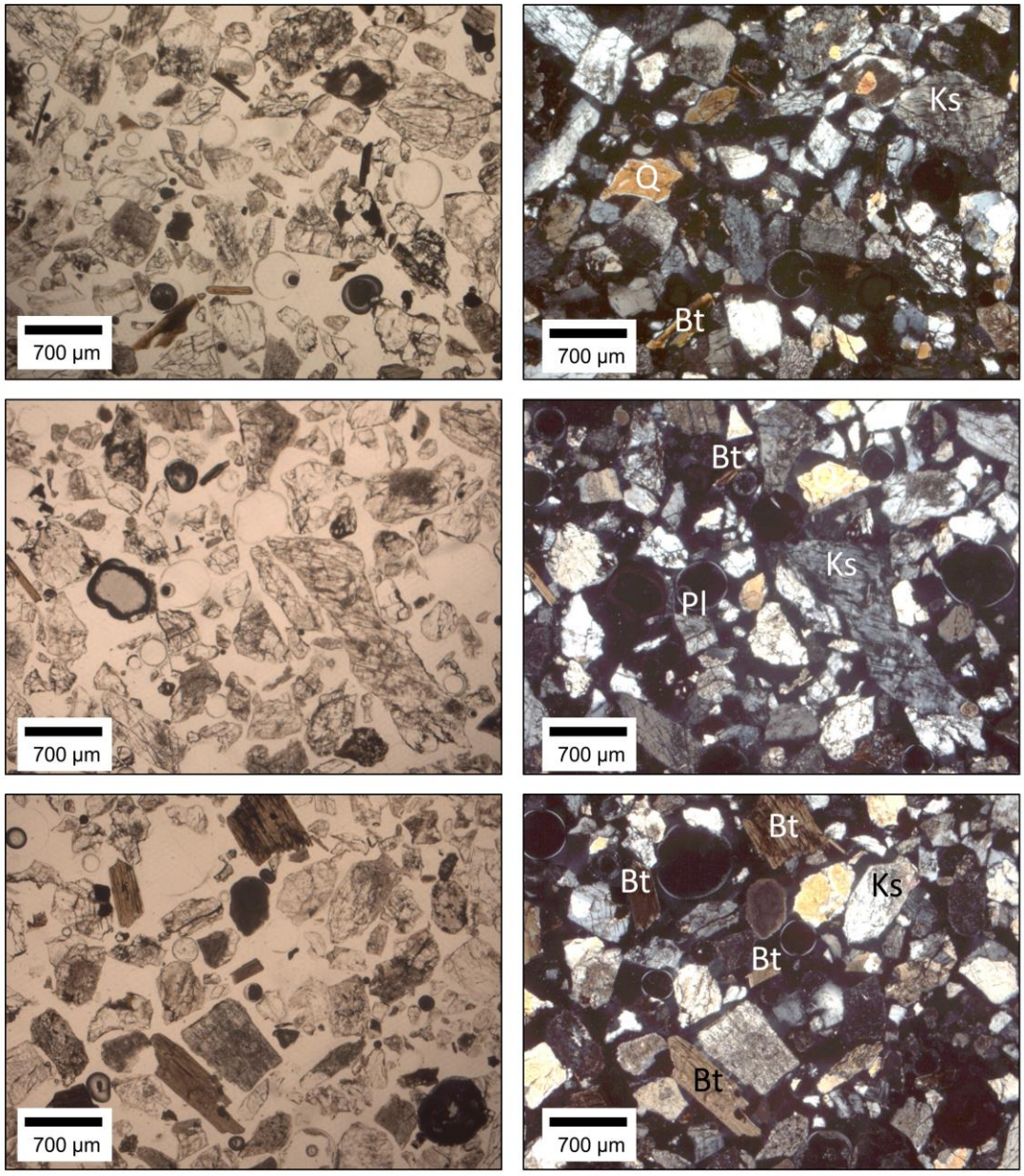

Figure A 8. Photomicrographs of sample CD-3.

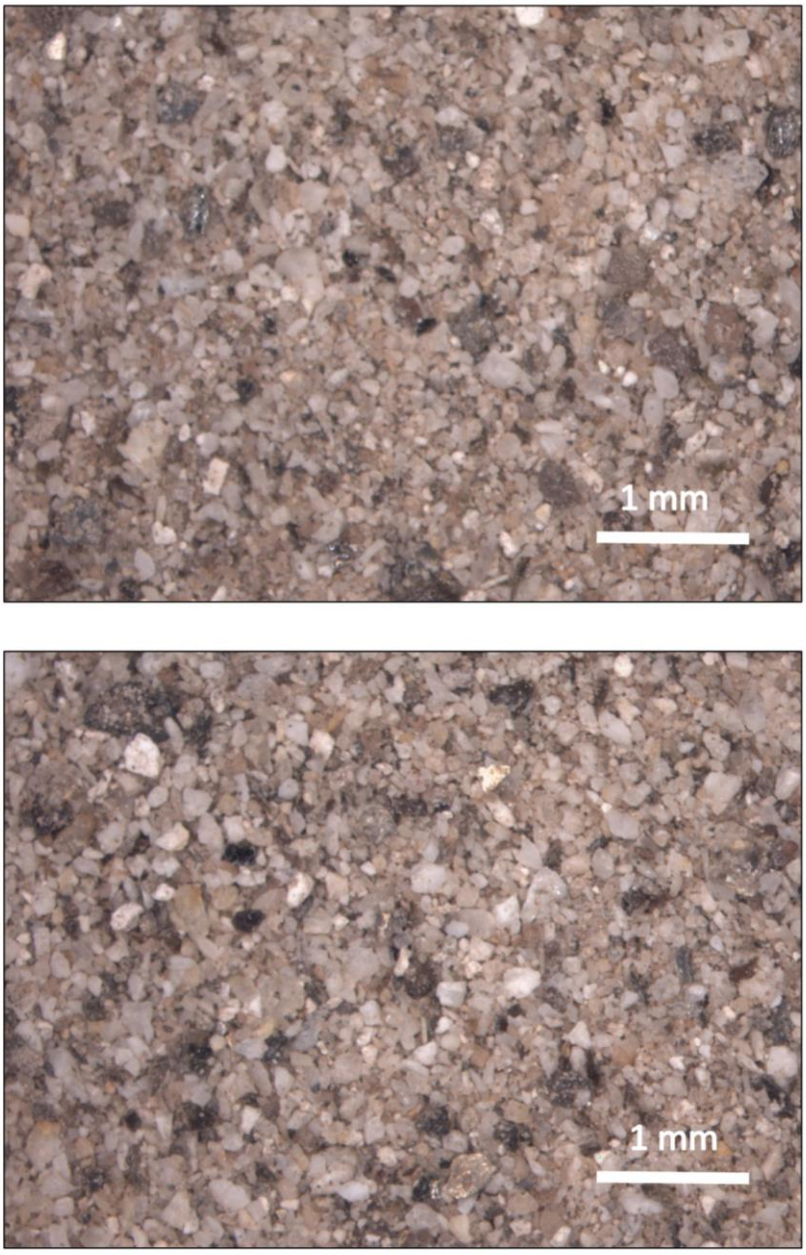

Figure A 9. Loose sediment from sample CD-4.

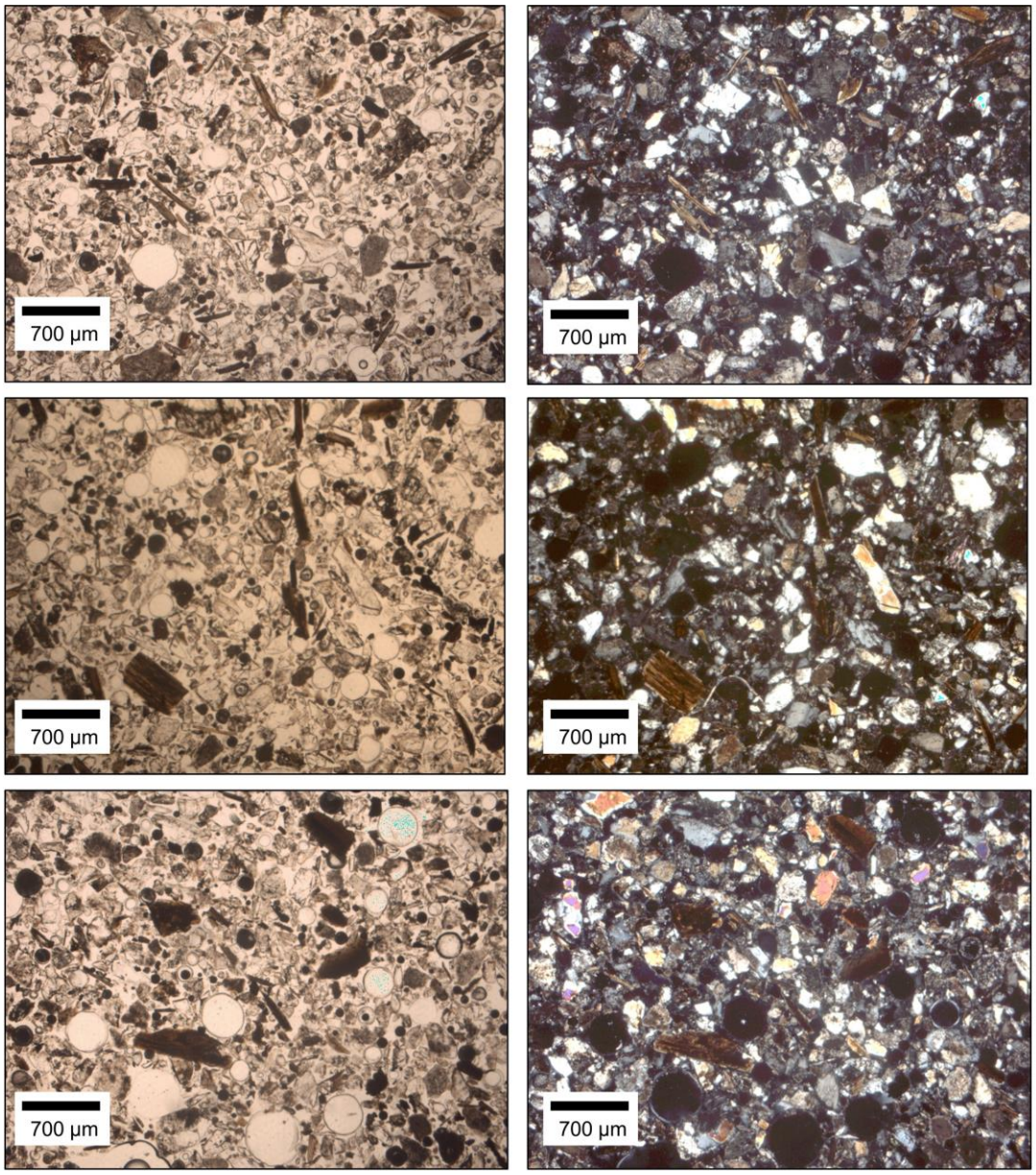

Figure A 10. Photomicrographs of sample CD-4.

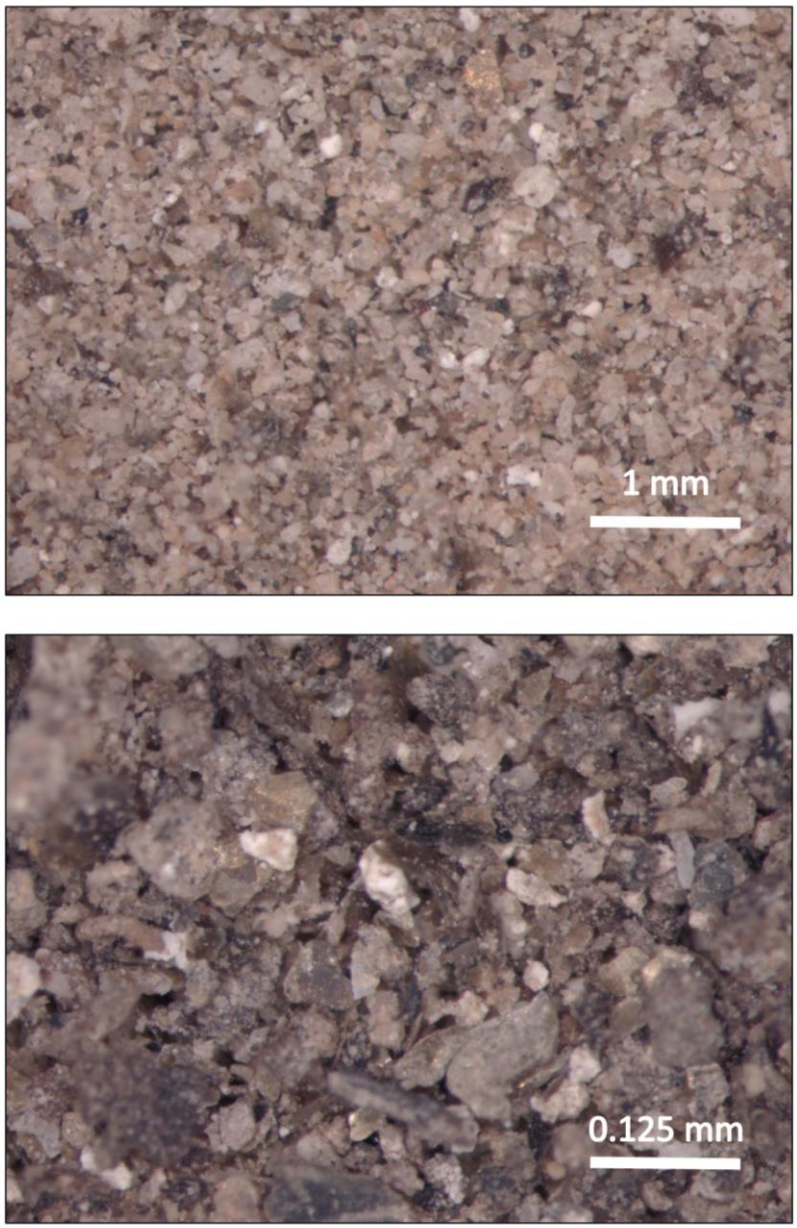

Figure A 11. Loose sediment from sample CD-5.

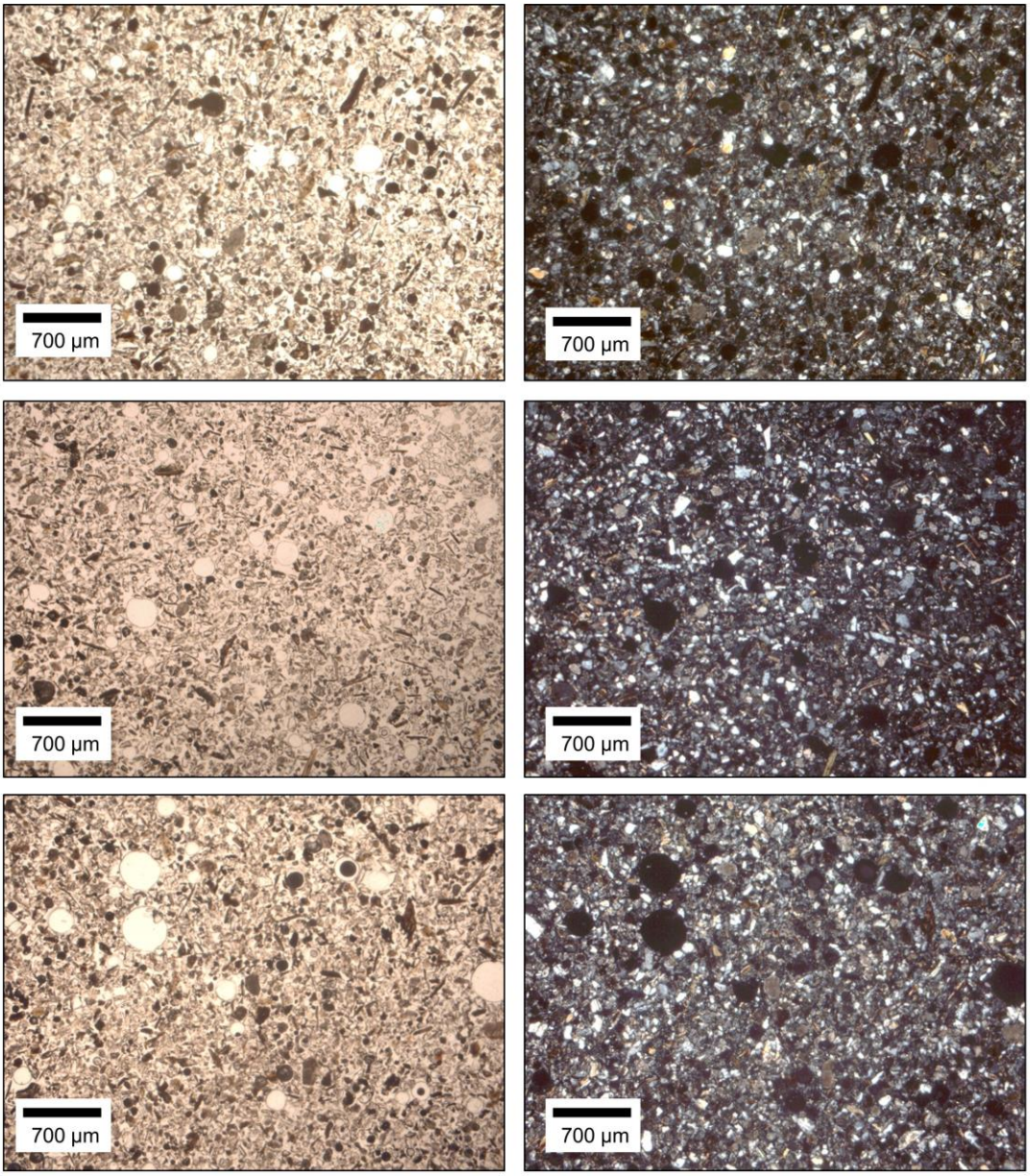

Figure A 12. Photomicrographs of sample CD-5.

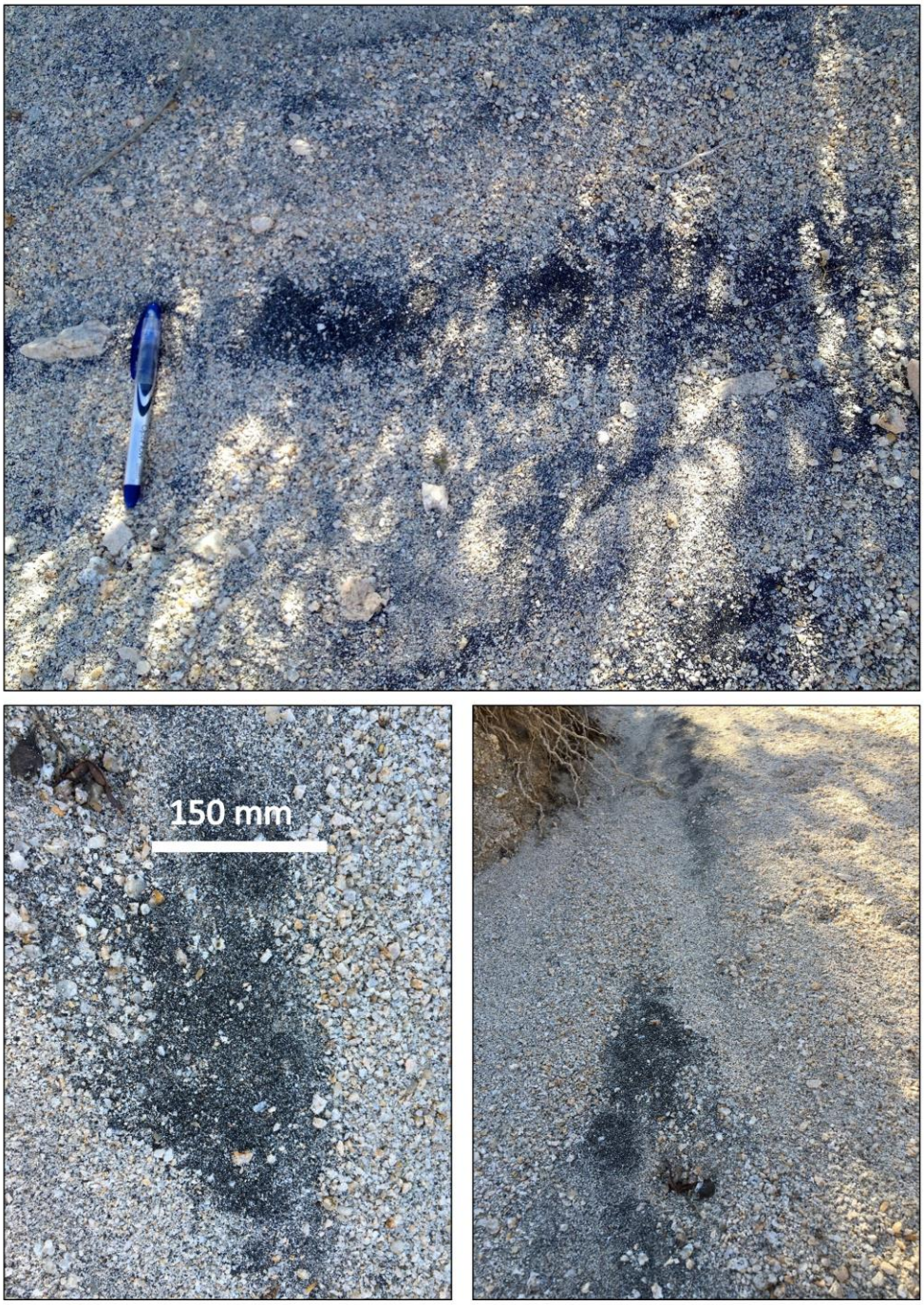

Figure A 13. Field photographs of magnetite concentrate sample CD-M in channel.

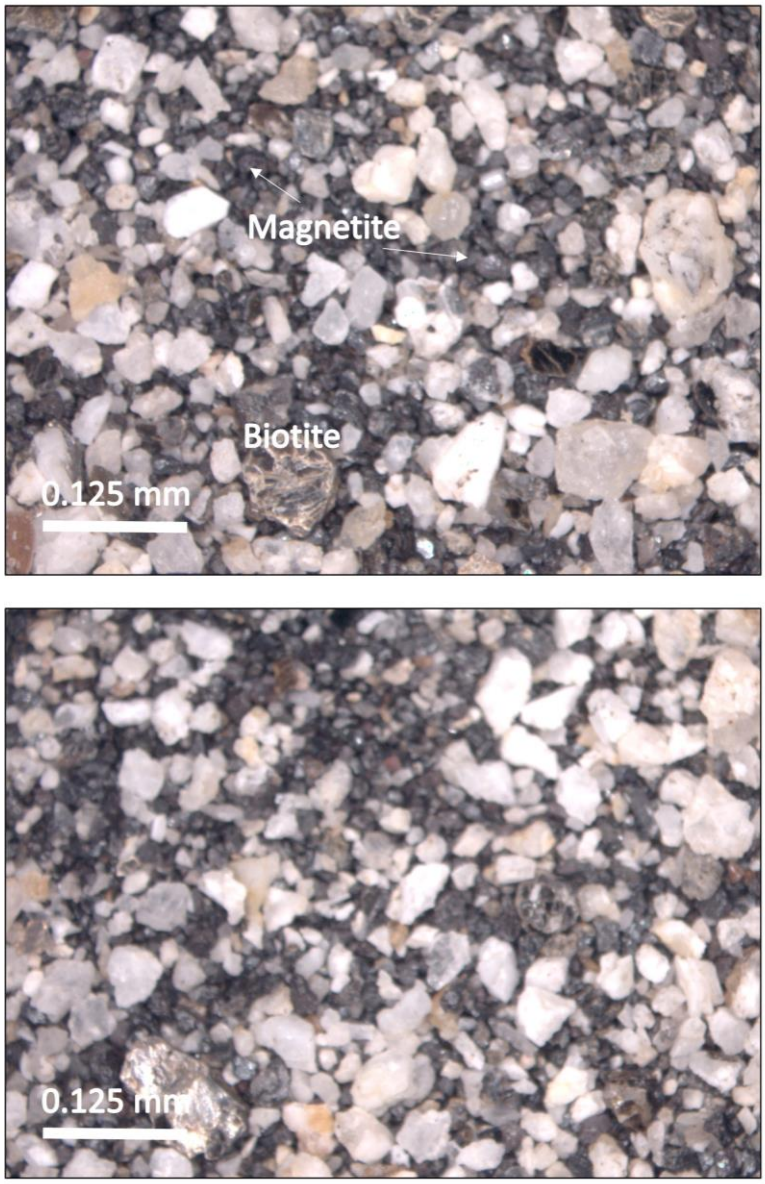

Figure A 14. Loose sediment from sample CD-M.

Appendix B

Joint Measurements

Table B 1. Measurements of joint set orientations taken across watershed.

NE Strike/Steep Dip			NW Strike/Steep Dip			NE Strike/NW Dip		
Strike	Dip	Dip Quad	Strike	Dip	Dip Quad	Strike	Dip	Dip Quad
70	83	S	300	89	N	220	36	W
50	80	S	300	87	N	219	33	W
70	70	S	320	64	E	230	40	N
40	89	E	330	79	E			
33	90	E	310	69	N			
30	72	E	340	80	E			
27	72	E	300	76	N			
61	90	S	280	85	N			
50	70	S	297	90	N			
50	82	S	285	90	N			
45	89	E	290	74	N			
30	70	E	295	46	N			
76	75	S	345	70	E			
30	88	E	335	87	E			
30	90	E	295	90	N			
65	85	S	335	70	E			
77	80	S	310	56	N			
20	56	E	290	72	N			
75	77	S	280	85	N			
75	67	S						
83	90	S						
85	87	S						
75	87	S						
25	77	E						
30	72	E						
40	82	E						
72	77	S						
88	90	S						
72	90	S						
25	75	E						
50	90	S						
60	90	S						
45	82	E						
70	83	S						
60	74	S						

Appendix C

Sieving Data

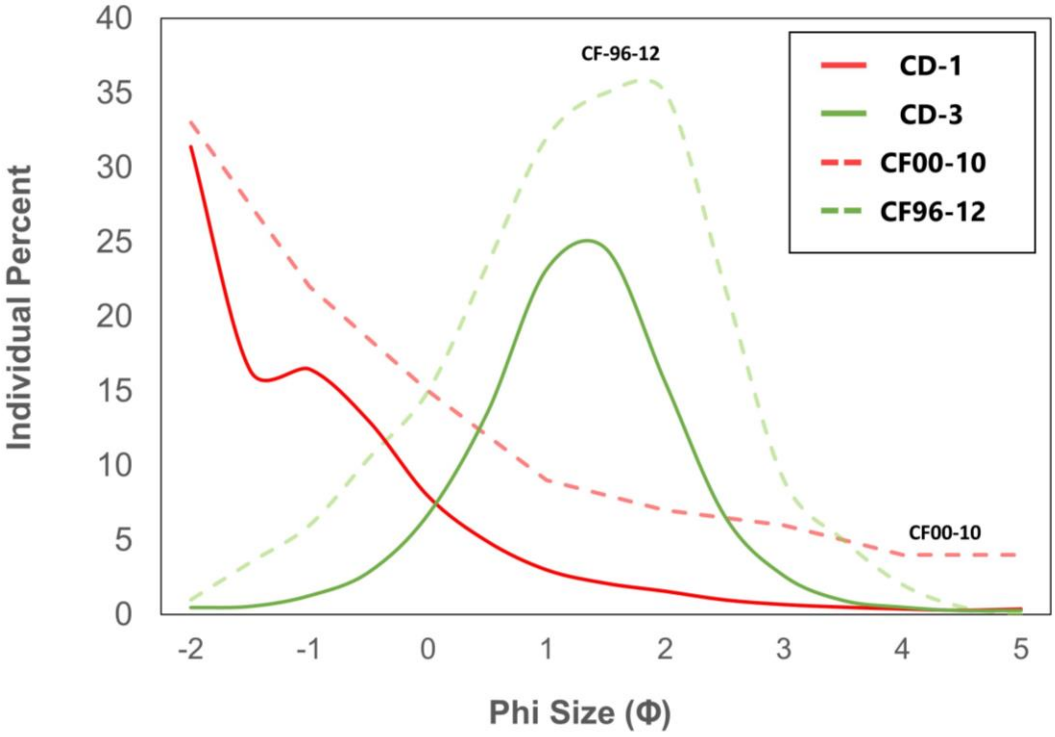

Figure C 1. Grain-size overlays of samples CD-1 and CD-3 with samples from Modi (2011) with similar grain-size distributions.

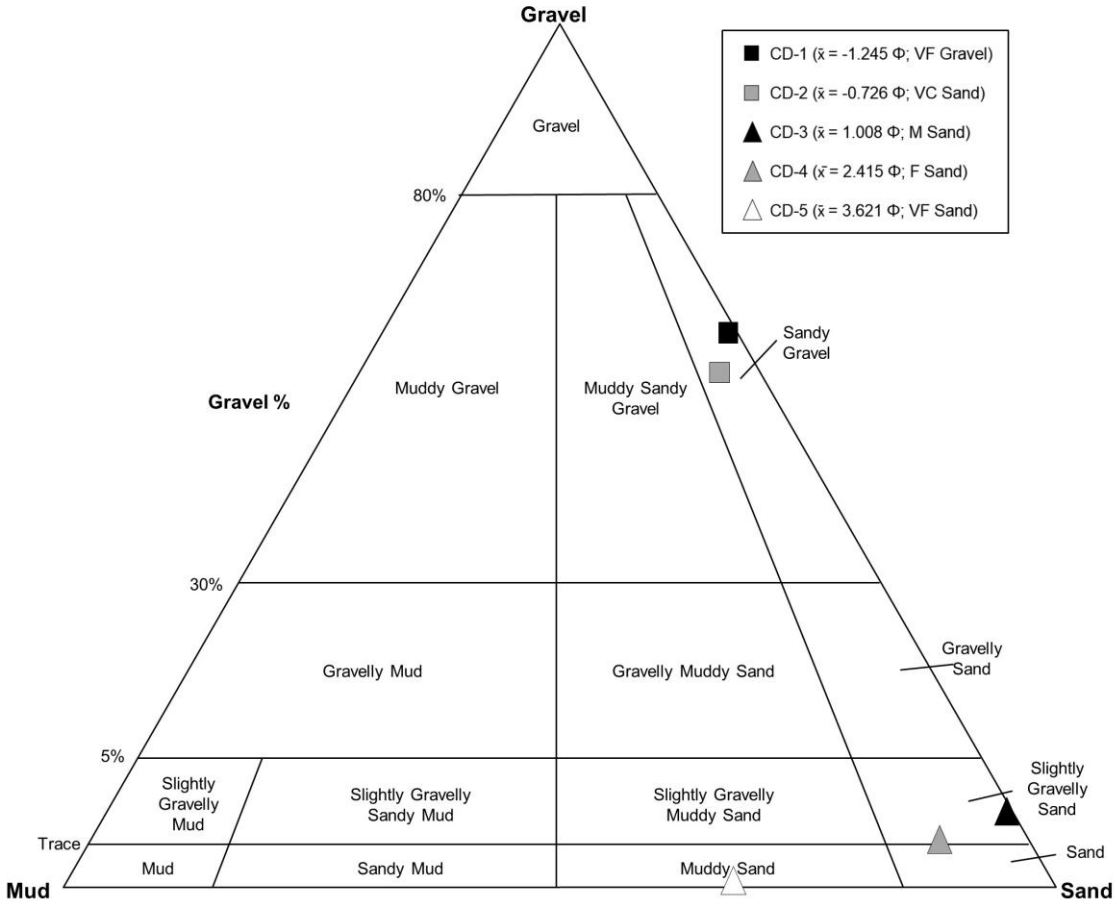

Figure C 2. Gravel-Mud-Sand textural classification diagram plotting channel sediments.

Table C 1. Sieve data for each sediment sample CD-1 through CD-5, and CD-M.

CD-1				CD-2				CD-3			
Phi	**Indiv. %**	**Cumu. %**	**Wt (g)**	**Phi**	**Indiv. %**	**Cumu. %**	**Wt (g)**	**Phi**	**Indiv. %**	**Cumu. %**	**Wt (g)**
-2	31.40	31.40	245.14	-2	38.07	38.07	289.89	-2	0.47	0.47	2.61
	16.39	47.79	127.98		11.93	50.01	90.88		0.55	1.03	3.02
-1	16.47	64.27	128.63	-1	8.93	58.95	68.01	-1	1.27	2.30	6.94
	13.00	77.27	101.5		6.84	65.79	52.1		2.85	5.15	15.53
0	7.95	85.22	62.08	0	4.76	70.55	36.26	0	6.72	11.87	36.62
	4.91	90.14	38.35		4.03	74.59	30.7		13.54	25.42	73.79
1	3.00	93.14	23.42	1	4.16	78.75	31.7	1	23.17	48.59	126.24
	2.09	95.23	16.38		4.41	83.16	33.6		24.55	73.14	133.76
2	1.56	96.80	12.23	2	4.37	87.54	33.29	2	15.58	88.73	84.93
	0.98	97.79	7.69		3.41	90.95	26.02		6.64	95.37	36.18
3	0.67	98.46	5.26	3	2.65	93.61	20.19	3	2.61	97.99	14.24
	0.49	98.96	3.88		1.92	95.53	14.67		0.95	98.94	5.21
4	0.38	99.34	2.98	4	1.58	97.12	12.05	4	0.50	99.44	2.73
	0.28	99.62	2.23		1.08	98.20	8.26		0.26	99.71	1.46
5	0.37	100	2.89	5	1.79	100	13.65	5	0.28	100	1.55
Total			780.64	Total			761.27	Total			544.81

CD-4				CD-5				CD-M			
Phi	**Indiv. %**	**Cumu. %**	**Wt (g)**	**Phi**	**Indiv. %**	**Cumu. %**	**Wt (g)**	**Phi**	**Indiv. %**	**Cumu. %**	**Wt (g)**
-2	0.30	0.30	0.99	-2	0	0	0	-2	0.31	0.31	0.63
	0.18	0.48	0.61		0	0	0		0.64	0.95	1.28
-1	0.34	0.83	1.15	-1	0	0	0	-1	1.22	2.18	2.43
	0.38	1.22	1.27		0.01	0.01	0.03		2.01	4.19	4.01
0	0.66	1.88	2.18	0	0.01	0.02	0.06	0	2.91	7.10	5.8
	1.20	3.08	3.95		0.03	0.06	0.12		4.38	11.49	8.73
1	3.25	6.34	10.71	1	0.12	0.19	0.43	1	6.90	18.39	13.74
	8.61	14.96	28.34		0.48	0.67	1.62		10.80	29.20	21.51
2	18.52	33.48	60.9	2	1.67	2.35	5.6	2	25.21	54.42	50.20
	22.63	56.11	74.42		4.85	7.20	16.19		31.06	85.48	61.83
3	18.77	74.88	61.72	3	13.64	20.84	45.54	3	12.59	98.08	25.08
	11.47	86.36	37.73		23.01	43.85	76.81		1.52	99.60	3.03
4	7.067	93.43	23.24	4	24.76	68.61	82.66	4	0.24	99.84	0.48
	3.59	97.02	11.81		16.25	84.87	54.25		0.07	99.92	0.15
5	2.97	100	9.79	5	15.12	100	50.5	5	0.075	100	0.15
Total			328.81	Total			333.81	Total			199.05

Table C 2. Textural data output from GRADISTAT program by Blott and Pye, 2001.

		CD-1	CD-2	CD-3	CD-4	CD-5	CD-M
	SIEVING ERROR (%):	0.1	0.2	0.0	0.2	0.1	0.2
	SAMPLE TYPE:	Bimodal, Poorly Sorted	Unimodal, Poorly Sorted	Unimodal, Moderately Sorted	Unimodal, Moderately Sorted	Unimodal, Moderately Sorted	Unimodal, Moderately Sorted
	TEXTURAL GROUP:	Sandy Gravel	Sandy Gravel	Slightly Gravelly Sand	Slightly Gravelly Sand	Muddy Sand	Slightly Gravelly Sand
	SEDIMENT NAME:	Sandy Very Fine Gravel	Sandy Fine Gravel	Slightly Very Fine Gravelly Medium Sand	Slightly Very Fine Gravelly Fine Sand	Very Coarse Silty Very Fine Sand	Slightly Very Fine Gravelly Fine Sand
Folk and Ward Method (Φ)	Mean ($\bar{x}$)	-1.24454	-0.7258	1.008309	2.414867	3.620854	1.728942
	Sorting (σ)	1.123465	1.841119	0.872632	0.980041	0.794267	0.894991
	Skewness (*Sk*)	0.365226	0.632267	-0.0385	0.099876	-0.0101	-0.37022
	Kurtosis (*K*)	1.034581	0.871386	1.128224	1.130148	0.953712	1.304965
Descriptions	Mean ($\bar{x}$)	Very Fine Gravel	Very Coarse Sand	Medium Sand	Fine Sand	Very Fine Sand	Medium Sand
	Sorting (σ)	Poorly Sorted	Poorly Sorted	Moderately Sorted	Moderately Sorted	Moderately Sorted	Moderately Sorted
	Skewness (*Sk*)	Very Fine Skewed	Very Fine Skewed	Symmetrical	Symmetrical	Symmetrical	Very Coarse Skewed
	Kurtosis (*K*)	Mesokurtic	Platykurtic	Leptokurtic	Leptokurtic	Mesokurtic	Leptokurtic
Grain-Size Distribution	% GRAVEL:	64.27419	58.95149	2.307226	0.836349	0	2.180357
	% SAND:	35.07671	38.19612	97.14663	92.67957	69.00474	97.67071
	% MUD:	0.649107	2.85239	0.54614	6.484085	30.99526	0.148931
	% V COARSE GRAVEL:	0	0	0	0	0	0
	% COARSE GRAVEL:	0	0	0	0	0	0
	% MEDIUM GRAVEL:	0	0	0	0	0	0
	% FINE GRAVEL:	31.40244	38.07979	0.479066	0.301086	0	0.316503
	% V FINE GRAVEL:	32.87175	20.8717	1.82816	0.535264	0	1.863853
	% V COARSE SAND:	20.9546	11.60692	9.572144	1.049238	0.026961	4.92841
	% COARSE SAND:	7.912738	8.196829	36.71555	4.458502	0.164764	11.28862
	% MEDIUM SAND:	3.664942	8.786633	40.1406	27.14029	2.162907	36.02612
	% FINE SAND:	1.658895	6.07012	9.254603	41.40385	18.49256	43.6624
	% V FINE SAND:	0.885531	3.535619	1.463735	18.62768	48.15755	1.765161
	% V COARSE SILT:	0.649107	2.85239	0.54614	6.484085	30.99526	0.148931

Appendix D

Petrographic and Geochemical Figures/Tables

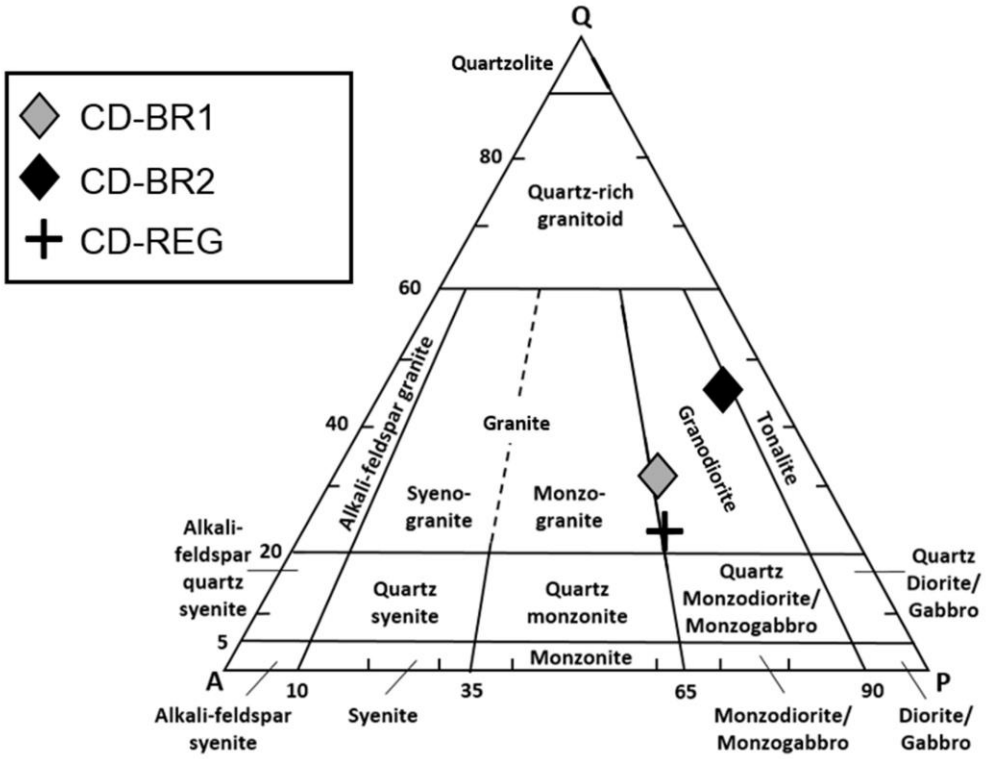

Figure D 1. Quartz-Alkali feldspar-Plagioclase (QAP) plutonic compositional classification diagram plotting bedrock and saprolite samples.

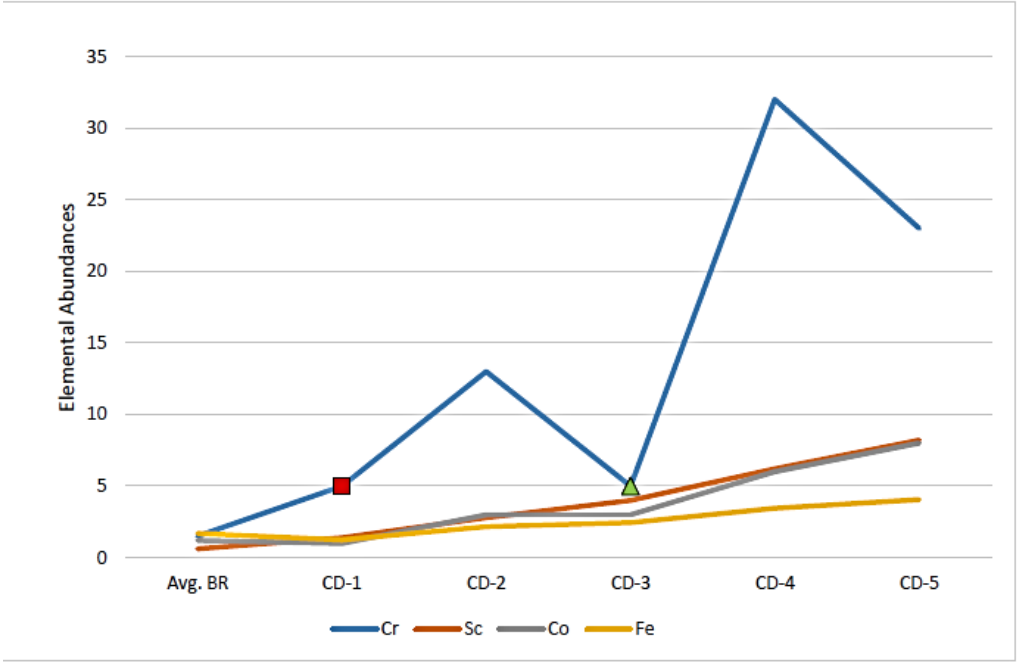

Figure D 2. Elemental abundances of Cr, Sc, Co, and FeO across average bedrock and channel sediments.

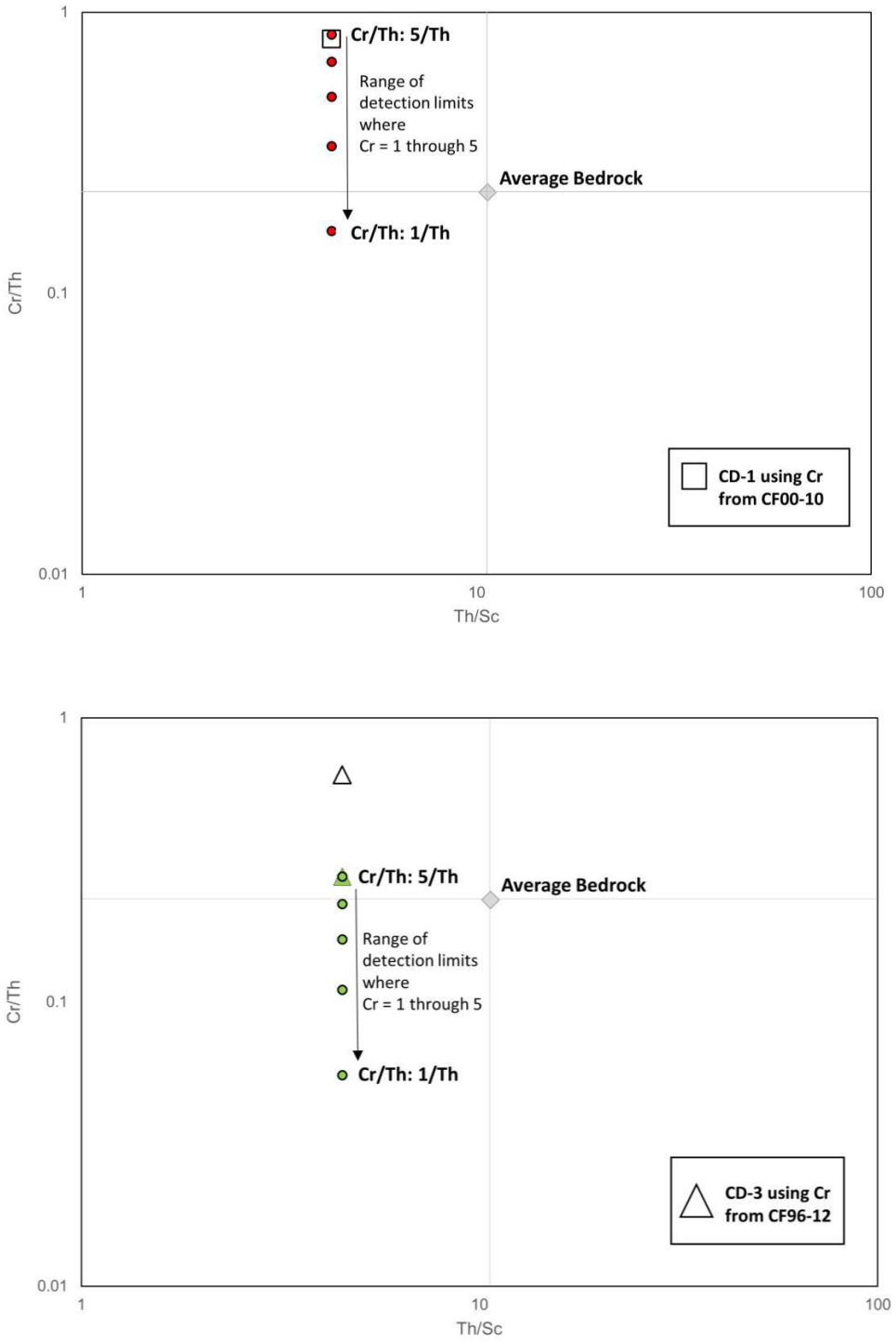

Figure D 3. Cr/Th vs Th/Sc iterative plots of CD-1 (above) and CD-3 (below).

Table D 1. Descriptive compositional parameters and ratios for Stepladder bedrock and saprolite samples.

	A/CNK	A/NK	ASI	Fe*	N+K-Ca
Bedrock					
ST09-02	1.47	1.83	1.49	0.75	6.30
CF00-18	1.45	1.86	1.48	0.71	5.84
CF96-4	1.47	1.82	1.49	0.77	6.42
CF96-8	1.52	1.90	1.54	0.73	5.85
Avg	1.48	1.85	1.50	0.74	6.11
Saprolite					
CF00-04	1.43	1.74	1.44	0.81	6.49
CF00-05	1.45	1.77	1.47	0.78	6.36
Avg	1.43	1.75	1.46	0.80	6.43

Formulas:
A/CNK: $Al_2O_3/CaO+Na_2O+K_2O$
A/NK: Al_2O_3/ Na_2O+K_2O
ASI: Al/Ca – 1.67P + Na + K
Fe*: Fe* FeO_{tot}/ FeO_{tot} + MgO
N+K-Ca: $Na_2O + K_2O – CaO$

Table D 2. Trace element ratios of Stepladder channel sediments, magnetite concentrate, bedrock, and saprolite.

	Sediment Samples					Bedrock*	Saprolite*
	CD-1 *Avg.*	CD-2	CD-3	CD-4	CD-5	*Avg.*	*Avg.*
Th/Sc	4.29	3.86	4.52	2.31	1.36	10.66	9.11
La/Sc	15.68	11.64	7.55	7.67	5.89	35.06	32.36
La/Th	3.65	3.02	1.67	3.33	4.27	3.29	3.55
Zr/Sc	72.86	57.86	44.50	39.03	42.93	274.52	207.54
Th/Co	6.00	3.60	6.03	2.38	1.41	5.46	4.86
Co/Th	0.17	0.28	0.16	0.42	0.71	0.18	0.20
Cr/Th	0.83	1.20	0.28	2.24	2.03	0.23	0.23

*Data from Modi (2011)

Note: Cr values used for samples CD-1 and CD-3 were derived from Modi (2011) from samples with respective grain-size distributions.

VITA

Forrest Christopher Driscoll was born on July 17th, 1992 in Radford, Virginia. During high school, he attended the Southwest Virginia Governor's School for Science, Mathematics, and Technology. In 2010, he enrolled at Virginia Tech to pursue his interest in geology. While at Virginia Tech, he was an active research assistant for other graduate students. In 2014, he graduated from Virginia Tech with a B.S. in geology. Because of his positive experience doing research, he enrolled as a graduate student in the Department Earth and Planetary Sciences at the University of Tennessee, Knoxville to work with advisor Dr. Chris Fedo. He defended his thesis on July 8th, 2016 to receive his M.S. in Geology.